Phase Equilibria of Imidazolium-based Ionic Liquids and Water

By

Alejandra Rocha

Submitted to the graduate degree program in Chemical and Petroleum Engineering Department and the Graduate Faculty of the University of Kansas in partial fulfillment of the requirements for the degree of Master of Science.

Chair: Mark B. Shiflett

Aaron Scurto

Bala Subramaniam

Date Defended: 10 December 2018

The thesis committee for Alejandra Rocha certifies that this is the approved version of the following thesis:

Phase Equilibria of Imidazolium-based Ionic Liquids and Water

Chair: Mark B. Shiflett

Date Approved: 10 December 2018

Abstract

Ionic liquids (ILs) are widely investigated materials due to their green properties including negligible vapor pressure, chemical tunability, and high temperature stability. The presence of water in ionic liquids has been observed to affect certain IL properties. Due to the ubiquitous nature of water and the fact that all ILs are hygroscopic to an extent, studies on the sorption of water into ILs are necessary. This research describes the application of the gravimetric microbalance technique for water sorption measurements in ILs and presents reproducible and accurate solubility data for water absorption and desorption in five ionic liquids 1-ethyl-3-methylimidazolium tetrafluoroborate [C_2C_1im][BF_4], 1-ethyl-3-methylimidazolium 1,1,2,2-tetrafluoroethane-1-sulfonate [C_2C_1im][TFES], 1-ethyl-3-methylimidazolium acetate [C_2C_1im][OAc], 1-butyl-3-methylimidazolium acetate [C_4C_1im][OAc], and 1-butyl-3-methylimidazolium chloride [C_4C_1im][Cl] at 283 K – 315 K and 0 – 70 % relative humidity (RH). The water solubility in order of highest to lowest at 303.15 K and 25 % RH was: [C_2C_1im][OAc] (78.4 mol%) > [C_4C_1im][OAc] (77.5 mol%) > [C_4C_1im][Cl] (68.6 mol%) > [C_2C_1im][TFES] (26.5 mol%) > [C_2C_1im][BF_4] (19.5 mol%).

The solubility data were well correlated with the Non-Random Two Liquid (NRTL) activity coefficient model and time dependent concentration data were used to determine the binary diffusion coefficients of water in the water-IL systems. The diffusion coefficients in order of increasing relative humidity ranged from: 1.3×10^{-10} to 2.7×10^{-11} m^2/s for [C_2C_1im][BF_4], 4.4×10^{-11} to 1.2×10^{-10} m^2/s for [C_2C_1im][TFES], 4.6×10^{-12} to 2.8×10^{-11} m^2/s for [C_2C_1im][OAc], 8.8×10^{-12} m^2/s to 3.9×10^{-11} m^2/s for [C_4C_1im][OAc], and 4.5×10^{-12} m^2/s to 2.8×10^{-11} m^2/s for [C_4C_1im][Cl]. To analyze the difference in diffusion behavior, the diffusing radii were calculated

for each water-IL system using the Stokes-Einstein relationship, and the heats of absorption were calculated for water sorption in the five ionic liquid systems using the Clausius-Clapeyron equation. The analysis concluded that as water concentration increases in the IL systems, the water-water interactions increase as more water molecules begin to hydrogen bond with each other. The analysis suggests that a few water molecules may form clusters with the [OAc] and [Cl] anions and that much larger water/BF_4^- clusters/networks may form in the [C_2C_1im][BF_4] system which increase in size with increasing water concentration. Therefore, even though viscosity of ILs decrease with increasing water concentration, the diffusion of water in [C_2C_1im][OAc], [C_4C_1im][OAc], and [C_4C_1im][Cl], increase, while the diffusion in [C_2C_1im][BF_4] decreases with increasing water concentration.

Studies are also emerging on water-IL mixtures and binary IL mixtures as a functional ionic liquid design to achieve certain properties. However, ternary mixtures of ILs and water are not commonly studied. This work presents an experimental study inspired by molecular simulation predictions for the phase behavior of water addition to equimolar mixtures of 1-ethyl-3-methylimidazolium bis(trifluoromethylsulfonyl)imide ([C_2C_1im][NTf_2]) + 1-ethyl-3-methylimidazolium acetate ([C_2C_1im][OAc]), [C_2C_1im][NTf_2] + 1-ethyl-3-methylimidazolium chloride ([C_2C_1im][Cl]), and [C_2C_1im][OAc]+[C_2C_1im][Cl]. The experiments verified the liquid-liquid phase separation which occurred when water was added to [C_2C_1im][NTf_2]:[C_2C_1im][OAc] and to [C_2C_1im][NTf_2]:[C_2C_1im][Cl] and verified that water addition to the miscible equimolar mixture of [C_2C_1im][OAc]:[C_2C_1im][Cl] does not induce a phase change.

Dedicated to my husband for his love and support

and to my brother for his resilient inspiration.

Acknowledgments

First and foremost, thank you Dr. Shiflett, for your mentoring, your trust, and for always challenging me to achieve more than I thought I could. You have expanded my knowledge of what I believe I can accomplish.

I would also like to thank the faculty and staff of the Department of Chemical and Petroleum Engineering at the University of Kansas for their teaching excellence and their kind help. Special thanks to Dr. David Griffin, Dr. Kevin Leonard, Rasha Faraj, and Dr. Justin T. Douglas and Sarah Neuenswander at the KU NMR Core Lab for their invaluable assistance.

Thank you to the Research and Graduate Programs in the School of Engineering for their sponsorship through the Graduate Ambassadors program and the Graduate Engineering Association. My sincerest gratitude for the travel award support, which allowed me to present my work at national conferences.

Thank you to my lab mates and friends; especially to Tugba Turnaoglu for listening to me and always encouraging me with positive words and actions of support. Thank you to Dr. David Minnick and Dr. William Gilbert for their guidance when I joined the Shiflett research group.

And finally, I would like to thank God and my loving family: my mom, my dad, my brother, and my husband, Jason Doresky; for their unrelenting support throughout this journey. It is because of you that I have reached this great milestone. I love you so dearly.

Additional Acknowledgements

Portions of this thesis have been previously published as articles in journals by the American Institute of Physics (AIP) Publishing and the American Chemical Society (ACS). The publishers allow the author to reuse published works in the author's thesis which the author writes and is required to submit to satisfy the criteria of degree-granting institutions.

Portions reused from:

1. Minnick, D. L.; Turnaoglu, T.; Rocha, M. A.; Shiflett, M. B. Review Article: Gas and Vapor Sorption Measurements Using Electronic Beam Balances. *J. Vac. Sci. Technol. A* **2018**, *36*, 050801-1–050801-14.
2. Rocha, M. A.; Zhang, Y.; Maginn, E. J.; Shiflett, M. B. Simulation and Measurement of Water-Induced Liquid-Liquid Phase Separation of Imidazolium Ionic Liquid Mixtures. *J. Chem. Phys.* **2018**, *149*, 164503.
3. (Submitted) Rocha, M. A.; Shiflett, M. B. Water Sorption and Diffusivity in $[C_2C_1im][BF_4]$, $[C_4C_1im][OAc]$, and $[C_4C_1im][Cl]$. *Ind. Eng. Chem. Res.* **2018**.

Table of Contents

List of Figures

List of Tables

Chapter 1: Introduction

1.1 Ionic Liquids

Over five thousand papers have been published on the topic of ionic liquids,[1] and interest continues to grow. Ionic liquids (ILs) are organic salts with melting temperatures defined below 373 K. The popularity of ionic liquids is due to many beneficial properties, such as negligible vapor pressure, high temperature stability, high electrical conductivity, and chemical tunability. ILs are typically composed of an organic cation and an organic or inorganic anion, therefore leading to the possibility of multiple ion combinations and, hence, the ability to design specific physicochemical properties. For example, the water solubility of ionic liquids can be modified by selecting a combination of specific cations and anions; the ionic liquid 1-butyl-3-methylimidazolium hexafluorophosphate [C_4C_1im][PF_6] is immiscible with water,[2] but the same cation paired with the acetate anion [C_4C_1im][OAc] is completely miscible.[3,4]

Due to the tunability of ionic liquids, many applications are possible, including chemical separations,[5] reaction media,[6] and energy conversion and storage.[7] Several of these applications currently use organic solvents, which may have undesirable environmental and safety properties, such as high volatility, toxicity, and flammability. Ionic liquids provide an alternative option which can be safer, greener, and more cost-effective than the use of conventional organic-based solvents.

1.2 Ionic Liquids and Water

The interest in ionic liquid applications has led to the need for studies on the effects of water on the physical and chemical properties of ionic liquids. Several researchers have observed that properties of ILs, such as density, viscosity, conductivity, selectivity, and reactivity, can be significantly affected by water presence in ionic liquids. For example, high water absorption into supported ionic liquid membranes (SILMs) have shown to hinder the permeability of gases such

as CO_2 due to hydrogen bonding of the IL with water.[8] This effect causes a decrease in performance for the use of SILMs for the separation of gases like CO_2/N_2. Although ILs can commonly be categorized as hydrophobic or hydrophilic, most ionic liquids are hygroscopic and will absorb moisture.[9–11] As water is a ubiquitous species, most water contamination occurs from atmospheric water sorption.

1.2.1 Water Measurement Techniques in ILs

Most work investigating the water-IL interactions has been performed by manual addition of water to the ionic liquid. A common and simple method to determine water concentration is using either coulometric or volumetric Karl Fischer titrations, where the coulometric method provides higher accuracy at concentrations of water below 5 wt.%. The use of Karl Fischer titration is accurate and convenient, but the process requires additional amounts of ionic liquid which cannot be reused. Nonetheless, as a single-measurement approach, Karl Fischer titration is certainly effective and the preferred choice for water analysis.

Nuclear magnetic resonance (NMR) spectroscopy is a conventional method used to detect impurities in ionic liquids. It has also been applied to observe interactions between water and ILs by analyzing mixtures of D_2O and ionic liquids. For example, Takamuku et al.[12] used ^2H NMR relaxation measurements to study the behavior of water in 1-ethyl-3-methylimidazolium tetrafluoroborate $[C_2C_1im][BF_4]$, and Cao et al.[13] used ^1H NMR measurements to study water and IL interactions for five functionalized imidazolium-based ionic liquids. NMR can be used for quantitative determination of species, either by observing a ratio of the components or by using a standard sample of known concentration. In Chapter 5, the application of NMR for the determination of water concentration for a ternary mixture of two ILs and water using the ratio

method will be discussed. In addition, an external standard was used to determine the concentration of the ionic liquids in the ternary mixture.

1.2.2 Vapor-Liquid Equilibria

There are only a few studies which have observed in situ sorption of water vapor into ILs where the temperature and pressure were recorded. Some researchers have used Near Infrared (NIR) spectroscopy to determine the concentration of water while observing the structural effects of water in ILs including, $[C_4C_1im][BF_4]$, $[C_4C_1im][NTf_2]$ (1-butyl-3-methylimidazolium bis(trifluoromethyl)sulfonylamide), and $[C_4C_1im][PF_6]$.[14] The benefit of using NIR is the ability to analyze water concentration in real-time, and in a non-invasive manner. However, due to the overlap of spectra for ILs and water, measurements by NIR require a high-performance apparatus and post-data deconvolution techniques.[14] Atmospheric Pressure X-ray Photoelectron Spectroscopy (APXPS) is another technique which is starting to be applied to study water in ILs, and while this also requires post-data treatment to remove background water spectra, the tool is extremely useful for observing the interactions of water at the ionic liquid interface within the top few nanometers of the sample. Therefore, the application of APXPS can be a beneficial tool for analysis of vapor sorption at the interface of ILs. Broderick et al.[15] have used APXPS to measure the concentration and interactions of water at the IL-water interface for 1-butyl-methylimidazolium acetate $[C_4C_1im][OAc]$ and have also performed a collaborative comparison against bulk sorption data investigated in the present study.

To measure the bulk water sorption in ionic liquids, a gravimetric technique has been developed. Examples include gravimetric methods in which the IL sample is placed on a balance in a temperature controlled space and use saturated salt solutions in proximity to the sample.[3,13,16] The salt solutions generate a specific relative humidity (RH) at a given temperature, while the RH,

temperature, and weight of the IL sample are measured as a function of time. A drawback in using this technique is the limitation of RH setpoints to the type of salt and the temperature at which the system is operated. Furthermore, the RH equilibration times are long, and this can affect the kinetic analysis. Some of these disadvantages have been overcome by replacing the saturated salt with a humidity generator.[17]

Humidity generating instruments achieve RH values using a combination of dry and water-saturated inert gas streams. The sample is exposed to the desired RH and weighed gravimetrically. This technique allows the instrument to quickly reach RH setpoints, which provides a better kinetics analysis of water sorption into ionic liquids. The instruments can regulate the temperature and humidity using feedback control and can be programmed to measure multiple temperature and RH isotherms. This type of equipment is beneficial for measuring the vapor-liquid equilibria of water into ionic liquids at precise atmospheric conditions. An IGAsorp microbalance, a Dynamic Vapor Sorption (DVS) analyzer designed by Hiden Isochema Ltd., was used to measure the absorption and desorption of water into five imidazolium-based ILs ionic liquids $[C_2C_1im][BF_4]$, $[C_2C_1im]$[TFES] (1-ethyl-3-methylimidazolium 1,1,2,2-tetrafluoroethanesulfonate), $[C_2C_1im][OAc]$, $[C_4C_1im][OAc]$, and $[C_4C_1im][Cl]$. Chapter 2 provides a description of the IGAsorp technique and the experimental details of the sorption measurements.

1.2.3 Liquid-Liquid Equilibria

There have also been studies investigating water-IL mixtures as a functional design method to create IL systems which achieve certain properties.[18,19] One example includes the extraction of biopolymers using binary mixtures of hydrophobic ionic liquids and water.[20] Ionic liquid mixtures, consisting of two ILs with a common cation or anion are also being studied.[21] Arce et al.[22] mixed two ILs with the same anions, trihexyl(tetradecyl)phosphonium chloride $[P_{6,6,6,14}][Cl]$ and 1-alkyl-

3-methylimidazolium chloride [$C_nC_n$im][Cl] (where the alkyl cations were shorter than the hexyl cation) and observed a broad range of temperature and compositions at which the system was biphasic. The phase separation was primarily a function of the large difference in cation structure. Kohno and Ohno,[19] investigated a mixture of hydrophobic and hydrophilic phosphonium-based ILs and found that several of those mixtures exhibited a Lower Critical Solution Temperature (LCST)-type phase separation, meaning the system was homogenous at low temperature, but separated into two liquids at higher temperatures. They were therefore able to manipulate the miscibility of the system by controlling the temperature. Ternary mixtures of ILs and water are not commonly studied except for the work of Kohno and Ohno.[19]

The effect of water addition on equimolar mixtures of [C_2C_1im][NTf_2]+[C_2C_1im][OAc], [C_2C_1im][NTf_2]+[C_2C_1im][Cl], and [C_2C_1im][OAc]+[C_2C_1im][Cl] will be discussed in Chapter 5. The results were originally predicted by molecular simulations and are confirmed by experiments performed in the present study. Furthermore, this work measures the concentration of each species in the resulting phases using several analytical techniques, including ^{1}H NMR, ^{19}F NMR, Karl Fischer, and Ion Chromatography.

1.3 Objectives

The main objectives of this research thesis are:

- to provide an overview of the gravimetric microbalance technique for measuring water absorption in ionic liquids (Chapter 2),
- to provide reproducible and accurate solubility data for water absorption and desorption in five ionic liquids, and to model water sorption using solution models (Chapter 3),

- to determine the diffusion coefficients of water sorption in ILs, and to evaluate the results using kinetic and thermodynamic analysis (Chapter 4) ,
- to highlight the phase equilibria effect of water addition to IL-IL mixtures (Chapter 5).

This thesis will end with overall conclusions and recommendations for future work (Chapter 6).

Chapter 2: Sorption Analysis Using the Gravimetric Technique

2.1 Introduction

The use of microbalance instruments for the solubility measurement of gases in ionic liquids has been proven reliable by several researchers.[23–26] The non-volatility of ILs makes them good candidates for this measurement technique. Anthony and coworkers[24,27] were the first to study CO_2 solubility in ILs using the Hiden IGA gravimetric microbalance, and researchers continue to use the gravimetric technique to measure solubility of a range of gases in ILs, including fluorocarbons, noble gases, inert gases, CO_2, H_2, and O_2, to name a few.[25,28]

Water solubility has also been measured in a few ILs by Anthony et al.[23] who used the IGA microbalance and a leak valve which allowed water vapor into the sample chamber. However, a disadvantage of this setup was the possibility of water condensation in the balance electronics which could affect the results. In 1997, Hiden Isochema Ltd. (then Hiden Analytical) introduced the IGAsorp, a Dynamic Vapor Sorption (DVS) instrument, specifically designed to measure the sorption of vapor into materials. The IGAsorp microbalance uses nitrogen as the carrier gas and overcomes the water condensation issue by using a constant flow of nitrogen gas on the microbalance parts with a purge located between the sample chamber and the balance chamber.

The IGAsorp microbalance has been used for quality control studies in the pharmaceutical,[29] electronics,[30–32] and construction industries[33,34] to understand the impact of moisture on water sensitive products. Other groups,[35–37] have also used the IGAsorp to study the sorption of water in ILs. Dahi et al. compared the effects of different cations and anions on water vapor sorption over a wide range of water activity.[35] They also used the IGAsorp with organic solutes to investigate the separation capabilities of supported ionic liquid membranes for water and other organic vapors including cyclohexane and ethanol.[36] In summary, gravimetric analysis is a

highly accurate experimental method for assessing the interaction between water and materials, and it is the method of choice for this research.

2.2 IGAsorp Overview

The Hiden IGAsorp is an ultra-sensitive electrobalance with 0.05 μg resolution and a weighing capacity limit of 1 g. It operates at ambient pressure and has a temperature working range of 278 K to 573 K (with the optional pre-heater). The balance is composed of a counterweight side (*j*) and a sample side (*i*), as shown in Figure 2.1. On each end of the balance beam, a tungsten hook connects to a gold chain. At the opposite end of each gold chain, a second tungsten hook connects to either the counterweight or the sample container. The counterweight is made of stainless-steel wire, and the sample cups used in this study were Pyrex® glass bulbs (as shown in Figure 2.2a). For solid samples, the sample container is a cone-shaped mesh basket (Figure 2.2b) which allows vapor transport through all solid faces.

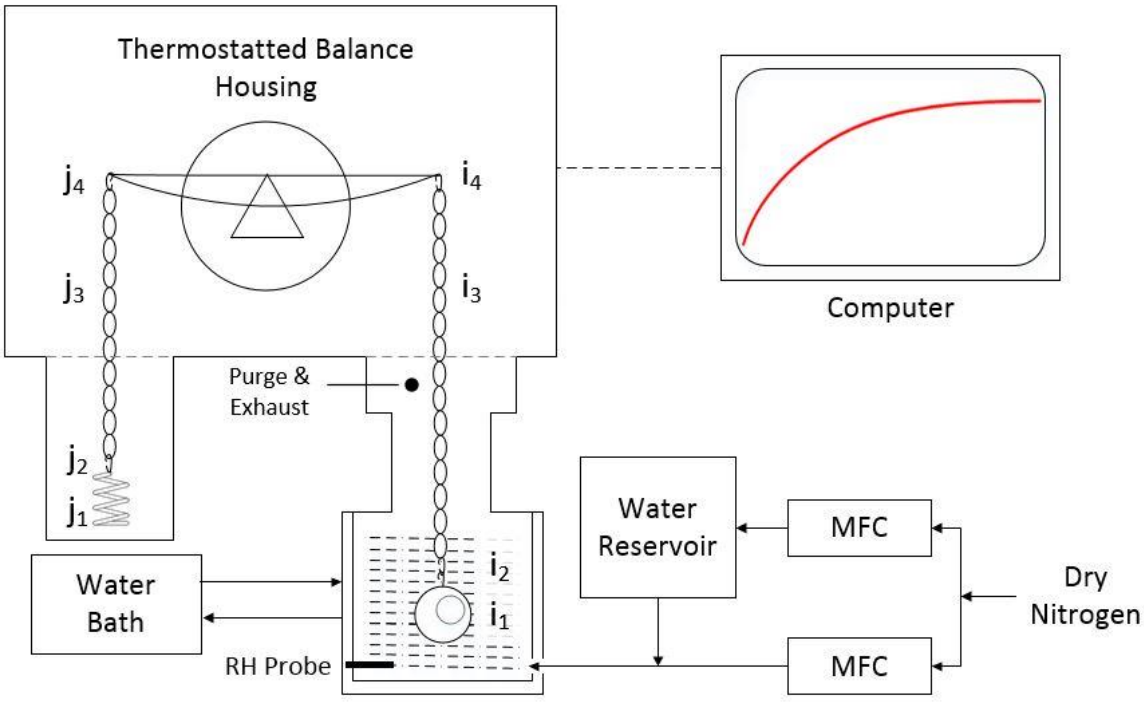

Figure 2.1. Hiden IGAsorp schematic. Symbols *i* and *j* are detailed in Table 2.1. MFC = Mass Flow Controller

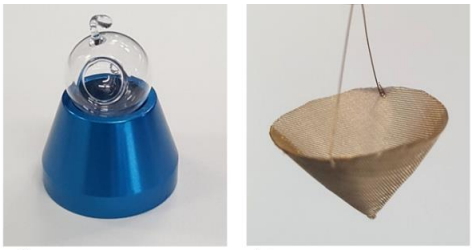

Figure 2.2. Sample containers for IGAsorp. Container (a) is used for liquids, and container (b) is used for solids.

The relative humidity in the IGAsorp is controlled through a measured combination of dry and wet nitrogen streams. Dry nitrogen enters the instrument and is divided into streams directed by the two mass flow controllers (MFC). The IGAsorp has a pressure relief set at 300 kPa to prevent damaging the MFCs. One of the streams directs nitrogen gas through a water reservoir, where the gas is saturated with the water at a set temperature controlled by the water bath. The wet and dry stream combine, and the mixed flow is directed to the sample chamber. A relative humidity sensor (Vaisala HMT333), with measurement accuracy of ± 1 % RH (at 0-90 % RH) and ± 2 % (at 90-95 % RH), and a platinum RTD (± 0.1 K) located within the sample chamber provide PID feedback control to the MFCs at ± 0.1 % RH regulation accuracy.

The instrument uses different “climate modes” to achieve a range of relative humidity values. It is important to note that the sample chamber can be controlled by the water bath or by the heater (which is included with the IGAsorp-XT or as an accessory to the IGAsorp). Temperature regulation for the water bath is 278 K to 353 K (± 0.05 K), and the heater can reach temperatures as high as 623 K (± 1 K). The water reservoir is regulated only by the water bath.

The conventional option is Climate mode, which uses a total gas flowrate of 250 ml/min and is optimal for measuring relative humidity values ranging from 2 % to 95 % RH. Climate mode operates by controlling the sample chamber and the water reservoir at the same temperature with the water bath. Therefore, when the system is set to a specific temperature and % RH in the sample

chamber, the percent of wet flow rate (wet flow/total flow x 100 %) is adjusted to that value. For example, if the desired condition at the sample chamber is 5 % RH at 303.15 K, the wet flow rate is set to about 5 %. The % RH is a function of the vapor pressure of water (P_{H2O}) divided by the saturation pressure (P^0) at a specific temperature as shown in Eq. 2.1. The saturated vapor pressure of water is calculated using REFPROP v9.1,[38] which is based on the work of Wagner and Pruss.[39]

$$\% RH = \frac{P_{H2O}}{P^0(T)} \times 100\ \% \tag{2.1}$$

At T = 303.15 K and 5 % RH set point, the vapor pressure of water in the reservoir and for the wet stream is 4.2 kPa, and the desired water partial pressure in the sample chamber is (5/100 x 4.2 kPa =) 0.21 kPa. Therefore, in order to generate water vapor at 0.21 kPa, the total flow rate should be composed of (0.21 kPa/4.2 kPa x 100 %=) 5 % wet flow rate and 95 % dry flow rate.

The Climate XT mode should be used when working at low humidity conditions (0 – 5 % RH). It uses a different process than the Climate mode to achieve the desired low humidity set points. Climate XT mode operates at 500 ml/min, controls the temperature of the water reservoir using the water bath, and controls the sample chamber temperature using the heater. This method allows the IGAsorp to reach lower humidity values without having to go below the IGAsorp's minimum wet flowrate of 2 %. The instrument achieves this by having the reservoir at a lower temperature and lower saturation pressure than at the sample chamber. Therefore, the partial pressure of water must be higher at the reservoir to achieve the desired % RH, which requires the wet flow rate to be higher than it would have been using the normal Climate mode. For example, if the desired RH set point is 0.8 % at 303.15 K, the sample chamber will be controlled at 303.15 K, and the water reservoir will be set at a lower temperature, for example 285.15 K. At 303.15 K and 0.8 % RH, the desired vapor pressure of water is (0.8/100 x 4.2 kPa =) 0.034 kPa, and the vapor pressure of water in the reservoir is 1.4 kPa at 285.15 K. To achieve a 0.034 kPa water vapor

pressure in the sample chamber, the total flow would have to be (0.034 kPa/1.4 kPa x 100 % =) 2.4 % wet flow and 97.6 % dry flow. The operating software for the Hiden microbalances, the HIsorp program, intelligently controls the IGAsorp reservoir temperature to achieve the target flow rate and relative humidity conditions.

In addition to data acquisition and control, HIsorp can also predict sorption equilibrium in real time. The default method used is the Linear Driving Force exponential model, shown in Eq. 2.2, where y (mg) is the total weight of the sample at time t (min), y_0 (mg) is the initial weight, Δy (mg) is the weight change, t_0 (min) is the initial time, and k is the kinetic rate constant (min^{-1}). The standard deviation using this prediction is low (<< 0.01 mg).

$$y = y_0 + \Delta y[1 - e^{-(t-t_0)k}] \tag{2.2}$$

At low T and high % RH conditions, the time to reach equilibrium in IL systems could be over 50 hours; therefore, the LDF model was used in this study to predict the absorption/desorption solubility of water in ILs. The slow sorption was expected due to the high viscosity of the ionic liquids, the ambient pressure driving force, and most importantly, there was no mixing, such that the equilibrium was purely diffusion-driven with no convection.

2.3 Data Corrections

Microgravimetric balances are sensitive instruments, and measurement error can easily be introduced through changes in buoyancy, temperature, and partial pressure. Aerodynamic drag forces and the changes in the sample volume can also affect the microbalance results. Not adjusting for these errors may lead to large inaccuracies (0.1 – 5 mg),[26] fortunately the IGAsorp is designed to minimize these errors.

The electrobalance housing is maintained at 343 K (± 0.05 K) and is constantly purged with dry nitrogen to reduce any effects due to temperature and humidity changes near the beam

balance and electronics. A correction for additional effects in the balance, such as buoyancy forces, volume expansion, and drag forces, is applied using a force balance and assuming additive molar volumes. Three forces act on each balance component: a gravimetric force (F_G), a drag force (F_D), and a buoyancy force (F_B). F_G and F_D are downward forces, where F_G is the effect of gravity on the objects, and F_D is the drag force which acts in opposing direction to the gas flow (in the IGAsorp, gas flow occurs from the bottom of the sample chamber directed upwards). F_B is the upward force exerted on an object and is equivalent to the weight of fluid displaced. Using Archimedes' principle, buoyancy can be calculated using Eq. 2.3,

$$F_B = Buoyancy = gV_i\rho_g(T, RH) = g\frac{m_i}{\rho_i}\rho_g(T, RH) \tag{2.3}$$

Equation 2.3 shows F_B is a function of temperature and the concentration of the vapor displaced, which is directly related to the % RH. The density of the surrounding gas, ρ_g, is estimated using an ideal gas approximation as shown in Eq. 2.4,

$$\rho_g = \frac{P_{H_2O}MW_H + P_{N_2}MW_N}{RT} \tag{2.4}$$

where MW_i is the molecular weight of species i, R is the ideal gas constant, and P_{H_2O} and P_{N_2} are partial pressures of water and nitrogen, respectively. The partial pressure of water was determined in Eq. 2.1 using the RH relationship. A force balance on the components shown in Figure 2.1 leads to Eq. 2.5, where F_{Meas} is the weight reported and measured by the IGAsorp. The correction factor, C_f, is a function of T and % RH, which is applied to drive F_{Meas} to approach zero when the sample container is empty (i.e., when $F_M(s)$ and $F_M(a)$ are zero).

$$F_{Meas} = \sum F_M(i_N) - \sum F_M(j_N) + F_M(s) + F_M(a) - \left(\sum F_B(i_N) + F_B(s) + F_B(a)\right) + \sum F_B(j_N) + F_D + C_f \tag{2.5}$$

In theory, drag effects may be calculated using the aerodynamic or viscous drag equations depending on the Reynolds number, however, in practice this study bundles the drag effects with the correction factor C_f.

The IGAsorp procedure is as follows, the microbalance is loaded with the empty sample container and counterweight of choice. The balance is tared at room temperature approximately 295 K, 0.1 MPa, and 40 % RH. Next, the isotherms begin with a desired temperature and a 0 % RH set point to determine a "dry" container mass. The isotherms are performed on the empty container at the same *T* and % RH conditions planned for the IL samples. The empty container mass data are used to determine the C_f value for each isotherm as described later in this chapter. Once the empty cup isotherms are complete, a new experiment is started, and the microbalance is again tared with the empty container. Next, the IL is loaded into the container to begin pre-treatment. Once the pre-treatment is complete, the sorption experiments begin by first measuring an "uncorrected dry" IL sample mass at 0 % RH and a set *T* .

Based on the operating procedures, the force balance is further simplified with the assumption that when the balance is tared, $F_M(i_N) = F_M(j_N)$. However, it is worthwhile to note that the balance is tared at a set point (approx. 295 K and 40 % RH) which is different than the "dry" container mass conditions (at 0 % RH and a set *T*). Therefore, $F_M(i_N)$-$F_M(j_N)$ is replaced with Z_C (or zero correction) which is equal to the "dry" container mass measured at 0 % RH and a set *T*. Substituting the buoyancy and gravimetric terms and canceling out the gravity term in Eq. 2.5, results in Eq. 2.6:

$$m_{Meas} = Z_C(T) + m_s + m_a - \sum_i \frac{m_i}{\rho_i}\rho_g(T_i, RH) - \frac{m_s}{\rho_s}\rho_g(T_s, RH) - \frac{m_a}{\rho_a}\rho_g(T_a, RH) - \sum_j \frac{m_j}{\rho_j}\rho_g\left(T_j, RH\right) + C_f(T_s, RH) \quad (2.6)$$

Equation 2.6 includes the mass measured by the IGAsorp (m_{Meas}), the sample IL mass (m_s), the absorbed water mass (m_a), and the mass of components *i* and *j*, all listed in Table 2.1 with the respective temperatures and densities. The density of all ILs were determined from literature (see Appendix A). The first step in using Eq. 2.6 is to solve for the C_f value, using the empty container isotherm measurements. The variable Z_c is the "dry" container mass at the specific isotherm temperature evaluated, m_s and m_a are both zero, and in theory m_{Meas} should be equal to zero, but, due to instrument error, it most likely is not. Therefore, a linear (slope and intercept) function (C_f) is fit to the m_{Meas} data as a function of RH for each isotherm.

The next step is to determine the "corrected dry" IL sample mass (m_s) for a specific isotherm temperature. The measured "uncorrected dry" IL mass is used in Eq. 2.6 as m_{Meas}, where m_a is zero, and the term Z_c is equal to the "dry" container mass at the same temperature. All other variables are known, and Eq. 2.6 is solved iteratively for m_s.

Finally, the determined values C_f, Z_c, and m_s are used in Eq. 2.6 to calculate the mass of water absorbed (m_a) at RH values > 0 %. Due to the low solubility of nitrogen in ionic liquids (0.001 mole fraction N_2 in $[C_2C_1im][BF_4]$ at 298.15 K and 101 kPa),[40,41] the mass absorbed (m_a) is assumed to be pure water.

Table 2.1. IGAsorp components

Symbol	Component	Material	Weight (g)	Density (g/cm^3)	Temperature (K)
s	Sample	Variable	m_s	ρ_s	Sample Temp
a	Interacted Vapor	Water	m_a	ρ_a	Sample Temp
i_1	Sample Container Bulb	Pyrex	varies	2.23	Sample Temp
i_2	Lower Sample Hook	Tungsten	0.0057	19.04	Sample Temp
i_3	Sample Chain	22 Ct. Gold	0.0930	11.10	Temp Profile i
i_4	Sample Side Balance Hook	Tungsten	0.0059	19.04	343.15
j_1	Counterweight (CW)	316 SS	varies	7.89	333.15
j_2	Lower CW Hook	Tungsten	0.0057	19.04	333.15
j_3	CW Chain	22 Ct. Gold	0.0650	11.10	Top half = 338. 15 Bottom half = 333.15
j_4	CW Side Balance Hook	Tungsten	0.0058	1.04	343.15

The balance housing is controlled and maintained at 343.15 K ± 0.1 K, the counterweight chamber is not temperature controlled but is often at approximately 333.15 K, and the sample chamber temperature is controlled using the water bath or the heater. Therefore, a temperature profile is present along both sides of the balance, as reported in Table 2.1. It is estimated that the top section of the counterweight gold chain is at 338.15 K, and the bottom half at 333.15 K. The sample side gold chain temperature profile is divided into two zones. The temperature of the top section is an average between the sample temperature (T_{sample}) and the balance chamber temperature (343.15 K). The bottom section is at T_{sample}. In addition, there is also a humidity profile, where the counterweight side, the balance housing, and the top third section of the sample side chain are in pure nitrogen gas. The bottom two-thirds of the sample side gold chain are assumed to be at the same relative humidity as the sample. The temperature and RH profile for the balance components are shown in Figure 2.3.

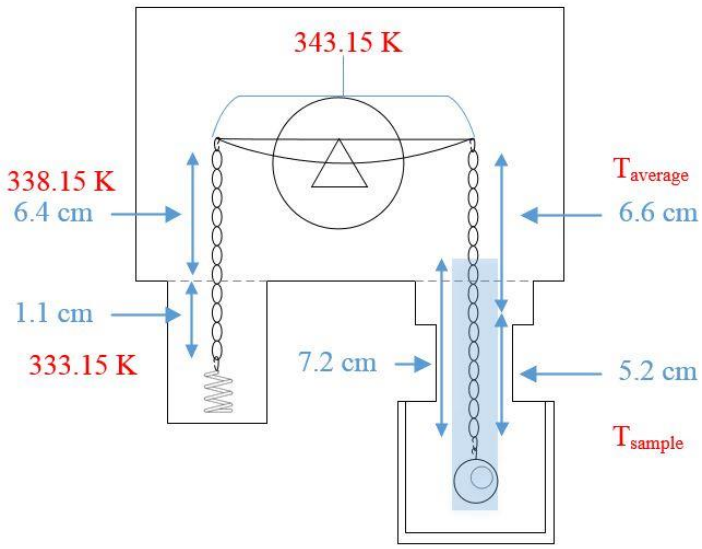

Figure 2.3. Temperature profiles on IGAsorp components. The shaded region indicates the sections which are assumed to be at the same RH value as the sample. The unshaded areas are assumed to be at 0 % RH or pure nitrogen.

2.4 Experimental Details

The solubility of water was measured in five ionic liquids, namely: 1-ethyl-3-methylimidazolium tetrafluoroborate [C_2C_1im][BF_4] (≥ 98.5% purity, Fluka, Lot and Filling Code 1084445 11106247, CAS no. 143314-16-3), 1-butyl-3-methylimidazolium acetate [C_4C_1im][OAc] (> 95% purity, Fluka, Lot and Filling Code B.13687 11707B11, CAS no. 284049-75-8), 1-butyl-3-methylimidazolium chloride [C_4C_1im][Cl] (> 99.0% purity, Lot and Filling Code 1084617 22905013, CAS no. 79917-90-1),1-ethyl-3-methylimidzolium 1,1,2,2-tetrafluoroethanesulfonate [C_2C_1im][TFES] (99 % purity, Lot and Filling Code IL-0232-HP-0050 I00113.1.3, CAS no. 880084-63-9), 1-ethyl-3-methylimidazolium acetate [C_2C_1im][OAc] (> 98 % purity, Lot and Filling Code N00952.7.Inc-IL-0189, CAS no. 143314-17-4). The sorption studies used reverse osmosis water (15 mΩ.cm at 298 K) for the reservoir water. Nitrogen gas (Matheson grade < 1 ppm H_2O, Lot code 7727-37-9) was used and a molecular sieve trap (Restek® 22015, Lot Code

393152-22015) was installed at the inlet to the microbalance instrument to remove trace amounts of water from the nitrogen gas.

Karl Fischer coulometric titration (Mettler Toledo DL36 Karl Fischer Coulometric Titrator) was used to measure the as-received water content for each ionic liquid. Prior to every IL measurement, the accuracy of the Karl Fischer (KF) instrument was checked with a water standard (94 ± 10 ppm H_2O, Apura®, Merck KGaA, Prod. no. 1.88050.0010, Lot code HC61276950). The water concentrations in $[C_2C_1im][BF_4]$, $[C_2C_1im][TFES]$, $[C_2C_1im][OAc]$, $[C_4C_1im][OAc]$, and $[C_4C_1im][Cl]$ were determined to be 249 ppm ± 13 ppm, 489 ± 93 ppm, 4802 ± 125 ppm, 2200 ppm ± 400 ppm, and 4636 ± 53 ppm, respectively. The KF measurement for water content in $[C_4C_1im][OAc]$ was performed after drying the system at 323.15 ± 1 K under vacuum and with stirring for 7 days. The chemical name, molecular weights, decomposition temperatures, and the chemical structures of the ILs measured are shown in Table 2.2.

Table 2.2. Name, molecular weight, decomposition temperature, and structure of ionic liquids investigated

Name	Abbreviation	MW	T_{Decomp}	Structure
1-ethyl-3-methylimidazolium tetrafluoroborate	$[C_2C_1im][BF_4]$	197.97	555.9 K[42]	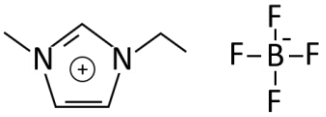
1-ethyl-3-methylimidazolium 1,1,2,2-tetrafluoroethanesulfonate	$[C_2C_1im][TFES]$	292.25	341.0 K[43]	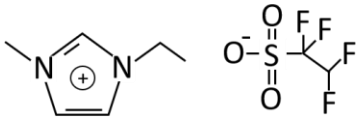
1-ethyl-3-methylimidazolium acetate	$[C_2C_1im][OAc]$	170.21	481.4 K[44]	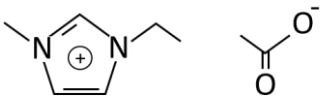
1-butyl-3-methylimidazolium acetate	$[C_4C_1im][OAc]$	198.26	496.9 K[44]	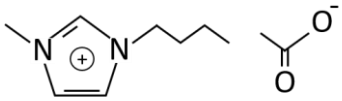
1-butyl-3-methylimidazolium chloride	$[C_4C_1im][Cl]$	174.67	507.2 K[45]	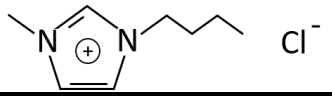

The temperatures and relative humidity values at which the ILs were measured varied by IL and are listed in Table 2.3.

Table 2.3. Experimental conditions at which the ionic liquids were measured

Ionic Liquid	Temperature (K)[a]	Relative Humidity (%)[b]
$[C_2C_1im][BF_4]$	298.15; 303.15	0; 10.67; 30.67; 50.67; 60.67; 70.67; 80.67
$[C_2C_1im][TFES]$	273.15; 303.15; 313.15	0; 1; 5; 10; 15; 20; 25
$[C_2C_1im][OAc]$	273.15; 303.15; 313.15	0; 2.5; 5; 10; 15; 20; 25
$[C_4C_1im][OAc]$	294.85; 303.15; 315.15	0; 1.47; 1.67; 5.67; 10.67; 15.67; 20.67; 25.67
$[C_4C_1im][Cl]$	283.15; 295.15; 303.15	0; 1.67; 5.67; 10.67; 15.67; 20.67; 25.67

[a] Uncertainty in the temperature measurements are ± 0.01 K.
[b] Uncertainty in the relative humidity measurements is ± 1.00 % RH, except for the 0 % set point. Some data have the decimal 0.67 due to a humidity calibration correction.

2.5 Experimental Methodology

Approximately 60 mg of IL were loaded into a clean Pyrex® glass container at room temperature (295 ± 1 K) and room humidity (40 ± 1%) and placed in the IGAsorp. This process was done as quickly as possible to minimize absorption of atmospheric water into the ionic liquid (< 5 minutes). Prior to every isothermal sorption measurement, a pre-treatment isotherm was performed at 348.15 ± 0.01 K and 0 % RH for 15 hours in the IGAsorp to remove any traces of residual water. The IL decomposition of $[C_2C_1im][TFES]$ is below 348 K (see Table 2.2), therefore, the pre-treatment temperature was set to 298 ± 1 K for the 293.15 K and 303.15 K isotherms, and the pre-treatment temperature was set to 318.15 K for the 303.15 K isotherm.

Each relative humidity set point had a minimum time-out of 3 hours, and in some cases, a maximum time-out of 100 hours to allow ample time for vapor-liquid equilibrium to be achieved. Moreover, the IGAsorp software, HIsorp, can predict the equilibrium water solubility using real-time weight vs. time data with the LDF model shown previously in Eq. 2.2. For further details on the methodology see Appendix A.

2.6 Conclusion

The gravimetric technique has been shown to be a reliable method for sorption of gases and vapors in ionic liquids. This research used the Hiden IGAsorp microbalance for measurement of solubility of water in five ionic liquids. This study included a correction factor for the buoyancy effects on the balance components. In addition, a detailed force balance on the components was described and included the effects of temperature and relative humidity.

Chapter 3: Solubility Results and Thermodynamic Modeling

3.1 Introduction

Measurements of in situ water absorption and desorption in five ionic liquids (1-ethyl-3-methylimidazolium tetrafluoroborate [C_2C_1im][BF_4], 1-ethyl-3-methylimidazolium 1,1,2,2-tetrafluoroethane-1-sulfonate [C_2C_1im][TFES], 1-ethyl-3-methylimidazolium acetate [C_2C_1im][OAc], 1-butyl-3-methylimidazolium acetate [C_4C_1im][OAc], and 1-butyl-3-methylimidazolium chloride [C_4C_1im][Cl]) were made using the IGAsorp gravimetric microbalance at temperatures ranging from 283.15 K to 315.15 K and percent relative humidity (% RH) 0 % to 70 % at 101 kPa. The non-random two liquid (NRTL) activity coefficient model was used to correlate the solubility data, and the energy parameters (α, τ_{12}, and τ_{21}) provided some insight into the solubility differences observed for these systems.

3.2 Sorption Isotherms

The first ionic liquid studied was [C_2C_1im][BF_4], where water vapor sorption was measured at 298.15 K and 303.15 K at RH values ranging from 0 % to 70 %. The solubility results are provided in Appendix A. A comparison of the water absorption and desorption as a function of the partial pressure of water is shown in Figure 3.1a. The data measured in this study show no sign of hysteresis (i.e., the absorption and desorption results are the same), indicating the sorption mechanism of water into [C_2C_1im][BF_4] is physical. Plotting the solubility results as a function of RH removes the effect of temperature on solubility and the data lie on the same curve, as shown in Figure 3.1b.

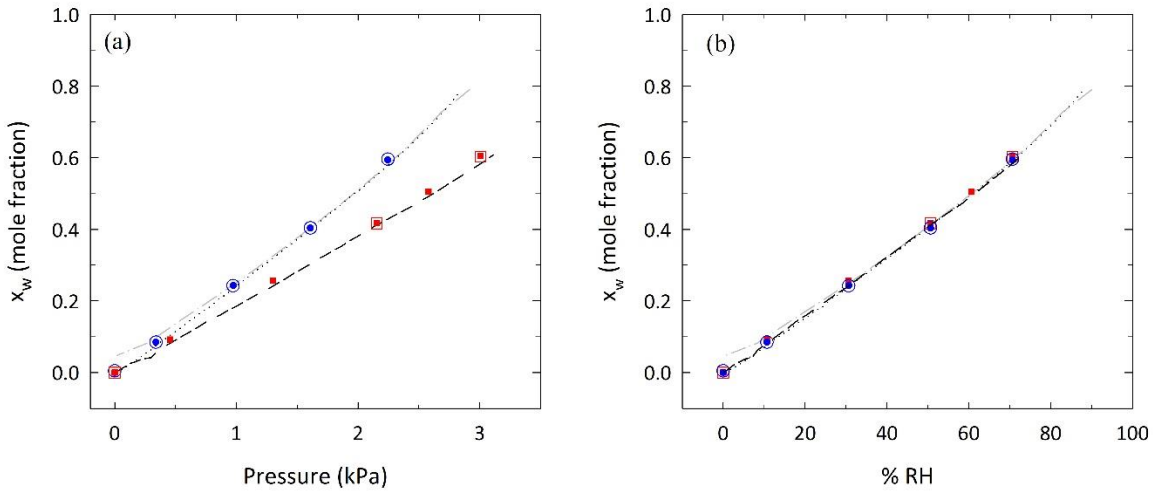

Figure 3.1. Absorption and desorption isotherms of water in $[C_2C_1im][BF_4]$ at 298 K and 303 K as (a) a function of partial pressure of water and (b) a function of relative humidity. Data at 298 K is shown in blue circles and data at 303 K is shown in red squares. Filled symbols represent absorption and open symbols represent desorption. Uncertainties for the data measured in this work were determined to be < 0.1 mol%. Black dotted and dashed lines are the fitted absorption data measured by Takamuku et al. and the grey dashed line is the fitted desorption data by Takamuku et al.[12]

The experimental absorption and desorption measurements were compared to previously published data by Takamuku et al.[12] who used a similar instrument; a Rubotherm gravimetric balance. The Rubotherm instrument is a magnetic suspension balance which measures the weight of a sample in a closed chamber using an external microbalance, where the environment surrounding the sample is not in direct contact with the balance. This allowed the Takamuku group to measure the sorption of water in $[C_2C_1im][BF_4]$ using only water vapor and no inert gas carrier, such as nitrogen which was used in the present work. A comparison of the results shows the data measured in this study and those measured by Takamuku et al.[12] are in close agreement (%AARD < 4.6 %), as shown in Figure 3.1. The slight deviation in the results at higher humidity can be attributed to the buoyancy correction applied in the current analysis. The comparison confirms that using nitrogen as a carrier gas has no effect on the solubility of water in $[C_2C_1im][BF_4]$ and that the IGAsorp is an accurate and reliable instrument for measuring water sorption in ionic liquids. The solubility of N_2 in $[C_2C_1im][BF_4]$ has been measured to be quite low (0.001 mole fraction N_2

at 298.15 K and 101 kPa);[40] therefore, the effect on the water solubility measurement was expected to be negligible. The solubility of N_2 in the other ionic liquids measured in this study was expected to be within the same range and has no effect on the water solubility measurements.[41]

The measured solubility of water in $[C_2C_1im][TFES]$, $[C_2C_1im][OAc]$, $[C_4C_1im][OAc]$ and $[C_4C_1im][Cl]$ as a function of water partial pressure and % RH are shown in Figures 3.2 – 3.5, respectively. As expected, the concentration of water in the ionic liquids increases with increasing relative humidity (or partial water vapor pressure) and decreases with increasing temperature as shown in Figures 3.1-3.5. In addition, little to no difference was observed between absorption and desorption measurements as shown in Figures 3.1a-3.5a, which indicates that the sorption process is physical and reversible. When the solubility data are plotted as a function of % RH, the isotherms converge and overlap, as shown in Figures 3.1b-3.5b. The absorption of water depends only on the relative humidity which incorporates the effect of temperature via the saturation pressure of water P^0 as shown in Eq. 2.1 (see Chapter 2).

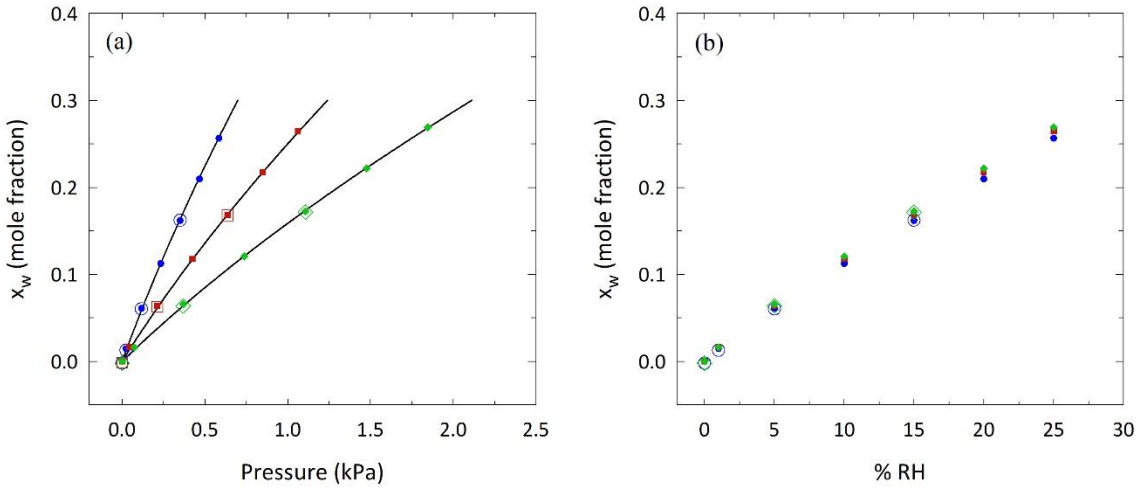

Figure 3.2. Absorption and desorption isotherms of water in $[C_2C_1im][TFES]$ at 293.15 K, 303.15 K, and 313.15 K as (a) a function of partial pressure of water and (b) a function of relative humidity. Blue circles represent data at 293.15 K; red squares represent data at 303.15 K; green diamonds represent data at 313.15 K. Filled symbols represent absorption and open symbols represent desorption. The black solid lines are calculated with the NRTL equation. Uncertainties are < 0.1 mol%.

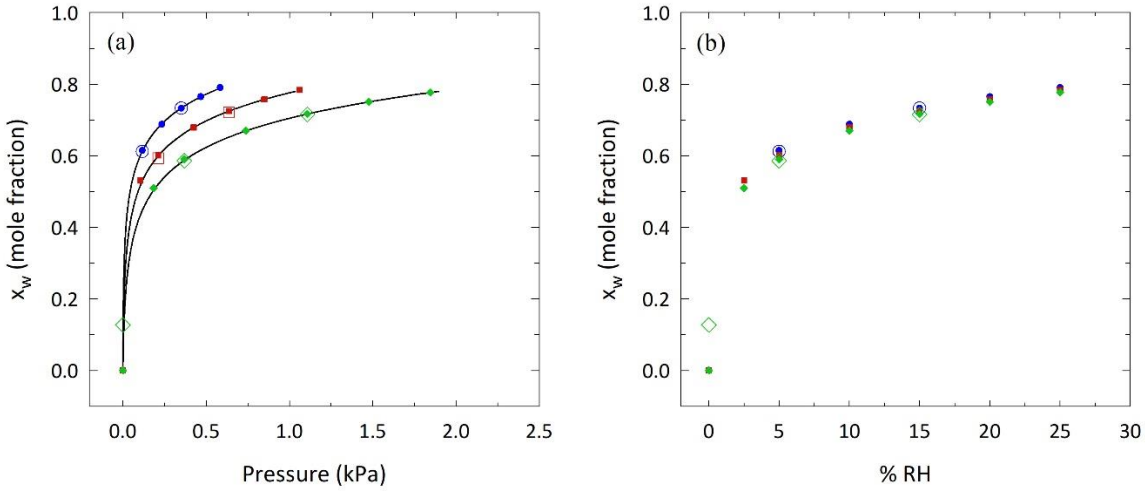

Figure 3.3. Absorption and desorption isotherms of water in [C_2C_1im][OAc] at 293.15 K, 303.15 K, and 313.15 K as (a) a function of partial pressure of water and (b) a function of relative humidity. Blue circles represent data at 293.15 K; red squares represent data at 303.15 K; green diamonds represent data at 313.15 K. Filled symbols represent absorption and open symbols represent desorption. The black solid lines are calculated with the NRTL equation. Uncertainties are < 0.1 mol%.

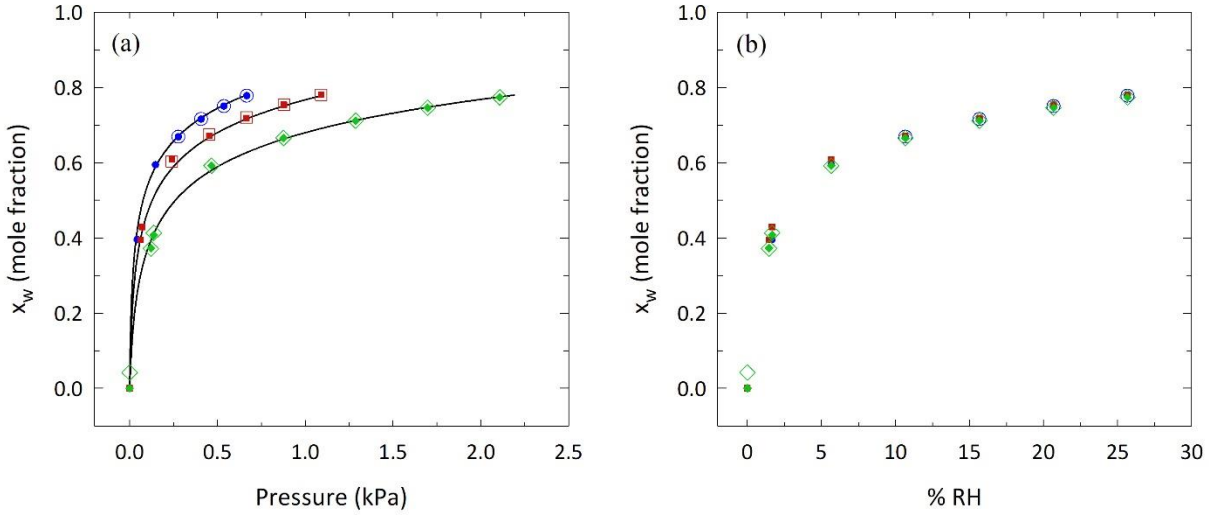

Figure 3.4. Absorption and desorption isotherms of water in [C_4C_1im][OAc] at 294.85 K, 303.15 K, and 315.15 K as (a) a function of partial pressure of water and (b) a function of relative humidity. Blue circles represent data at 294.85 K; red squares represent data at 303.15 K; green diamonds represent data at 315.15 K. Filled symbols represent absorption and open symbols represent desorption. The black solid lines are calculated with the NRTL equation. Uncertainties are < 0.1 mol%.

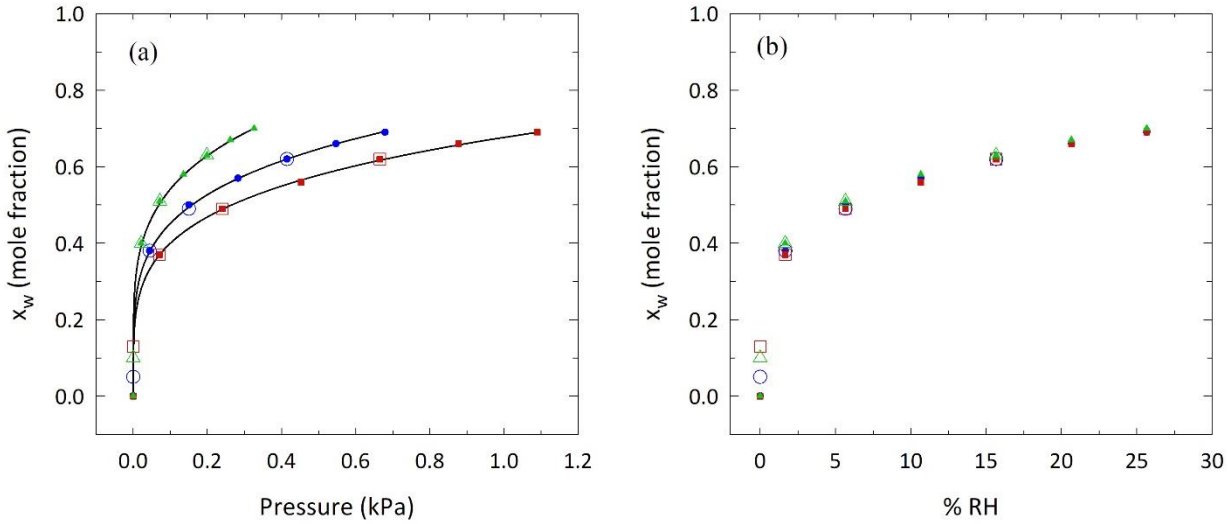

Figure 3.5. Absorption and desorption isotherms of water in [C_4C_1im][Cl] at 283.15 K, 295.15 K, and 303.15 K as (a) a function of partial pressure of water and (b) a function of relative humidity. Green triangles represent data at 283.15 K; blue circles represent data at 295.15 K; red squares represent data at 303.15 K. Filled symbols represent absorption and open symbols represent desorption. The solid black lines are calculated with the NRTL equation. Uncertainties are < 0.1 mol%.

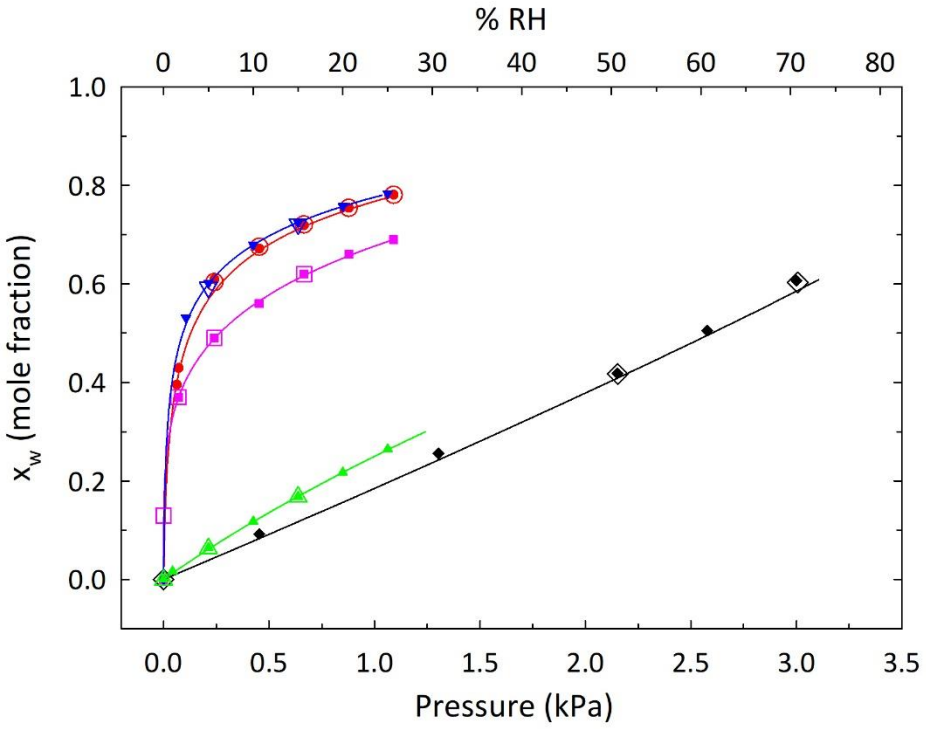

Figure 3.6. Solubility data comparison for [C_2C_1im][BF_4], [C_2C_1im][TFES], [C_2C_1im][OAc], [C_4C_1im][OAc], and [C_4C_1im][Cl] at 303.15 K. Black diamonds are [C_2C_1im][BF_4], green triangles are [C_2C_1im][TFES], blue inverted triangles are [C_2C_1im][OAc], red circles are [C_4C_1im][OAc], and pink squares are [C_4C_1im][Cl]. Filled symbols represent absorption, and open symbols represent desorption. The solid lines are calculated with the NRTL equation. The NRTL fit for [C_2C_1im][BF_4] was developed using experimental data from Takamuku et al.[12]

A comparison of the water solubility at 303.15 K in all five ionic liquids indicates that the solubility of water is highest in $[C_2C_1im][OAc]$ and lowest in $[C_2C_1im][BF_4]$, where the water absorption in $[C_2C_1im][OAc]$ is higher than that of $[C_2C_1im][BF_4]$ even at much lower relative humidity (i.e., 25 % RH). This is not surprising as the cations studied here ($[C_2C_1im]$ and $[C_4C_1im]$) have similar chain lengths and the anions have the primary effect on water solubility. It is well known that the acetate anion is a very hydrophilic ion, and although the BF_4^- anion has been often referred to as "hydrophobic," ILs with BF_4^- anions have been observed to uptake significant amounts of water (>12 wt.%).[46] Based on the water sorption measurements in this study, the strength of the water-IL interactions are observed in the order: $[C_2C_1im][OAc]$ > $[C_4C_1im][OAc]$ > $[C_4C_1im][Cl]$ > $[C_2C_1im][TFES]$ > $[C_2C_1im][BF_4]$. The higher water solubility in $[C_2C_1im][OAc]$ than in $[C_4C_1im][OAc]$ was expected as the $[C_2C_1im]$ cation has a shorter alkyl chain than the $[C_4C_1im]$, and it has been observed in literature that the hydrophilicity of ionic liquids decrease with increasing alkyl chain length.[46]

The shape of the isotherms is another clear difference between the water-IL systems, shown in Figure 3.6. The isotherms of H_2O-$[C_2C_1im][OAc]$, H_2O-$[C_4C_1im][OAc]$, and H_2O-$[C_4C_1im][Cl]$ exhibit typical Langmuir-type isothermal behavior, while the isotherms of H_2O-$[C_2C_1im][BF_4]$ appear to be essentially linear over the measured RH range (0 – 70 % RH). The isotherms of H_2O-$[C_2C_1im][TFES]$ in general also show a linear behavior over the measured RH range (0 – 25 %), but the higher temperatures appear to indicate a slight concave curvature at the higher RH values. This is seen more clearly in the NRTL fits shown in Figures 3.2 and 3.6.

3.3 Thermodynamic Modeling

The solubility of water in the five ionic liquids was modeled using the NRTL activity coefficient model which has been used successfully to fit other water-ionic liquid systems.[35,47,48] The NRTL model can be applied to the current systems because the measured pressures are low ($P \leq 101.325$ kPa) and the vapor pressure for the ionic liquid is assumed to be negligible ($P_2 = 0$). The calculation begins with the vapor-liquid equilibrium of a binary mixture (Eq. 3.1) where *i* represents the species (1) water and (2) IL, γ is the activity coefficient, *x* is the mole fraction of *i* in the liquid phase, *f/P* is the fugacity coefficient, and *y* is the mole fraction of *i* in the gas phase.

$$\sum_{i=1}^{2} x_i \gamma_i(T,P,x) P_i^{sat}(T) \left(\frac{f}{P}\right)_{sat,i} = P \sum_{i=1}^{2} y_i \left(\frac{f}{P}\right)_i \tag{3.1}$$

Equation 3.1 can be simplified assuming the absorption of nitrogen into ionic liquids is minimal, the vapor pressure of ILs are negligible, and due to the sufficiently low pressures, the fugacity coefficient corrections are essentially equal to one. Calculated $(f/P)_{sat,H2O}$ values can be found in Appendix A. These assumptions result in the simplified equation (Eq. 3.2):

$$x_1 \gamma_1 P_1^{sat} = P_1 \tag{3.2}$$

The activity coefficient can be calculated using the NRTL model as shown in Eq. 3.3, where τ_{12} and τ_{21} are the dimensionless interaction parameters.

$$P_1 = P_1^{sat} x_1 \exp\left(x_2^2 \left(\tau_{21} \left(\frac{G_{21}}{x_1 + x_2 G_{21}}\right)^2 + \frac{\tau_{12} G_{12}}{(x_2 + x_1 G_{12})^2}\right)\right) \tag{3.3}$$

This form can be further simplified using $G_{ij} = exp(-\alpha_{ij}\tau_{ij})$ and $x_2 = 1 - x_1$ giving the following equation:

$$P_1 = P_1^{sat} x_1 \exp\left((1-x_1)^2 \left(\tau_{21} \left(\frac{\exp(-\alpha_{21}\tau_{21})}{x_1 + (1-x_1)\exp(-\alpha_{21}\tau_{21})}\right)^2 + \frac{\tau_{12}\exp(-\alpha_{12}\tau_{12})}{(1-x_1+x_1\exp(-\alpha_{12}\tau_{12}))^2}\right)\right) \tag{3.4}$$

As typically done in literature,[49,50] τ_{12} and τ_{21} were modelled using two empirical parameters: $\tau_{12} = b_{12} + c_{12}/T$ and $\tau_{21} = b_{21} + c_{21}/T$. The α_{ij} term is called the non-randomness parameter, and it is often

set to be $\alpha = \alpha_{i\,j} = \alpha_{ji}$. The temperature independent parameters α, b_{ij}, and c_{ij} were determined by fitting the solubility data of all isotherms to Eq. 3.4, using a least squares difference method on the measured pressure and the pressure estimated by the model. The parameters are provided in Table 3.1 along with S, the standard error of regression. The standard error of regression, also known as RMSE (Root Mean Square Error), was calculated using Eq. 3.5, where $\hat{y}_i$ is the predicted pressure, y_i is the measured pressure, and n is the number of measurements.

$$S = \sqrt{\sum_{i=1}^{n} \frac{(\hat{y}_i - y_i)^2}{n}} \tag{3.5}$$

Table 3.1. Binary NRTL parameters of water vapor solubility in ionic liquids

Ionic Liquid	α	b_{12}	c_{12} (K)	b_{21}	c_{21} (K)	S (kPa)	n
$[C_2C_1im][BF_4]$	0.82	13.53	-3139.19	-0.86	271.61	0.04	149
$[C_2C_1im][TFES]$	0.08	55.86	5334.43	-2.20	528.53	0.02	31
$[C_2C_1im][OAc]$	0.12	-9.29	5303.02	-1.57	-2170.91	0.01	26
$[C_4C_1im][OAc]$	0.16	6.76	-122.00	-5.82	-388.00	0.05	39
$[C_4C_1im][Cl]$	0.32	7.05	-3009.51	-2.25	-201.01	< 0.01	33

The model correlations for $[C_2C_1im][TFES]$, $[C_2C_1im][OAc]$, $[C_4C_1im][OAc]$ and $[C_4C_1im][Cl]$ are shown in Figures 3.2 – 3.6. This study only measured two temperatures for the $[C_2C_1im][BF_4]$ system, therefore, the solubility data for water in $[C_2C_1im][BF_4]$ at temperatures of 283 K, 291 K, 298 K, and 303 K were obtained from Takamuku et al.[12] and correlated with the NRTL model. Overall, the NRTL model provides an excellent fit for all five systems as shown by the low standard errors of regression in Table 3.1. Considering that α is a measure of non-randomness, and α = 0 describes the ideal random system, it can be concluded that the most non-ideal system is $[C_2C_1im][BF_4]$ with α = 0.82. It was also attempted to fix the α value to 0.2 and 0.3 and to solve for the b_{ij} and c_{ij} parameters for the $[C_2C_1im][BF_4]$ system; however, the standard

errors of regression were not optimal (at 1.3 kPa). The nonrandom dispersion of water molecules in both $[C_2C_1im][BF_4]$[12] and $[C_4C_1im][BF_4]$[35] as described in the literature may provide some explanation for this non-ideal behavior. In addition, the similarity of the α values in $[C_2C_1im][OAc]$ ($\alpha = 0.12$) and $[C_4C_1im][OAc]$ ($\alpha = 0.16$) was expected due to the similarity of the ionic liquids. The low α value ($\alpha = 0.08$) of the water-$[C_2C_1im][TFES]$ system suggests the behavior of the mixture is close to an ideal random system; however, it is important to note that the fit analysis for the water-$[C_2C_1im][TFES]$ system is limited to the low water concentrations measured (x_w: 0 – 30 mol%) as a function of the RH range measured.

It is also valuable to discuss $\Delta g_{ij,}$ which is the difference in the energy interaction parameters between the water molecules and the ionic liquid molecules. These parameters can be determined using Eq. 3.6 and the τ_{ij} values (shown in Table 3.2) calculated by the b_{ij} and c_{ij} parameters.

$$\tau_{ij} = \frac{\Delta g_{ij}}{RT} = \frac{g_{ij} - g_{jj}}{RT} \tag{3.6}$$

Noting that g_{ij} values are negative because they represent attractive forces,[51] it is clear that the τ_{ij} values indicate the cation/anion interactions $|g_{22}|$ are stronger than the water/IL $|g_{12}|$ interactions for most water-IL systems, except for $[C_4C_1im][Cl]$ and to a less extent for $[C_2C_1im][BF_4]$. This suggests that water could be promoting ion dissociation of $[C_4C_1im][Cl]$[52] and $[C_2C_1im][BF_4]$[53]; an effect which has been described in literature. In addition, the observation of τ_{21} indicates that for $[C_2C_1im][OAc]$, $[C_4C_1im][OAc]$, and $[C_4C_1im][Cl]$ the water/IL interactions $|g_{21}|$ are stronger than the water/water interactions $|g_{11}|$. On the other hand, the water/IL interactions are slightly weaker than the water/water interactions in $[C_2C_1im][BF_4]$. This comparison suggests that substantial water-water bonding interactions exist in the $[C_2C_1im][BF_4]$ system which are energetically equal, if not stronger, than the bonding occurring between water

and the IL molecules. The τ_{21} values for $[C_2C_1im][TFES]$ are also close to zero ($\tau_{21} \sim -0.46$), and therefore suggest a similar behavior that hydrogen bonding between water molecules may be equivalent to the water-IL forces over the water concentration calculated (0 – 30 mol% H_2O).

Table 3.2. NRTL parameters τ_{ij} calculated for different temperatures of water absorption into $[C_2C_1im][BF_4]$, $[C_2C_1im][TFES]$, $[C_2C_1im][OAc]$, $[C_4C_1im][OAc]$, and $[C_4C_1im][Cl]$.

Ionic Liquid	T (K)	τ_{12}	τ_{21}
$[C_2C_1im][BF_4]$[a]	283	2.44	0.10
	291	2.74	0.07
	298	3.00	0.05
	303	3.17	0.04
$[C_2C_1im][TFES]$	283.15	74.06	-0.40
	303.15	73.46	-0.46
	313.15	72.90	-0.51
$[C_2C_1im][OAc]$	283.15	8.80	-8.97
	303.15	8.20	-8.73
	313.15	7.65	-8.50
$[C_4C_1im][OAc]$	294.85	6.34	-7.14
	303.15	6.35	-7.10
	315.15	6.37	-7.05
$[C_4C_1im][Cl]$	283.15	-3.58	-2.96
	295.15	-3.15	-2.93
	303.15	-2.88	-2.91

[a]The NRTL parameters were determined using experimental data from Takamuku et al. [12]

3.4 Conclusion

The solubility of water was measured in five ionic liquids ($[C_2C_1im][BF_4]$, $[C_2C_1im][TFES]$, $[C_2C_1im][OAc]$, $[C_4C_1im][OAc]$, and $[C_4C_1im][Cl]$) using an IGAsorp gravimetric microbalance over a range of temperature (293 K to 315 K) and relative humidity (0 % to 70 %). The solubility of water in $[C_2C_1im][BF_4]$ agreed with published data and provided confidence that the method was reliable for measuring water sorption in ionic liquids. The solubility of water was the highest in $[C_2C_1im][OAc]$ (78.4 mol%), followed by $[C_4C_1im][OAc]$

(77.5 mol%), [C_4C_1im][Cl] (68.6 mol%), [C_2C_1im][TFES] (26.5 mol%) and [C_2C_1im][BF_4] (19.5 mol%) at equivalent conditions (303.15 K and 25 % RH).

The activity coefficient NRTL model was successfully used to correlate the solubility data of the five IL systems. Temperature independent parameters were calculated using the solubility for each isotherm. Furthermore, energy interaction parameters (α, τ_{12}, and τ_{21}) provided further explanation for the solubility differences observed between [C_2C_1im][BF_4], [C_2C_1im][TFES], [C_2C_1im][OAc], [C_4C_1im][OAc], and [C_4C_1im][Cl].

Chapter 4: Diffusion and Enthalpy

4.1 Introduction

Time dependent concentration data were used to determine the binary diffusion coefficients of water in the five water-IL systems. One-dimensional and two-dimensional models were applied for the determination of diffusion coefficients. Differences between the water diffusion behavior in the ionic liquid systems are discussed by comparing the diffusing radius and heats of absorption for each system.

4.2 Diffusion

4.2.1 Model Selection

The mass absorption and desorption of water into the ionic liquids were measured as a function of time at each *T* and % RH using a spherical-shaped sample container shown in Figure 2.2a (Chapter 2). Due to the shape of the Pyrex® container, the ionic liquid volume was also a partial spherical shape (shown in Figure 4.1), where the water vapor present above the partial sphere enters the ionic liquid through the planar face. Water diffuses within the IL in radial (r) and polar (θ) directions, and the concentration of water is equal across the azimuthal (ϕ) coordinate and symmetrical at $\theta = 0$. The diffusion stops at the walls of the glass bulb where the flux boundary condition is equal to zero. To simplify the calculation of the diffusion coefficient, the following assumptions were made:

- no convective force is present,
- the temperature and pressure remain constant,
- and the ionic liquid-water system is a dilute solution where the thermophysical properties, such as density and viscosity, remain constant.

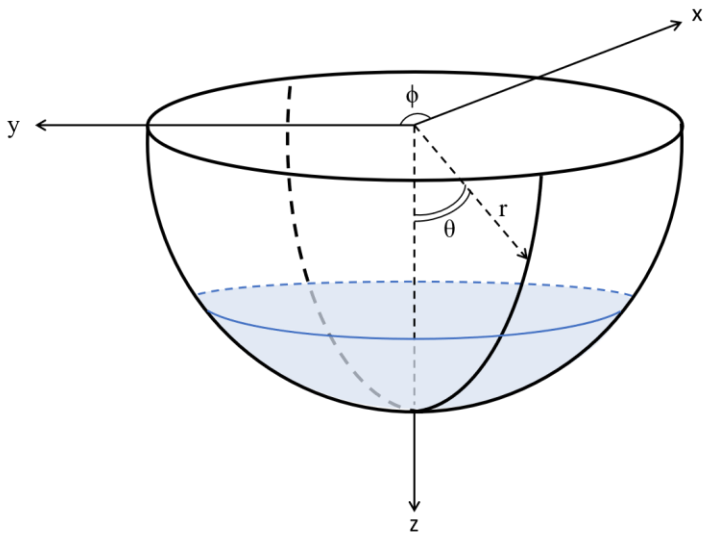

Figure 4.1. Partial spherical structure of the ionic liquid sample volume shown in the shaded region.

Yet, even with the assumptions in place, a derivation of the two-dimensional mass transfer occuring in a spherical-shaped system is quite complicated. Furtheremore, the *partial* spherical shape of the ionic liquid in the sample container complicates the coordinate description of the top boundary condition, where the concentration of water is assumed to instantly reach the saturation concentration. COMSOL Multiphysics® modeling software was used to simulate the diffusion of water into a partial sphere of ionic liquid using Fick's law of diffusion, where C is the concentration of water (mol/m^3), t is time (sec), and D is the diffusion coefficient (m^2/s) of water vapor in the ionic liquid:

$$\frac{\partial C}{\partial t} = D\nabla C \tag{4.1}$$

The geometry of the system in COMSOL was defined by creating half of a two-dimensional (2D) hemisphere with a radius equal to the radius of the Pyrex® container used, and removing a portion of the top section to achieve the height (Boundary 1 in Figure 4.2) equal to the height of the ionic liquid. This height was determined using Eq. 4.2, where the mass m (g) of IL,

density ρ (g/cm^3) of IL, and sphere radius r (cm) were known. The container radius and the mass of IL sample, sample container, and counterweight for each IL system are listed in Table 4.1.

Table 4.1. Size and mass of sample container and counterweight details for IL systems studied

Ionic Liquid	Radius of Spherical Container (cm)	Mass of IL (g)	Mass of Container (g)	Mass of Counterweight (g)
$[C_2C_1im][BF_4]$	0.6363	0.5635	0.2707	0.3808
$[C_2C_1im][TFES]$	0.5890	0.5275	0.2704	0.3769
$[C_2C_1im][OAc]$	0.6376	0.5141	0.2706	0.3768
$[C_4C_1im][OAc]$	0.6363	0.5664	0.2707	0.3808
$[C_4C_1im][Cl]$	0.6363	0.6305	0.2707	0.3808

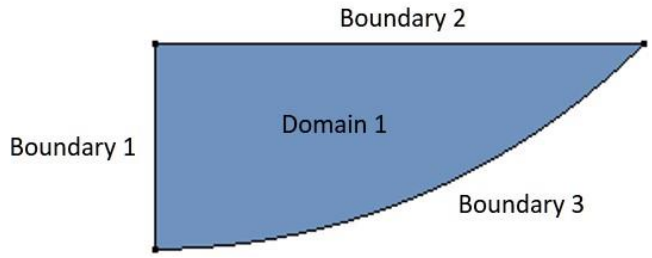

Figure 4.2. COMSOL 2D geometry with the domain and boundaries of interest

$$\frac{m}{\rho} = \frac{1}{3}\pi h^2(3r - h) \tag{4.2}$$

The COMSOL Multiphysics® software describes the entire geometry of the liquid by revolving the 2D shape in Figure 4.2 around the line r = 0 (Boundary 1), thus creating a three-dimensional (3D) shape. The initial concentration (Eq. 4.3) was applied by setting an initial value condition to Domain 1. The saturation assumption (Eq. 4.4) was set to Boundary 2 with a concentration condition equal to C_s. The symmetry assumption (Eq. 4.5) was applied using the "Axial Symmetry" condition for Boundary 1. Finally, the no flux boundary condition (Eq. 4.6) was set on Boundary 3.

$$C = C_0 \text{ throughout the IL when } t = 0 \tag{4.3}$$

$$C = C_s \text{ at the top boundary when } t > 0 \tag{4.4}$$

$$\frac{\partial C}{\partial \theta} = 0 \text{ at } \theta = 0 \tag{4.5}$$

$$\frac{\partial C}{\partial r} = 0 \text{ at } r = R \tag{4.6}$$

Three methods were considered in the COMSOL Multiphysics® analysis where the objective was to minimize the sum of squared differences between the simulation measurement and the experimental data (mass vs. time). The experimental mass versus time data is the average water concentration (i.e., mass fraction) in the sample at a given time. The output of the COMSOL Multiphysics® Simulation is reported in moles of H_2O per liquid volume (n_{H2O}/V) as a function of position and time. Therefore, the output n_{H2O}/V was integrated over the 3D geometry to obtain total moles of H_2O (n_{H2O}) and divided by the total mass to obtain composition, as shown in Eqs. 4.7 and 4.8.

$$n_{H2O} = \iiint \frac{n_{H2O}}{V} dV \tag{4.7}$$

$$C = \frac{n_{H2O} * MW_{H2O}}{n_{H2O} MW_{H2O} + (1 - n_{H2O}) * MW_{IL}} \tag{4.8}$$

The first diffusion coefficient calculation method was applied to the time-dependent solubility data for the H_2O-[C_4C_1im][OAc] system at 294.85 K and 15.67 % RH, where a value for C_0 was specified and D and C_s variables were solved. The specified value for C_0 (15.28 wt. %) was based on the water concentration measured in the ionic liquid at the instant when the RH becomes stable. A comparison between the simulation (lines) and the experimental data (circles), shown in Figure 4.3a, indicates that the fit is reasonable but could be improved. The second method applied included C_0 as a parameter to be optimized along with D and C_s. This method provides a better fit, as shown in Figure 4.3a but could also be improved if the first few data points were deleted. Therefore, the third COMSOL optimization trial was performed deleting the first 3

measured points and solving for D, C_s, and C_o. The optimized parameters D, C_s, C_o, and standard errors of regression (S) for each method are shown in Table 4.2, and the methods are listed below:

- Method 1: C_0 value was specified, D and C_s were calculated using all data points.
- Method 2: D, C_s, and C_0 were calculated using all data points.
- Method 3: D, C_s, and C_0 were calculated using all data except for the first 3 points.

It was also desired to observe if the 1D diffusion approximation previously used by Minnick et al.[25] could be successfully used to predict the diffusion in this hemispherical system. The 1D diffusion approximation is shown in Eq. 4.9, which describes the average concentration of water ($<C>$) as a function of time for an ionic liquid system with height L in a cylindrical container, where $\lambda_n=(n+1/2)\pi/L$. In this case, water vapor enters the liquid system through the top flat face and travels downward in the z-direction. It is important to note that L in Eq. 4.9 is not equal to h in Eq. 4.2. The radius of the cylinder was assumed to be equal to the partial radius r_p (i.e., the length of Boundary 2 in Figure 4.2) calculated in Eq. 4.10, and the height (L) of the theoretical cylinder was calculated using Eq. 4.11, where the mass of IL m (g), the IL density ρ (g/cm^3), and sphere radius r (cm) were known.

$$< C >= C_s \left[1 - 2\left(1 - \frac{C_0}{C_s}\right)\sum_{n=0}^{\infty}\frac{\exp(-\lambda_n^2 Dt)}{L^2\lambda_n^2}\right] \tag{4.9}$$

$$r_p = \sqrt{h(2r-h)} \tag{4.10}$$

$$L = \frac{m}{\rho\pi r_p^2} \tag{4.11}$$

One-hundred and fifty summations were used in Eq. 4.9 because additional terms had an impact less than 1 x 10^{-14} (m^2/s) on the D coefficient and less than 1 x 10^{-4} (mass fraction) on the C_s and C_0 values. The 1D approximation, Eq. 4.9, was applied to the time-dependent solubility data of the H_2O-[C_4C_1im][OAc] system at 294.85 K and 15.67 % RH using the same three methods

used previously. The different fits obtained by the 1D diffusion equation are shown in Figure 4.3b and Table 4.2 provides the values for *D*, C_s, C_0, and standard errors of regression.

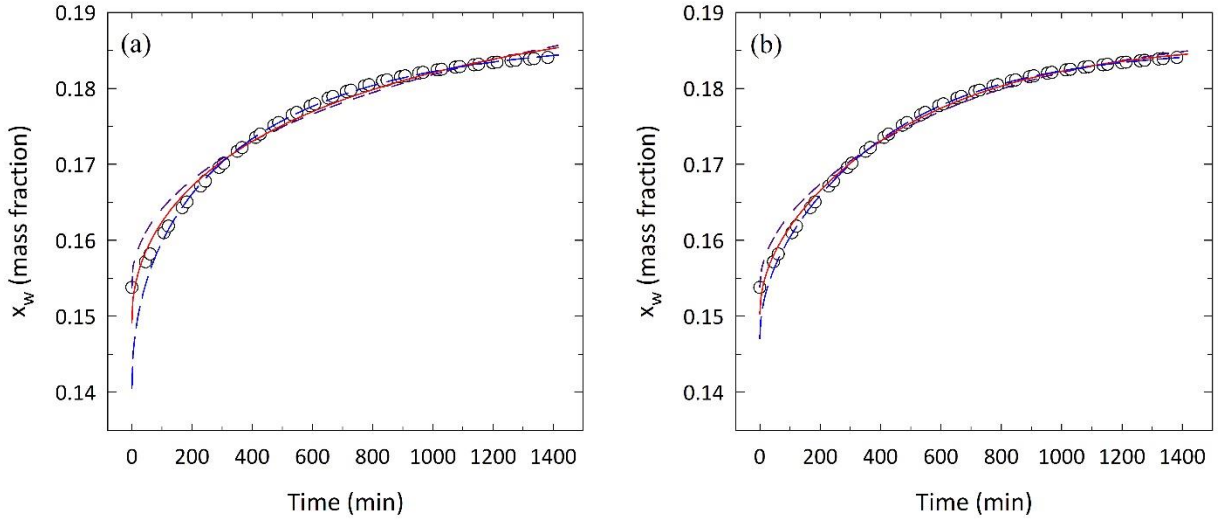

Figure 4.3. Diffusion model comparison between (a) the COMSOL 2D mass transfer simulation and (b) the 1D diffusion Eq. 4.9 to determine the binary D coefficient for water in ILs by fitting the mass fraction per time data. Open circle symbols are experimental data. Purple short-dashed line represents the fit where C_0 value was specified, D and C_s were calculated using all data points; red solid line represents the fit where D, C_s, and C_0 were calculated using all data points; blue long-dashed line represents the fit where D, C_s, and C_0 were calculated using all data points except for the first 3 measured points.

Table 4.2. Values D, C_s, and C_0 determined by the 2D COMSOL simulation and the 1D diffusion equation (Eq. 4.9) for the solubility of water in $[C_4C_1im][OAc]$ at 15 % RH and 294.85 K

Approach	Method	D (x 10^{-11} m^2/s)	C_s, meas (wt. %)	C_s, calc (wt. %)	C_0, meas (wt. %)	C_0, calc (wt. %)	S (wt. %)
2D	1	0.5	18.6	20.3	15.4	15.4	0.2
COMSOL	2	1.1	18.6	19.2	15.4	14.9	0.1
Simulation	3	2.2	18.6	18.6	15.4	14.1	0.2
1D	1	0.8	18.6	18.8	15.4	15.4	0.1
Equation	2	1.1	18.6	18.6	15.4	15.0	0.1
(Eq. 4.9)	3	1.3	18.6	18.5	15.4	14.7	0.1

The 47 data points were fitted.

Method 1, with a specified value for C_0, was not optimum for either the 2D or 1D models, and Method 3 eliminated the first three data points which was not preferred. Finally, comparing the results for Method 2 predicted by COMSOL Multiphysics® and the 1D diffusion model shows that the parameters are not significantly different, as shown in Figure 4.3 and Table 4.2. However,

the 1D model predicts a C_s value closer to the measured water solubility; therefore, the 1D model was used for the remainder of this study. The measured and calculated solubility of water in the five ionic liquid systems using the 1D diffusion model are shown in Tables 4.3-4.7.

4.2.2 Diffusion Results

Table 4.3. Diffusivity data for absorption and desorption of water in $[C_2C_1im][BF_4]$ determined using the 1D diffusion equation[a]

T[b] (K)	Sorption	RH[b] (%)	D[c] (x 10^{-11} m^2/s)	$C_{s,\ meas}$[b] (mol%)	$C_{s,\ calc}$[c] (mol%)	$C_{0,\ meas}$[b] (mol%)	$C_{0,\ calc}$[c] (mol%)	S[d] (mol%)	n[d]
298.15	Abs.	10.67	9.6	8.4	8.5	2.7	2.7	0.1	1092
	Abs.	50.67	5.3	40.4	40.4	25.8	25.8	0.2	2261
	Des.	50.67	3.6	40.4	39.5	59.7	62.4	1.3	1016
	Abs.	70.67	2.6	59.4	59.2	41.9	39.2	0.4	4262
303.15	Abs.	10.67	13	9.2	9.2	2.7	2.7	0.1	966
	Abs.	50.67	6.9	41.9	41.8	27.3	24.9	0.2	1830
	Des.	50.67	4.4	41.7	40.7	62.8	65.6	1.6	994
	Abs.	70.67	2.7	60.6	60.5	51.0	49.6	0.3	4919

[a] Complete solubility data (including absorption and desorption) can be found in Appendix A.
[b] The instrumental uncertainties are: T = ± 0.01 K; % RH = ± 1 %; C_s and C_0 < ± 0.1 mol%. See Appendix A for more details.
[c] The average uncertainties determined by the error of regression are: D = ± 0.1 x 10^{-11} m^2/s; C_s = ± 0.1 mol%; C_0 = ± 0.1 mol%.
[d] S is the standard error of regression for the 1D diffusion equation. n is the number of data points fitted.

Table 4.4. Diffusivity data for absorption and desorption of water in [C_2C_1im][TFES] determined using the 1D diffusion equation[a]

T[b] (K)	Sorption	RH[b] (%)	D[c] (x 10^{-11} m^2/s)	$C_{s,\ meas}$[b] (mol%)	$C_{s,\ calc}$[c] (mol%)	$C_{0,\ meas}$[b] (mol%)	$C_{0,\ calc}$[c] (mol%)	S[d] (mol%)	n[d]
293.15	Abs.	5.00	4.4	6.06	6.08	2.40	1.88	0.03	2298
	Abs.	15.00	4.5	16.18	16.19	11.86	11.30	0.04	2323
	Des.	15.00	5.2	16.22	16.16	24.78	25.97	0.13	981
	Abs.	25.00	4.2	25.65	25.69	21.38	20.78	0.05	2345
303.15	Abs.	5.00	7.3	6.39	6.40	2.75	2.27	0.03	2094
	Abs.	15.00	7.4	16.84	16.85	13.01	12.47	0.04	2128
	Des.	15.00	8.8	16.78	16.76	24.90	26.06	0.11	975
	Abs.	25.00	7.4	26.45	26.46	22.16	21.58	0.04	2118
313.15	Abs.	5.00	11	6.55	6.56	3.03	2.55	0.03	2276
	Abs.	15.00	11	17.23	17.22	13.24	12.7	0.03	2099
	Des.	15.00	14	17.15	17.15	25.46	26.64	0.09	1689
	Abs.	25.00	12	26.90	26.90	22.89	22.33	0.04	2276

[a] Complete solubility data (including absorption and desorption) can be found in the Appendix A.
[b] The instrumental uncertainties are: T = ± 0.01 K; % RH = ± 1 %; C_s and C_0 < ± 0.1 mol%. See Appendix A for more details.
[c] The average uncertainties determined by the error of regression are: D = ± 0.1 x 10^{-11} m^2/s; C_s = ± 0.1 mol%; C_0 = ± 0.1 mol%.
[d] S is the standard error of regression for the 1D diffusion equation. n is the number of data points fitted.

Table 4.5. Diffusivity data for absorption and desorption of water in [C_2C_1im][OAc] determined using the 1D diffusion equation[a]

T[b] (K)	Sorption	RH[b] (%)	D[c] (x 10^{-11} m^2/s)	$C_{s,\ meas}$[b] (mol%)	$C_{s,\ calc}$[c] (mol%)	$C_{0,\ meas}$[b] (mol%)	$C_{0,\ calc}$[c] (mol%)	S[d] (mol%)	n[d]
293.15	Abs.	5.00	0.46	61.5	61.7	48.2	45.3	0.7	998
	Abs.	15.00	0.73	73.3	73.3	68.8	68.0	0.4	984
	Des.	15.00	0.73	73.3	73.1	78.8	79.6	0.7	1002
	Abs.	25.00	0.78	79.0	79.1	76.5	76.1	0.3	999
303.15	Abs.	5.00	0.99	60.2	60.2	52.6	51.2	0.4	1002
	Abs.	15.00	1.5	72.5	72.6	68.1	67.3	0.3	1003
	Des.	15.00	1.5	72.1	72.1	77.9	78.8	0.3	995
	Abs.	25.00	1.6	78.4	78.4	75.9	75.5	0.3	1005
313.15	Abs.	5.00	1.8	59.0	59.0	51.3	49.8	0.3	1008
	Abs.	15.00	2.7	71.7	71.7	67.2	66.4	0.6	986
	Des.	15.00	2.7	71.6	71.5	77.5	78.4	0.4	1010
	Abs.	25.00	2.8	77.7	77.7	75.2	74.7	0.3	991

[a] Complete solubility data (including absorption and desorption) can be found in the Appendix A.
[b] The instrumental uncertainties are: T = ± 0.01 K; % RH = ± 1 %; C_s and C_0 < ± 0.1 mol%. See Appendix A for more details.
[c] The average uncertainties determined by the error of regression are: D = ± 0.1 x 10^{-11} m^2/s; C_s = ± 0.1 mol%; C_0 = ± 0.1 mol%.
[d] S is the standard error of regression for the 1D diffusion equation. n is the number of data points fitted.

Table 4.6. Diffusivity data for absorption and desorption of water in [C_4C_1im][OAc] determined using the 1D diffusion equation[a]

T[b] (K)	Sorption	RH[b] (%)	D[c] (x 10^{-11} m^2/s)	$C_{s,\ meas}$[b] (mol%)	$C_{s,\ calc}$[c] (mol%)	$C_{0,\ meas}$[b] (mol%)	$C_{0,\ calc}$[c] (mol%)	S[d] (mol%)	n[d]
294.85	Abs.	5.67	0.88	59.4	59.4	38.6	33.0	0.8	3399
	Abs.	15.67	1.1	71.6	71.6	66.7	66.1	0.7	46
	Des.	15.67	1.2	71.6	71.6	74.9	75.4	0.3	997
	Abs.	25.67	1.3	77.8	77.8	75.2	74.7	0.8	3477
303.15	Abs.	5.67	1.5	60.9	61.0	45.0	41.6	0.7	422
	Abs.	15.67	2.1	71.8	71.9	64.5	63.1	0.6	361
	Des.	15.67	1.9	72.1	72.0	72.1	76.3	0.6	1241
	Abs.	25.67	2.1	78.1	78.0	74.1	73.4	0.4	421
315.15	Abs.	5.67	3.6	59.2	59.1	41.4	37.3	0.6	1640
	Abs.	15.67	3.8	71.2	71.2	66.6	65.9	0.4	541
	Des.	15.67	4.0	71.2	71.1	74.5	75.0	0.3	999
	Abs.	25.67	3.9	77.4	77.4	74.7	74.3	0.3	611

[a] Complete solubility data (including absorption and desorption) can be found in the Appendix A.
[b] The instrumental uncertainties are: T = ± 0.01 K; % RH = ± 1 %; C_s and C_0 < ± 0.1 mol%. See Appendix A for more details.
[c] The average uncertainties determined by the error of regression are: D = ± 0.1 x 10^{-11} m^2/s; C_s = ± 0.1 mol%; C_0 = ± 0.1 mol%.
[d] S is the standard error of regression for the 1D diffusion equation. n is the number of data points fitted.

Table 4.7. Diffusivity Data for absorption and desorption of Water in [C_4C_1im][Cl] determined using the 1D diffusion equation[a]

T[b] (K)	Sorption	RH[b] (%)	D[c] (x 10^{-11} m^2/s)	$C_{s,\ meas}$[b] (mol%)	$C_{s,\ calc}$[c] (mol%)	$C_{0,\ meas}$[b] (mol%)	$C_{0,\ calc}$[c] (mol%)	S[d] (mol%)	n[d]
283.15	Abs.	5.67	0.45	50.6	50.8	37.9	35.4	0.4	1038
	Abs.	15.67	0.67	63.1	58.0	57.3	0.3	0.67	1961
	Abs.	25.67	0.76	70.1	70.1	66.8	66.2	0.2	1429
295.15	Abs.	5.67	0.95	49.6	49.9	38.0	36.2	0.3	1597
	Abs.	15.67	1.7	61.9	62.0	57.2	56.4	0.2	1838
	Des.	15.67	1.7	61.9	61.9	69.0	69.9	0.4	994
	Abs.	25.67	1.7	69.3	69.3	66.1	65.5	0.2	1900
303.15	Abs.	5.67	1.7	49.1	49.0	37.2	35.3	0.3	1544
	Abs.	15.67	2.7	61.7	61.7	56.7	56.0	0.2	1190
	Des.	15.67	2.9	61.6	61.6	68.8	69.7	0.4	993
	Abs.	25.67	2.8	69.0	69.1	65.8	65.3	0.2	1111

[a] Complete solubility data (including absorption and desorption) can be found in the Appendix A.
[b] The instrumental uncertainties are: T = ± 0.01 K; % RH = ± 1 %; C_s and C_0 < ± 0.1 mol%. See Appendix A for more details.
[c] The average uncertainties determined by the error of regression are: D = ± 0.1 x 10^{-11} m^2/s; C_s = ± 0.1 mol%; C_0 = ± 0.1 mol%.
[d] S is the standard error of regression for the 1D diffusion equation. n is the number of data points fitted.

4.2.3 1D Diffusion with Cylindrical Container

The accuracy of the 1D diffusion model applied to water solubility data measured with a spherical-shaped container was verified by repeating the water solubility measurements and 1D diffusion calculation in $[C_2C_1im][OAc]$ using a flat bottom cylindrical container, shown in Figure 4.4. The amount of IL used was ~ 0.92 g, the weight of the sample cup and counterweight were 0.568 g and 0.669 mg, respectively, and the radius of the container was 0.62 cm. The height of the liquid (L) was obtained using Eq. 4.11 and the measured cylinder radius. The solubility measurements were carried out at 303.15 K and a range of 0-25 % RH. A comparison of the results obtained using the spherical-shaped container and the cylindrical container are shown in Table 4.8. The results are not significantly different; therefore, the use of the 1D diffusion model is applicable to data obtained using a spherical-shaped container.

Figure 4.4. Cylindrical container used for verification of the 1D diffusion approximation

Table 4.8. Diffusion coefficient comparisons for absorption of water in $[C_2C_1im][OAc]$ at 303.15 K using a spherical-shaped container and using a cylindrical-shaped container with the 1D diffusion equation (Eq. 4.9).

RH (%)	$D_{Spherical\ cup}$ (x 10^{-11} m^2/s)	$D_{Cylindrical\ Cup}$ (x 10^{-11} m^2/s)
5	0.99 ± 0.01	1.1 ± 0.1
10	1.5 ±0.1	1.9 ± 0.1
15	1.6 ± 0.1	2.0 ± 0.1

4.2.4 Height Effect on the Diffusion Coefficient

It is important to note that the diffusion coefficients calculated in this work and reported in Tables 4.3-4.7 are approximations, as the diffusion coefficient calculations assumed that the system was dilute. The concentration of water increases as RH increases; therefore, the physical properties of the system are not constant. Due to volume expansion, the height of the sample through which the water molecules must travel increases with increasing RH. Therefore, the diffusion coefficient of each IL was recalculated at the highest RH measured for each temperature using the average "wet" height instead of the "dry" height to observe the effect of height (L) on the diffusion coefficient. The "wet" height was calculated by taking the average of the height from beginning to end at a specified T and RH condition. For example, for $[C_4C_1im][OAc]$ at 294.85 K and 25.67 % RH, x_w was 77.8 mol% and the calculated molar volume was 0.0692 cm^3, and at 294.85 K and 20.67 % RH, x_w was 75.2 mol% and the molar volume was 0.0718 cm^3; the average volume is 0.0705 cm^3. Using Eqs. 4.10 and 4.11, the average cylinder height was calculated to be 0.1054 cm. The dry height was calculated assuming the IL is completely dry, which for $[C_4C_1im][OAc]$ at 294.85 K is 0.0904 cm.

The diffusion coefficients, the average "wet" height values, and the "dry" height values are listed in Table 4.9. On average the diffusion coefficient increased by 26 % when using the average height including volume expansion versus the initial height without volume expansion. The diffusion coefficients at the highest RH values were about 15 % higher for $[C_2C_1im][BF_4]$, 3 % higher for $[C_2C_1im][TFES]$, 48 % higher for $[C_2C_1im][OAc]$, 33 % higher for $[C_4C_1im][OAc]$, and 25 % higher for $[C_4C_1im][Cl]$, when using the average "wet" height, than when using the "dry" height in Eq. 4.9.

Table 4.9. Effect of Height on the Diffusion Coefficient

Ionic Liquid	Temperature (K)	RH (%)	Dry Cylindrical Height (cm)	$D_{Dry\ Height}$ (x 10^{-11} m^2/s)	Average "wet" Cylindrical Height (cm)	$D_{Avg\ Wet\ Height}$ (x 10^{-11} m^2/s)
$[C_2C_1im][BF_4]$	298.15	70.67	0.0810	2.6	0.0864	2.9
	303.15	70.67	0.0811	2.7	0.0876	3.2
$[C_2C_1im][TFES]$	293.15	25.00	0.0771	4.2	0.0783	4.4
	303.15	25.00	0.0773	7.4	0.0785	7.6
	313.15	25.00	0.0776	12	0.0776	12
$[C_2C_1im][OAc]$	293.15	25.00	0.0837	0.78	0.1013	1.2
	303.15	25.00	0.0837	1.6	0.1007	2.3
	313.15	25.00	0.0838	2.8	0.1001	4.1
$[C_4C_1im][OAc]$	294.85	25.67	0.0904	1.3	0.1054	1.7
	303.15	25.67	0.0907	2.1	0.1059	2.8
	315.15	25.67	0.0909	3.9	0.1056	5.2
$[C_4C_1im][Cl]$	283.15	25.66	0.0948	0.8	0.1072	1.0
	295.15	25.67	0.0934	1.7	0.1052	2.1
	303.15	25.66	0.0953	2.8	0.1072	3.5

As expected, the reported diffusion coefficients for $[C_2C_1im][BF_4]$, $[C_2C_1im][TFES]$, $[C_2C_1im][OAc]$, $[C_4C_1im][OAc]$, and $[C_4C_1im][Cl]$ increase with an increase in temperature. For example, the water absorption in $[C_2C_1im][BF_4]$ at 10 % RH and 298 K had D = (9.6 - 9.7) x 10^{-11} m^2/s, while at 10 % RH and 303 K, D = 1.3 x 10^{-10} m^2/s. The 35% increase in the diffusion coefficient is due to the decrease in viscosity of the ionic liquid (0.0372 ± 0.00324 Pa-s at 298.15 K and 0.0314 ± 0.0021 Pa-s at 303.15 K)[54] which leads to faster water diffusion into the ionic liquid.

Also as expected, the viscosity of $[C_2C_1im][BF_4]$, $[C_2C_1im][OAc]$, $[C_4C_1im][OAc]$, and $[C_4C_1im][Cl]$ decreases as the water concentration increases.[54–56] Although there are no data reporting the mixture viscosity of water and $[C_2C_1im][TFES]$, it is predicted that the viscosity of the mixture would decrease as water concentration increases because water has a lower viscosity (0.001 Pa-s at 293.15 K) than the viscosity of pure $[C_2C_1im][TFES]$ (0.117 Pa-s at 293.15 K). Therefore, diffusivity is expected to increase in ILs as relative humidity increases, and this was

observed for [C_2C_1im][TFES], [C_2C_1im][OAc], [C_4C_1im][OAc], and [C_4C_1im][Cl]. Surprisingly, despite a decrease in viscosity as relative humidity increases, the H_2O-[C_2C_1im][BF_4] system shows a decrease in diffusion *D*.

The desorption diffusion coefficients for [C_2C_1im][TFES], [C_2C_1im][OAc], [C_4C_1im][OAc], and [C_4C_1im][Cl] were not significantly different from the absorption diffusion coefficients, but in general, the desorption *D* values were slightly higher, especially in the water-[C_2C_1im][TFES] system. This is expected because the diffusion during the desorption process begins with a higher water concentration; and, therefore, the viscosity is lower than the corresponding absorption process at the same *T* and *P* conditions. However, in the case of [C_2C_1im][BF_4] the desorption coefficients were lower than the absorption coefficients; for example, at 298.15 K and 50.67 % RH (including the liquid height effect on *D*): $D_{desorption}$= (3.6 – 4.1) x 10^{-11} m^2/s vs. $D_{absorption}$= (5.3 – 5.6) x 10^{-11} m^2/s. This again illustrates the unexpected influence the presence of water has on the diffusion coefficient in [C_2C_1im][BF_4].

4.2.5 Einstein-Stokes Estimation of Diffusing Radius

A comparison of the diffusing radii in the water-IL systems was applied to further analyze the difference in diffusion coefficients of such systems. The Einstein-Stokes equation provides the relationship of a spherical solute (A) with radius r_A diffusing through a solution B with viscosity η_B, as shown in Eq. 4.12, where *k* is the Boltzmann constant.

$$D = \frac{kT}{6\pi r_A \eta_B} \tag{4.12}$$

This equation was modified empirically by Shiflett and Yokozeki[50] to introduce the dependence of diffusion on the mixture density raised to a power *b* (i.e., $D \propto \eta^{-b}$), and it is shown in Eq. 4.13, where a normalization factor was included (η_0 = 1 mPa-s) and $a = ln(k/6\pi r\eta_0)$.

$$\ln(D/T) = a - b\ln(\eta/\eta_0) \tag{4.13}$$

The diffusion data for the water-IL systems were fit to Eq. 4.13 as a function of T and x_w using mixture viscosity data determined from literature. The parameters a and b were calculated by minimizing the error between the measured and calculated D values, and the diffusing radius r was calculated from coefficient a. The results are listed in Table 4.10. Due to the lack of viscosity data for mixtures of $[C_2C_1im][TFES]$ and water, the diffusivity radius was not calculated.

Table 4.10. Parameters determined in Eq. 4.13

Ionic Liquid	a	b	Diffusing Radius r (nm)
$[C_2C_1im][BF_4]$	-31.205 ± 0.509	-0.755 ± 0.198	15.694 – 43.436
$[C_2C_1im][OAc]$	-27.701 ± 0.630	0.973 ± 0.201	0.418 – 1.475
$[C_4C_1im][OAc]$	-27.796 ± 0.682	0.714 ± 0.184	0.437 – 1.709
$[C_4C_1im][Cl]$	-28.543 ± 0.562	0.441 ± 0.131	1.040 – 3.200

The viscosity values for $[C_2C_1im][BF_4]$,[54] $[C_2C_1im][OAc]$,[55] $[C_4C_1im][OAc]$,[55] and $[C_4C_1im][Cl]$[56] were determined from literature. Errors are determined from linear regression of $\ln(D/T)$ vs. $\ln(\eta/\eta_0)$.

The resulting diffusing radius for the water-$[C_2C_1im][OAc]$, water-$[C_4C_1im][OAc]$, and water-$[C_4C_1im][Cl]$ systems were ~ 1 nm, and the diffusing radius for the water-$[C_2C_1im][BF_4]$ system was ~ 30 nm. The radii of water, $[OAc]^-$, $[Cl]^-$, and $[BF_4]^-$ are 0.14 nm,[57] 0.16 nm,[58] 0.18 nm,[59] and 0.22 nm,[60] respectively. This leads to a hypothesis that the anions in $[C_2C_1im][OAc]$, $[C_4C_1im][OAc]$, and $[C_4C_1im][Cl]$ may coordinate with a few water molecules through hydrogen bonding, and that much larger water/BF_4^- networks may be occurring in the $[C_2C_1im][BF_4]$ system, where water-water hydrogen bonds form and aggregate with or around BF_4 ions. Several studies agree on the possibility of water aggregates and ionic cluster formations in aqueous IL mixtures.[16,18,61–63] Therefore, although viscosity of the water-IL systems decreased as water concentration increased, the size of the diffusing species in $[C_2C_1im][BF_4]$ is expected to increase

whereas the diffusing radii in the [C_2C_1im][OAc], [C_4C_1im][OAc], and [C_4C_1im][Cl] are expected to remain constant.

4.3 Heats of Absorption

A comparison between the heat of absorption of water in the water-ionic liquid systems and the heat of vaporization of water can provide insight into the interaction behavior.[12] The heats of absorption for all three systems were calculated with the Clausius-Clapeyron Relation shown in Eq. 4.14, where R is the ideal gas constant, T is temperature, H is enthalpy and C is the indefinite integral constant. The pressure values used in Eq 4.14 were determined using the NRTL correlation at the temperatures and water concentrations measured. The heats of absorption (ΔH) were calculated from the slope ($-\Delta H/R$) of $ln(P)$ as a function of $1/T$ at constant composition. The enthalpies of absorption calculated by Takamuku et al.[12] were recalculated in this work using their data and the NRTL model parameters determined in the present study.

$$\ln(P) = \frac{-\Delta H}{RT} + C \tag{4.14}$$

The heats of water absorption as a function of x_w in [C_2C_1im][BF_4], [C_2C_1im][TFES], [C_2C_1im][OAc], [C_4C_1im][OAc], and [C_4C_1im][Cl] are compared to the enthalpy of vaporization for water (ΔH_{vap}) at 298.15 K (44 kJ/mol)[64] in Figure 4.5. The IL-water interactions (i.e., heats of absorption) in the [C_2C_1im][BF_4] and [C_2C_1im][TFES] systems are weaker at lower concentrations of water (x_w) as shown in Figure 4.5a and b. However, as the water concentration increases, the interactions with water increase and approach that of pure water-water interactions which are governed by hydrogen bonding. On the contrary, at low concentrations of water in [C_2C_1im][OAc], [C_4C_1im][OAc], and [C_4C_1im][Cl] (Figure 4.5c, d, and e, respectively), the heats of absorption are larger than the ΔH_{vap} of water, and as the water concentration increases, the interactions decrease and approach that of pure water-water interactions.

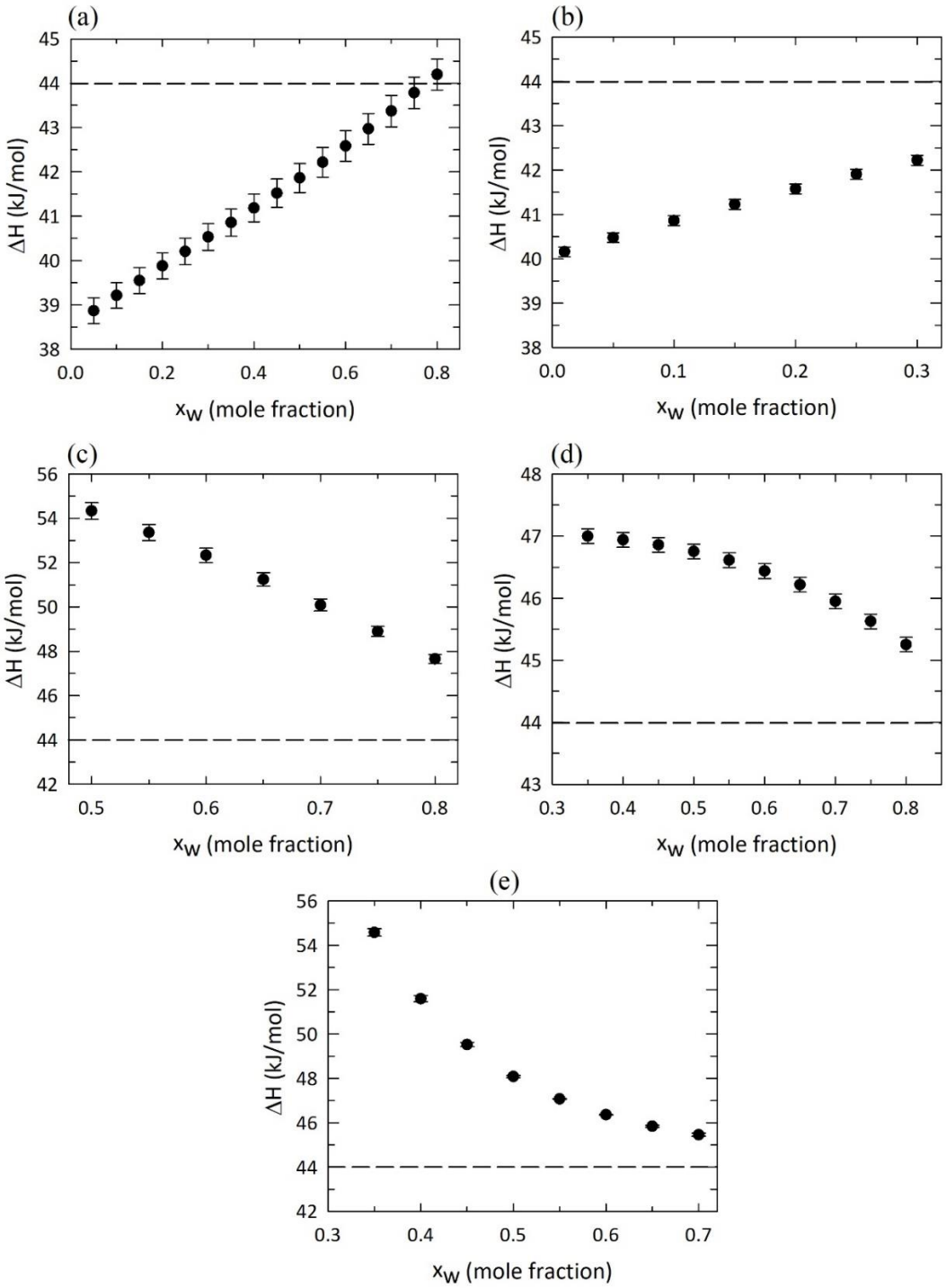

Figure 4.5. Enthalpy of absorption for water in (a) $[C_2C_1im][BF_4]$, (b) $[C_2C_1im][TFES]$, (c) $[C_2C_1im][OAc]$, (d) $[C_4C_1im][OAc]$, and (e) $[C_4C_1im][Cl]$. The standard errors are shown in vertical error bars. The dashed line represents the enthalpy of vaporization of water at 298 K. Tabulated data can be found in Appendix A

The effects of the water-IL interactions on the diffusion coefficients are clearly observed when comparing the three systems at similar viscosities and temperatures as shown in Table 4.11.

The ΔH_{abs} of water and viscosity in [C_4C_1im][OAc] (45.4 ± 0.1 kJ/mol, 0.024 Pa-s, x_w = 78.1 mol%) and [C_4C_1im][Cl] (45.5 ± 0.1 kJ/mol, 0.028 Pa-s, x_w = 69.0 mol%) at 303.15 K were essentially the same; therefore, the absorption diffusion coefficients were similar ($D_{[C4C1im][OAc]}$ = (2.1 – 2.8) x 10^{-11} m^2/s and $D_{[C4C1im][Cl]}$ = (2.8 – 3.5) x 10^{-11} m^2/s). At the same conditions, (0.021 Pa-s and 303.15 K), the water-[C_2C_1im][OAc] system (at x_w= 72.5 mol%) had a higher ΔH_{abs} of water (48.1 ± 0.3 kJ/mol) and a lower diffusion coefficient ((1.3 – 1.7) x 10^{-11} m^2/s). At 0.025 Pa-s and 303.15 K, the H_2O-[C_2C_1im][BF_4] system (at x_w = 9.23 mol%) had a lower ΔH_{abs} of water (39.3 ± 0.1 kJ/mol), and a significantly higher absorption diffusion (1.3 x 10^{-10} m^2/s). The same effect is observed at 294.85 – 298.15 K and 0.030 – 0.041 Pa-s, as shown in Table 4.11. The results for the four water-IL systems indicate that at about equal viscosities and temperatures, the diffusion coefficients are higher for lower values of ΔH_{abs} and lower for higher values of $\Delta H_{abs.}$ Therefore, the measurements show that even though the viscosity of all three IL-water systems decreases as water concentration increases, the diffusion coefficients are also a function of the molecular (water-water and water-IL) interactions (i.e., ΔH_{abs}).

Table 4.11. Comparison of diffusion coefficients and ΔH_{abs} of water in [C_2C_1im][BF_4], [C_4C_1im][OAc], and [C_4C_1im][Cl] as a function of temperature and viscosity

Ionic Liquid	T[a] (K)	x_w[a] (mole %)	μ[b] (Pa-s)	D[c] (m^2/s)	ΔH_{abs} (kJ/mol)
[C_2C_1im][BF_4]	298.15	8.5	0.030	(9.6 – 9.7) x 10^{-11}	39.2 ± 0.1
	303.15	9.2	0.025	1.3 x 10^{-10}	39.4 ± 0.1
[C_2C_1im][OAc]	293.15	73.3	0.031	(0.73 – 1.0) x 10^{-11}	49.3 ± 0.3
	303.15	72.5	0.021	(1.5 – 2.0) x 10^{-11}	48.1 ± 0.3
[C_4C_1im][OAc]	294.85	77.8	0.039	(1.3 – 1.7) x 10^{-11}	45.4 ± 0.1
	303.15	78.1	0.024	(2.1 – 2.8) x 10^{-11}	45.4 ± 0.1
[C_4C_1im][Cl]	295.15	69.3	0.040	(1.7 – 2.1) x 10^{-11}	45.5 ± 0.1
	303.15	69.0	0.028	(2.8 – 3.5) x 10^{-11}	45.5 ± 0.1

[a] The uncertainties are: T ± 0.01 K and x_w < 0.1 mol% .
[b] The viscosity values for [C_2C_1im][BF_4],[54] [C_2C_1im][OAc],[55] [C_4C_1im][OAc],[55] and [C_4C_1im][Cl][56] were determined from literature.
[c] The diffusion values presented show a range of the diffusion coefficients obtained with the dry and "wet" height.

These interactions in the $[C_2C_1im][BF_4]$ system are weaker than the water-water interactions (i.e., hydrogen bonding). The activation energies (E_a) for the rotational motion of water molecules make this clearer. Published E_a values for D_2O in $[C_2C_1im][BF_4]$[12] and $[C_4C_1im][Cl]$[65] are shown in Figure 4.6. These measurements indicate that the rotational motion activation energy for D_2O in $[C_4C_1im][Cl]$ is much larger than for D_2O in $[C_2C_1im][BF_4]$, which indicates that the rotational motion of water is more restricted in the D_2O + $[C_4C_1im][Cl]$ system. This is likely due to the Coulombic forces between the Cl anion and the water molecules[65] and explains why the water diffusion in $[C_2C_1im][BF_4]$ is overall faster than $[C_4C_1im][Cl]$ at a given temperature and x_w. As the concentration of water increases, the E_a for $[C_4C_1im][Cl]$-D_2O decreases and approaches the E_a value of pure D_2O, suggesting water molecules have more mobility and may diffuse more easily. On the other hand, the E_a for $[C_2C_1im][BF_4]$-D_2O, after having reached a value lower than E_a of pure D_2O, appears to be increasing as $x_w > 0.3$; a behavior which has been attributed to the water-water hydrogen bonds restricting rotational motion.[12]

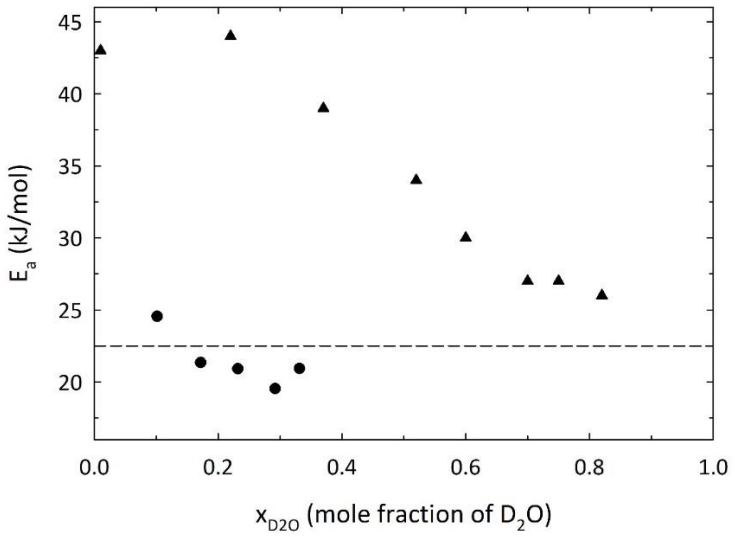

Figure 4.6. Activation energies of the rotational motion of water molecules in $[C_2C_1im][BF_4]$ and $[C_4C_1im][Cl]$ plotted as a function of D_2O mole fraction. The circles represent data measured by Takamuku et al. for $[C_2C_1im][BF_4]$, and the triangles are data measured by Yasaka et al. for $[C_4C_1im][Cl]$. The dashed line is the rotational motion activation energy of pure D_2O.[66]

Finally, looking back at the NRTL model energy interaction parameters τ_{ij}, it can be concluded that the Δg_{ij} parameters (shown in Table 3.2) provided a similar idea as the differences in enthalpy curve shown in Figure 4.5. For example, the Δg_{ij} parameters for the water-IL systems containing $[C_2C_1im][OAc]$, $[C_4C_1im][OAc]$, and $[C_4C_1im][Cl]$ showed that the water-IL interactions $|g_{21}|$ were much stronger than the water-water interactions $|g_{11}|$; similarly the ΔH_{abs} for the same systems were larger than the water-water interactions (ΔH_{vap}), as shown in Figures 4.5c-e. The g_{ij} parameters for water-IL systems containing $[C_2C_1im][BF_4]$ and $[C_2C_1im][TFES]$ showed the water-water interactions $|g_{11}|$ were much weaker than the IL-water interactions $|g_{21}|$, and their ΔH_{abs} values were also estimated to be lower than ΔH_{vap} as shown in Figures 4.5a and b.

4.4 Conclusion

A diffusion analysis was performed on the mass time-dependent data which were measured using a spherically-shaped container using two different models: one which considered the 2D diffusion behavior in a partial hemisphere, and another which applied the 1D diffusion equation employed in previous works.[25] This work demonstrated the 1D diffusion model provides satisfactory predictions and can be used to determine the water-IL diffusion coefficients. In addition, the diffusion coefficients measured with the spherically-shaped container and determined with the 1D equation for $[C_2C_1im][OAc]$ at 303.15 K were compared to diffusion coefficients for data measured in a flat cylindrical container and calculated using the 1D equation. The comparison between the two methods showed that applying the 1D diffusion model approximation for data measured in the spherical-shaped container is appropriate.

The expected increase in diffusion as viscosity decreased was confirmed for the water-IL systems containing $[C_2C_1im][TFES]$ (4.4×10^{-11} to 1.2×10^{-10} m^2/s), $[C_2C_1im][OAc]$ (4.6×10^{-12}

to 2.8 x 10^{-11} m^2/s), $[C_4C_1im][OAc]$ (8.8 x 10^{-12} to 3.9 x 10^{-11} m^2/s) and $[C_4C_1im][Cl]$ (4.5 x 10^{-12} to 2.8 x 10^{-11} m^2/s). However, an unexpected result was observed for $[C_2C_1im][BF_4]$ with a decrease in diffusion (1.3 x 10^{-10} to 2.7 x 10^{-11} m^2/s) as water concentration increased (i.e., lower viscosity). Diffusing radius calculations using the Stokes-Einstein relationship support the hypothesis that only a few water molecules through hydrogen bonding form clusters with the [OAc] and [Cl] anions, but much larger water/BF_4^- clusters/networks are forming in the $[C_2C_1im][BF_4]$ system which increase in size with increasing water concentration.

The NRTL correlations and the Clausius-Clapeyron equation were used to determine the enthalpy of absorption for the three ILs, which were compared to the water-water interactions illustrated by the heat of vaporization of water at 298 K. This assessment, along with rotational energy information and the NRTL interaction parameters, also provide further support for the differences observed in the diffusivity of water in each IL. In general, the $[C_2C_1im][BF_4]$ and $[C_2C_1im]$[TFES] display weaker interactions with water than the $[C_2C_1im][OAc]$, $[C_4C_1im][OAc]$, and $[C_4C_1im][Cl]$. It was observed, that as water concentration increased, the water-water hydrogen bonding energy began to exceed the $[C_2C_1im][BF_4]$-water interactions, and the water diffusivity decreased. On the other hand, the increase in water concentration in $[C_2C_1im][OAc]$, $[C_4C_1im][OAc]$ and $[C_4C_1im][Cl]$, decreased the interactions between water-IL, and was presumed to increase water mobility; therefore, the water diffusivity increased. For the limited water concentration range (0 – 30 mol%) in $[C_2C_1im]$[TFES], it was observed that as water concentration increased, the hydrogen bonding interactions increased, and the water diffusivity increased. Water solubility measurements in $[C_2C_1im]$[TFES] at higher RH values and water-$[C_2C_1im]$[TFES] mixture viscosities are needed to thoroughly analyze the origin for the water diffusivity behavior in this ionic liquid.

Chapter 5: Water-Induced Liquid-Liquid Equilibria in Imidazolium-based ILs

5.1 Introduction

This chapter focuses on experimental validation of an unexpected observation originally predicted by molecular simulations. This study is a perfect example of how experimental research direction can now be motivated by molecular simulations, where the simulations are performed first and lead to experimental designs.

Dr. Yong Zhang and Dr. Ed Maginn at the University of Notre Dame, Department of Chemical and Biomolecular Engineering, predicted using molecular simulations, that the addition of water to equimolar amounts of imidazolium-based ionic liquid binary mixtures ($[C_2C_1im][NTf_2]$ + $[C_2C_1im][OAc]$ and $[C_2C_1im][NTf_2]$ + $[C_2C_1im][Cl]$) at 293 K could induce a liquid-liquid phase separation. The results of this study in collaboration with Dr. Maginn and Dr. Zhang have been recently published.[67]

The simulations predicted that the first system ($[C_2C_1im][NTf_2]$:$[C_2C_1im][OAc]$) was miscible at 293 K with equimolar concentrations of the ILs. When water was added to the system (x_w = 0.83), a clear phase split could be observed; acetate anions concentrated in the water-rich phase, and the $[NTf_2]$ anions preferred the water-lean phase, as shown in Figure 5.1.

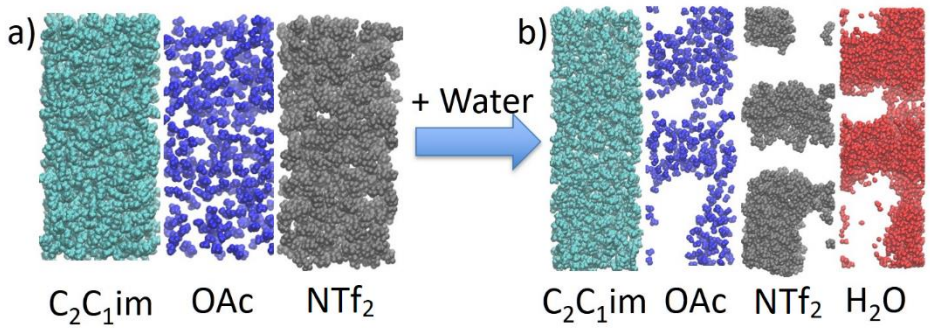

Figure 5.1. Molecular dynamic simulation snapshots of the $[C_2C_1im][NTf_2]$:$[C_2C_1im][OAc]$ mixture at 293 K, where (a) the dry system was miscible and (b) the system phase separated into a water-rich and water-lean phase at 83 mol% water. Each panel shows only $[C_2C_1im]$ (cyan), [OAc] (blue), $[NTf_2]$ (grey), or water (red). This is a modified version of the original image published by Rocha et al.[67]

The second system ([C_2C_1im][NTf_2]:[C_2C_1im][OAc]) was also predicted to be miscible at 293 K with equimolar IL concentrations. The simulation predicted a clear phase split at a water concentration of 83 mol%. In this case, the chloride anions concentrated in the water-rich phase, and the [NTf_2] anions concentrated in the water-lean phase, shown in Figure 5.2.

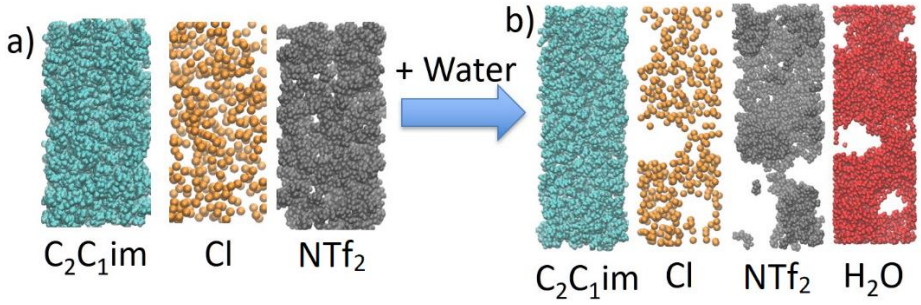

Figure 5.2. Molecular dynamic simulation snapshots of the [C_2C_1im][NTf_2]:[C_2C_1im][Cl] mixture at 293 K, where (a) the dry system was miscible and (b) the system phase separated into a water-rich and water-lean phase at 83 mol% water. Each panel shows only [C_2C_1im] (cyan), [NTf_2] (grey), [Cl] (gold), or water (red). This is a modified version of the original image published by Rocha et al.[67]

The third system ([C_2C_1im][OAc]:[C_2C_1im][Cl]) was predicted to be miscible with equimolar amounts of IL at 293 K. The simulation predicted that the system would remain miscible even after reaching 83 mol% water as shown in Figure 5.3.

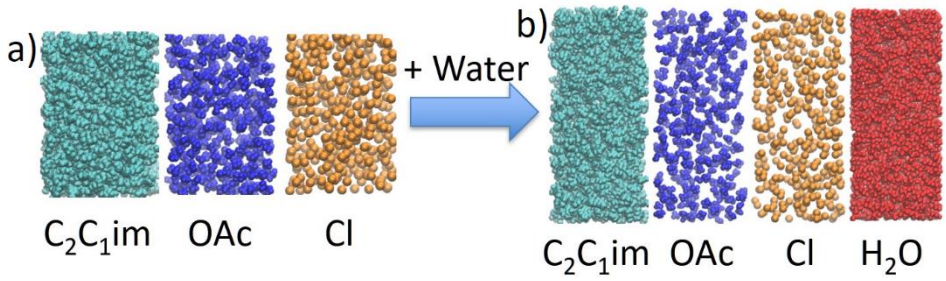

Figure 5.3. Molecular dynamic simulation snapshots of the [C_2C_1im][OAc]:[C_2C_1im][Cl] mixture at 293 K, where (a) the dry system was miscible and (b) the system remained miscible at 83 mol% water. Each panel shows only [C_2C_1im] (cyan), [OAc] (blue), [Cl] (gold), or water (red). This is a modified image of the original image published by Rocha et al.[67]

The effect of water on the phase behavior of the IL mixtures was verified experimentally, and the ionic liquid and water concentrations were determined in each phase using ^{1}H NMR, and

a combination of ^{19}F NMR, Karl Fischer titration, and ion chromatography techniques. Herein, the experimental methodology and results are discussed for the three ionic liquid systems.

5.2 Experimental

5.2.1 Materials

The ionic liquid 1-ethyl-3-methylimidazolium bis(trifluoromethylsulfonyl)imide [C_2C_1im][NTf_2] (99 % purity, Lot and filling code IL-0023-HP-1000 H00620.1, CAS no. 174899-82-2) was obtained from Iolitec. The ionic liquids 1-ethyl-3-methylimidazolium acetate [C_2C_1im][OAc] (97 % purity, Lot and Filling code BCBG2131V, CAS no. 143314-17-4) and 1-Ethyl-3-methylimidazolium chloride [C_2C_1im][Cl] (98 % purity, Lot and Filling code 6130LC, CAS no. 65039-09-0), and water (HPLC grade, lot and filling code. 3HBH9984, CAS no. 7732-18-5) were purchased from Sigma-Aldrich. The ionic liquid melting points and molecular weights are listed in Table 5.1.

Table 5.1. Molecular weight and melting point values for the ionic liquids studied

Ionic Liquid	Abbreviation	Molecular Weight	Melting Point (K)
1-ethyl-3-methylimidazolium bis(trifluoromethylsulfonyl)imide	[C_2C_1im][NTf_2]	391.31	263[68]
1-ethyl-3-methylimidazolium acetate	[C_2C_1im][OAc]	146.62	253[69]
1-ethyl-3-methylimidazolium chloride	[C_2C_1im][Cl]	170.21	357[70]

Water content in the pure ionic liquids was determined by Karl Fischer titration (Mettler Toledo DL36 Karl Fischer Coulometric Titrator) using a water standard of 94 ± 10 ppm H_2O (Apura ®, Merck KGaA, Prod. no. 1.88050.0010, Lot code HC61276950). The Karl Fischer results for [C_2C_1im][NTf_2], [C_2C_1im][OAc], and [C_2C_1im][Cl] were 202 ppm ± 16 ppm, 4449 ppm

± 724 ppm, and 4752 ppm ± 210 ppm, respectively. The ionic liquids were used as-is with no additional drying as water concentration was accounted for and would not impact the final phase results.

The chemicals used in the NMR studies were: deuterated benzene (99.6 atom % D, Lot code MKCD3810, CAS no. 1076-43-3), deuterated dimethyl sulfoxide (99.5 % purity, Lot code Y30D065, CAS no. 2206-27-1, 2,4 dichloro-benzotrifluoride (99.51 % purity, Lot code BCBT0752, CAS no. 320-60-5.), 2-chloro-4-fluorotoluene (99.57 % purity, Lot code BCBR0116, CAS no. 452-73-3.). The mixed anion standard (VeriSpec^{TM} Mixed Anion Standard, Lot code 8706040, CAT no. RV010685-100N) was a purchased from RICCA and utilized for the ion chromatography measurements.

5.2.2 Methodology

Clear borosilicate glass tubes (approx. 7 ml capacity) were used to initially observe the presence of liquid-liquid separation in the IL-IL-water ternary mixtures. The tubes were cleaned with acetone and dried in a vacuum oven at 343.15 ± 1 K. A stainless steel (SS316), Swagelok® cap and plug with Teflon® ferrules were used to seal one end of the tube. The ferrules were tightened over the tubes with caution to prevent damaging the glass.

The tubes were placed on a balance and the ILs were added as quickly as possible to prevent atmospheric water absorption. The tubes were mixed for 2 hours using a rocking table at room temperature (295 K ± 1 K). Subsequently, the tubes were left standing upright for a minimum of 12 hours to stabilize at room temperature. Water was added in increments of 10 to 30 mg, and the tubes were again mixed and left to sit for a minimum of 12 hours. This last step was repeated until liquid-liquid equilibrium was observed.

After determining the concentrations of water at which the room temperature liquid-liquid equilibrium was induced in the equimolar ionic liquid system, the concentration of each species in each phase were analyzed. Larger amounts of the IL-IL-water mixtures were made in the same compositions as determined by the borosilicate glass tube test, and each were loaded into separatory funnels. Most of the top liquid phase was collected using a glass pipette. The bottom phase was drained out of the funnel and collected. Residues of the top liquid phase were collected separately and accounted for in the total mass for each phase. Each liquid phase was analyzed for determination of the species concentration with ^{1}H NMR, ^{19}F NMR, Karl Fischer, and/or ion chromatography depending on the species being determined.

5.3 Results and Discussion

The following sections will report the phase-equilibrium results and detail the analytical techniques applied to determine the concentrations of each liquid phase. The uncertainty calculations can be found in Appendix B.

5.3.1 $[C_2C_1im][NTf_2]$:$[C_2C_1im][OAc]$:H_2O System

The equimolar mixture of $[C_2C_1im][NTf_2]$ and $[C_2C_1im][OAc]$ with residual water (2.3 ± 1.2 mol%) was a homogeneous clear liquid at 295 ± 1 K as shown in Figure 5.4. Upon initial addition of water, cloudiness could be observed at points of contact between the IL mixture and water, and a noticeable amount of heat was released, resulting in a temperature increase estimated to be less than 10 K. This heat is attributed to the exothermic process of hydrogen bonding between water molecules and acetate ions.[71,72] Water concentration at 54 ± 1 mol% resulted in a liquid-liquid phase split (see Figure 5.4). If more water were to be added to the system, it would continue to be phase separated. Therefore, the results validated the simulation predictions that a mixture of

$[C_2C_1im][NTf_2]$, $[C_2C_1im][OAc]$, and water at a concentration of 82 mol% H_2O would exhibit phase separation.

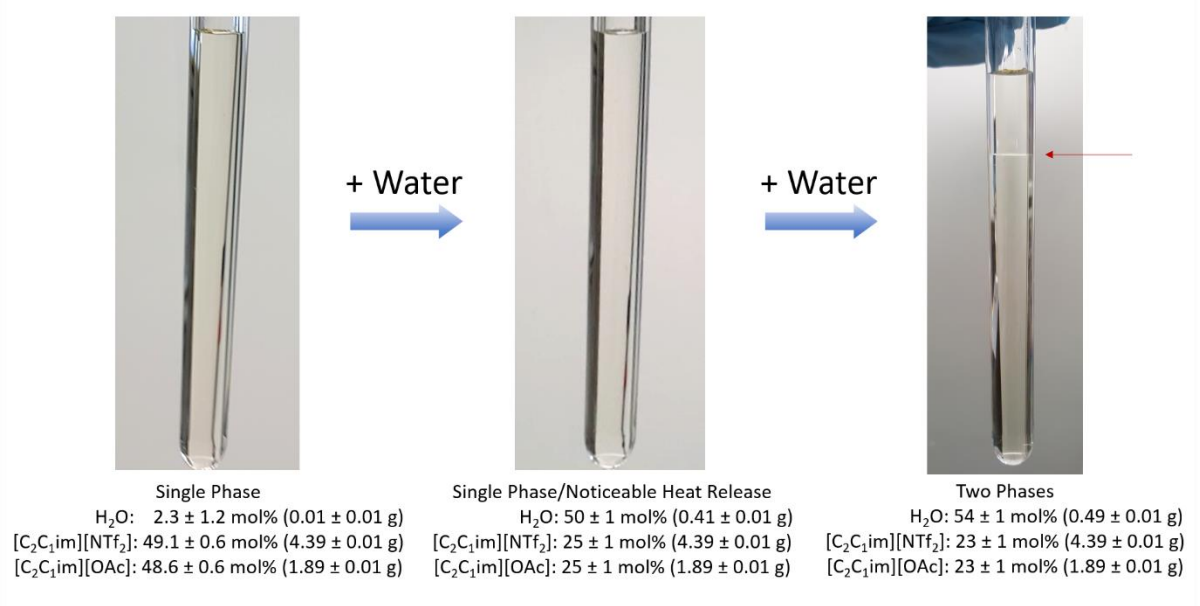

Figure 5.4. Experimental results for $[C_2C_1im][NTf_2]$:$[C_2C_1im][OAc]$:H_2O at 295 ± 1 K with increasing water content. This is a modified version of the original image published by Rocha et al.[67]

Larger quantities of the $[C_2C_1im][NTf_2]$:$[C_2C_1im][OAc]$:H_2O mixture were prepared at the same composition where the liquid-liquid phase split occurred. The phases were separated and weighed. Both phases were analyzed using ^1H NMR, as the protons in $[C_2C_1im]^+$ cations, $[OAc]^-$ anions, and water could be observed. The concentration of each component could therefore be determined as a ratio to one another. Deuterated benzene was selected as the lock solvent for this system and loaded into a coaxial tube (Wilmad-LabGlass WGS-5BL). The samples were measured using a 500 MHz Bruker AVIII spectrometer equipped with a cryogenically-cooled broadband observe probe, and the peak analysis was performed with Mestrenova V12.0. Figure 5.5 shows the ^1H NMR spectra for a mixture of $[C_2C_1im][NTf_2]$, $[C_2C_1im][OAc]$, and H_2O and includes the peaks labeled correspondingly to the protons on the chemical structures. The integrals or areas of

the peaks were obtained using the Mestrenova program. NMR spectra for the top and bottom phases of the $[C_2C_1im][NTf_2]$:$[C_2C_1im][OAc]$:H_2O mixture are shown in Appendix B.

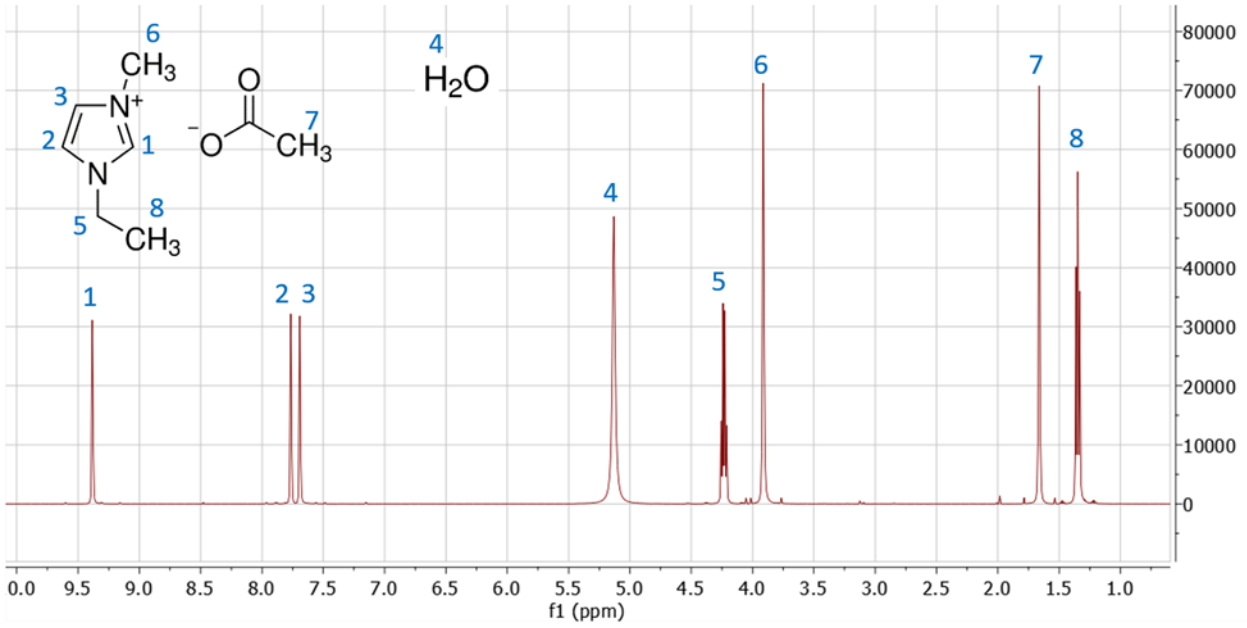

Figure 5.5. ^{1}H NMR spectra for $[C_2C_1im][NTf_2]$:$[C_2C_1im][OAc]$:H_2O mixture [a] with peak assignments.
[a] The overall composition was 22.33 mol% $[C_2C_1im][NTf_2]$, 22.45 mol% $[C_2C_1im][OAc]$, and 55.21 mol% H_2O

The equations used to calculate the concentrations are shown below, where a_k is the area corresponding to the kth peak and n_k is the number of protons related to the kth peak. The $[C_2C_1im][NTf_2]$ area is a_T, a_O is the area related to $[C_2C_1im][OAc]$ ($a_O = a_7$) , and a_H is the area related to H_2O ($a_H = a_4$). Equation 5.1 is calculating the representative $[C_2C_1im][NTf_2]$ a_T/n_T terms by using the $[C_2C_1im]$ a_k/n_k normalized areas and subtracting a_O/n_O. This applies the assumption that the $[C_2C_1im]$ ions which are not paired with the acetate ions are paired with the $[NTf_2]$ ions.

$$\frac{a_T}{n_T} = \frac{\frac{a_1}{n_1}+\frac{a_2}{n_2}+\frac{a_3}{n_3}+\frac{a_5}{n_5}+\frac{a_6}{n_6}+\frac{a_8}{n_8}}{6} - \frac{a_O}{n_O} \qquad (5.1)$$

The areas are shown in Table 5.2.

Table 5.2. Areas for the ^{1}H NMR peaks in the $[C_2C_1im][NTf_2]$:$[C_2C_1im][OAc]$:H_2O mixture[a]

	Top Phase		Bottom Phase		*n*
Peak #	Range (ppm)	Absolute Area	Range (ppm)	Absolute Area	Hydrogens Associated to Peak
1	9.46 ... 9.32	1222413	9.20 ... 9.03	1960416	1
2	7.85 ... 7.73	1230121	7.67 ... 7.56	1956296	1
3	7.73 ... 7.57	1239064	7.56 ... 7.44	1965908	1
4	5.47 ... 4.73	5745530	5.15 ... 4.71	3249794	2
5	4.34 ... 4.14	2450466	4.33 ... 4.13	3885821	2
6	4.00 ... 3.80	3661615	3.97 ... 3.76	5816858	3
7	1.76 ... 1.56	3004051	1.81 ... 1.64	2127089	3
8	1.43 ... 1.25	3669714	1.52 ... 1.31	5864053	3

[a] The overall composition was 22.33 mol% $[C_2C_1im][NTf_2]$, 22.45 mol% $[C_2C_1im][OAc]$, and 55.21 mol% H_2O

The mole fractions of each species were calculated using Eqs. 5.2 to 5.4.

$$[\mathrm{C_2mim}][\mathrm{NTf_2}]\ \text{mole fraction} = x_T = \frac{a_T/n_T}{a_T/n_T + a_O/n_O + a_H/n_H} \tag{5.2}$$

$$[\mathrm{C_2mim}][\mathrm{OAc}]\text{mole fraction} = x_O = \frac{a_O/n_O}{a_T/n_T + a_O/n_O + a_H/n_H} \tag{5.3}$$

$$\mathrm{H_2O}\ \text{mole fraction} = x_H = \frac{a_H/n_H}{a_T/n_T + a_O/n_O + a_H/n_H} \tag{5.4}$$

The moles of each phase (N_{top} and N_{bot}) were calculated using Eqs. 5.5 to 5.10 by solving Eqs. 5.11 and 5.12, where x_{ij} is the mole fraction of species *J* in the *ith* phase, MW_j is the molecular weight of species *J* and T_{molJ} is the total moles of species *J* (T = $[C_2C_1im][NTf_2]$, O = $[C_2C_1im][OAc]$, and H = H_2O). $T_{WJActual}$ is the measured total mass of species *J* in the $[C_2C_1im][NTf_2]$:$[C_2C_1im][OAc]$:H_2O system.

$$T_{molT} = x_{topT}N_{top} + x_{botT}N_{bot} \tag{5.5}$$

$$T_{molO} = x_{topO}N_{top} + x_{botO}N_{bot} \quad (5.6)$$

$$T_{molH} = x_{topH}N_{top} + x_{botO}N_{bot} \quad (5.7)$$

$$T_{WT} = x_{topT}N_{top}MW_T + x_{botT}N_{bot}MW_T \quad (5.8)$$

$$T_{WO} = x_{topO}N_{top}MW_O + x_{botO}N_{bot}MW_O \quad (5.9)$$

$$T_{WH} = x_{topH}N_{top}MW_H + x_{botH}N_{bot}MW_H \quad (5.10)$$

$$mol\ error = Abs\left|\frac{T_{WJActual}}{MW_J} - T_{molJ}\right|^2 \quad (5.11)$$

$$mass\ error = Abs\left|T_{WJActual} - T_{molJ}MW_J\right|^2 \quad (5.12)$$

The total mass and moles of each species in the bottom and top phases are listed in Table 5.3 and the mole % and mass % concentrations are listed in Table 5.7.

Table 5.3 Mole and mass amounts in the top and bottom phases of the $[C_2C_1im][NTf_2]$:$[C_2C_1im][OAc]$:H_2O system[a]

Comp.	Top Phase (moles)	Bottom Phase (moles)	Top Phase (g)	Bottom Phase (g)
$[C_2C_1im][NTf_2]$	$(0.342 \pm 0.082) \times 10^{-2}$	$(2.724 \pm 0.112) \times 10^{-2}$	1.338 ± 0.322	10.66 ± 0.44
$[C_2C_1im][OAc]$	$(1.519 \pm 0.229) \times 10^{-2}$	$(1.553 \pm 0.111) \times 10^{-2}$	2.585 ± 0.389	2.64 ± 0.19
H_2O	$(4.357 \pm 0.663) \times 10^{-2}$	$(3.558 \pm 0.205) \times 10^{-2}$	0.785 ± 0.120	0.64 ± 0.04
Total	$(6.218 \pm 0.706) \pm 10^{-2}$	$(7.835 \pm 0.259) \times 10^{-2}$	4.708 ± 0.519	13.94 ± 0.48

[a] The overall composition was 22.33 mol% $[C_2C_1im][NTf_2]$, 22.45 mol% $[C_2C_1im][OAc]$, and 55.21 mol% H_2O

The phase partitions were calculated for each species (Equation 5.13) and for the overall system (Equation 5.14), where P_{iJ} is the phase partition of species *J* in the *ith* phase, w_{iJ} is the mass percent of species *J* in the *ith* phase. The partition results are shown in Tables 5.4 and 5.5.

$$P_{IJ} = \frac{x_{iJ}N_i}{x_{topJ}N_{top} + x_{botJ}N_{bot}} = \frac{w_{iJ}T_{Wi}}{w_{topJ}T_{Wtop} + w_{botJ}T_{Wbot}} \quad (5.13)$$

$$P_{T_{Wi}} = \frac{T_{Wi}}{T_{Wtop}+T_{Wbot}} \quad (5.14)$$

Table 5.4 Phase partition results (in wt. % or mol%) for the $[C_2C_1im][NTf_2]$:$[C_2C_1im][OAc]$:H_2O mixture[a] determined with the ^1H NMR technique

Phase	$[C_2C_1im][NTf_2]$	$[C_2C_1im][OAc]$	H_2O
Top Phase	11.15 ± 2.42 %	49.45 ± 4.16 %	55.05 ± 4.03 %
Bottom Phase	88.85 ± 2.42 %	50.55 ± 4.16 %	44.95 ± 4.03 %

[a] The overall composition was 22.33 mol% $[C_2C_1im][NTf_2]$, 22.45 mol% $[C_2C_1im][OAc]$, and 55.21 mol% H_2O

Table 5.5 Overall phase partition results (in wt.% or mol%) for the $[C_2C_1im][NTf_2]$:$[C_2C_1im][OAc]$:H_2O mixture[a]

Phase	Calculated	Measured
Top	24.24 ± 2.47	26.16 ± 0.15
Bottom	74.76 ± 2.47	73.84 ± 0.15

[a] The overall composition was 22.33 mol% $[C_2C_1im][NTf_2]$, 22.45 mol% $[C_2C_1im][OAc]$, and 55.21 mol% H_2O

The mass of the top (4.7078 ± 0.5187 g) and bottom (13.9447 ± 0.4784 g) phases were significantly close to the measured amounts in the top phase (4.7653 ± 0.0348 g) and bottom phase (13.4522 ± 0.0284 g). In addition, the water content was measured by Karl Fischer as shown in Table 5.6. Comparing the measured and calculated water concentration (Table 5.7), the results were within 1% of the water mass concentrations obtained using ^1H NMR. Therefore, the ^1H NMR methodology is considered an excellent technique to determine the concentration of species in the $[C_2C_1im][NTf_2]$:$[C_2C_1im][OAc]$:H_2O mixture.

Table 5.6 Karl Fischer measurements for water content in each phase of the $[C_2C_1im][NTf_2]$;$[C_2C_1im][OAc]$:H_2O system[a]

Measurement	Top Phase (%)	Bottom Phase (%)
1	15.95	4.29
2	16.42	4.26
3	15.66	4.33
4	16.26	4.33
5	15.93	4.33
6	16.05	--
Average	16.05 ± 0.27	4.31 ± 0.03

[a] The overall composition was 22.33 mol% $[C_2C_1im][NTf_2]$, 22.45 mol% $[C_2C_1im][OAc]$, and 55.21 mol% H_2O

Table 5.7 The phase concentrations determined by ^1H NMR and the Karl Fischer results for water content of $[C_2C_1im][NTf_2]$;$[C_2C_1im][OAc]$:H_2O system[a]

Phase	Component	Measured by ^1H NMR (mole %)	Calculated by ^1H NMR (mass %)	Measured by Karl Fischer (mass %)
Top	$[C_2C_1im][NTf_2]$	5.50 ± 1.57	28.41 ± 5.83	--
	$[C_2C_1im][OAc]$	24.42 ± 1.11	54.91 ± 4.59	--
	H_2O	70.08 ± 1.54	16.68 ± 1.44	16.05 ± 0.27
Bottom	$[C_2C_1im][NTf_2]$	34.77 ± 1.50	76.45 ± 1.20	--
	$[C_2C_1im][OAc]$	19.82 ± 1.25	18.95 ± 1.15	--
	H_2O	45.41 ± 1.21	4.60 ± 0.20	4.31 ± 0.03

[a] The overall composition was 22.33 mol% $[C_2C_1im][NTf_2]$, 22.45 mol% $[C_2C_1im][OAc]$, and 55.21 mol% H_2O

It is clear from Table 5.7 that the top liquid phase was rich in water and $[C_2C_1im][OAc]$, and the bottom liquid phase was rich in $[C_2C_1im][NTf_2]$. These results are reasonable as the [OAc] anion has a stronger affinity for water than the $[NTf_2]$ anion, and the density of $[C_2C_1im][NTf_2]$ is greater than that of water and $[C_2C_1im][OAc]$. Therefore, the majority of $[C_2C_1im][NTf_2]$ was

present in the bottom liquid phase. It was assumed the [C_2C_1im] cations were distributed among both phases, according to the concentration of each anion, to maintain neutrality in each phase. Figure 5.6 summarizes the phase concentration of the [C_2C_1im][NTf_2]:[C_2C_1im][OAc]:H_2O mixture.

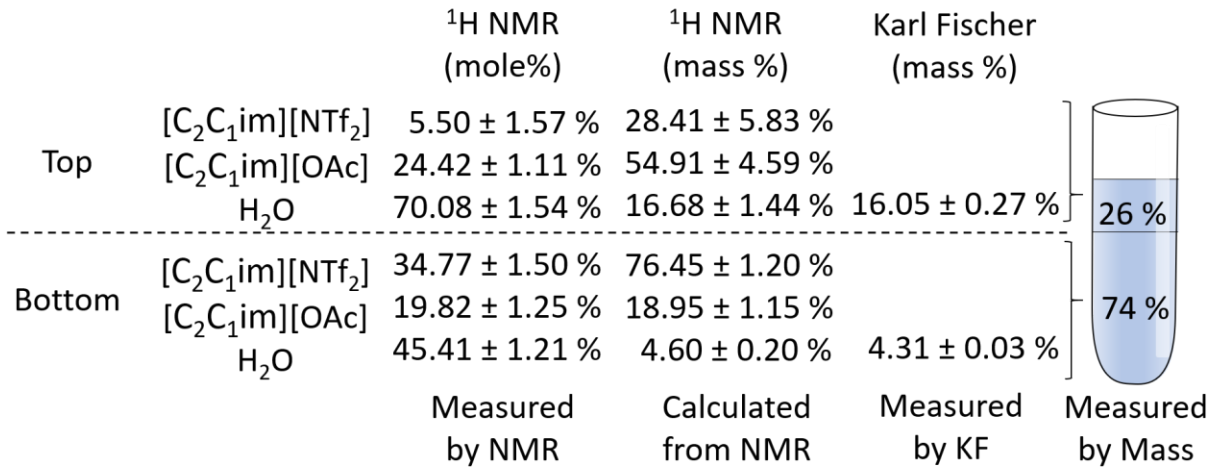

Figure 5.6. Phase concentration results for [C_2C_1im][NTf_2]:[C_2C_1im][OAc]:H_2O mixture[a] determined by ^{1}H NMR, and Karl Fischer was used to confirm water content. This is a modified version of the original image published by Rocha et al.[67]

[a] The overall composition was 22.33 mol% [C_2C_1im][NTf_2], 22.45 mol% [C_2C_1im][OAc], and 55.21 mol% H_2O.

5.3.2 [C_2C_1im][NTf_2]:[C_2C_1im][Cl]:H_2O System

The second system in this study was the equimolar [C_2C_1im][NTf_2] and [C_2C_1im][Cl] mixture. The [C_2C_1im][Cl] is present in the form of solid green-colored crystals at 295 K. Color in ionic liquids can originate from the presence of trace metal impurities. Measurements with inductively coupled plasma mass spectrometry (ICP-MS) determined the [C_2C_1im][Cl] contained 90-130 ppm Ni. The anhydrous salt nickel(II) chloride ($NiCl_2$) is known to be yellow and the more familiar hydrate $NiCl_2 \cdot 6H_2O$ is green. However, the trace levels of metal hydrate will have no effect on the LLE measurements. When [C_2C_1im][NTf_2] and [C_2C_1im][Cl] were initially combined, they remained in a heterogeneous solid-liquid solution as shown in Figure 5.7, until the

concentration of water was increased to about 20 mol%. At this stage, all the $[C_2C_1im][Cl]$ had dissolved and the mixture was a homogeneous green color. This color persisted as the system partitioned into a two-phase mixture at 41 ± 1 mol% H_2O. The study reports the phase split at 39 ± 3 % H_2O because water was added in small increments, and the concentration of water prior to 41 mol% was 37 ± 1 mol% with no phase partition. Therefore, the phase split was assumed to occur at a concentration of 39 ± 3 mol%. The experimental results validate the simulation results, indicating that water addition to an equimolar mixture of $[C_2C_1im][NTf_2]$ and $[C_2C_1im][Cl]$ can induce a liquid-liquid phase separation.

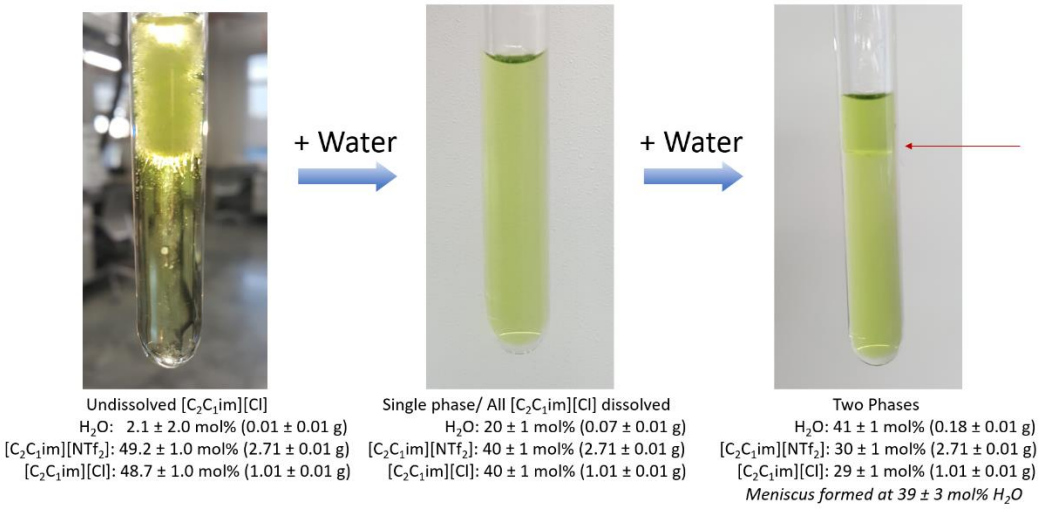

Figure 5.7. Experimental results for $[C_2C_1im][NTf_2]$:$[C_2C_1im][Cl]$:H_2O at 295 ± 1 K with increasing water content. This is a modified version of the original image published by Rocha et al.[67]

As was performed with the first system, a larger amount of solution was created for the $[C_2C_1im][NTf_2]$:$[C_2C_1im][Cl]$ mixture at the 39 ± 3 mole % composition. Each phase was separated and analyzed by ^{19}F NMR applying the methodology described by Henderson[73] and utilizing a 500 MHz Bruker AVIII spectrometer. The method utilizes a coaxial insert tube with a reference standard (2,4 dichlorobenzotrifluoride) for quantitative NMR spectroscopy. The usage of the coaxial tube was accounted using Henderson's methodology by calculating the ratio of the

insert volume (V_R) to that of the NMR sample tube (V_T). This was done for two sets of coaxial inserts.

Henderson's[73] main equation is effectively Eq. 5.15, where C_T is, in this study, the concentration of $[C_2C_1im][NTf_2]$ in moles per volume. The term I_T/I_R is the integral signal ration of $[C_2C_1im][NTf_2]$ to the reference compound. The term V_R/V_T is the ratio of the coaxial tube volume to the sample tube volume detected by the NMR coil.

$$C_T = (C_R)\left(\frac{I_T}{I_R}\right)\left(\frac{V_R}{V_T}\right) \tag{5.15}$$

The volume ratios were experimentally determined using three solutions: A, B, and C which used DMSO as a solvent, shown in Table 5.8. Solutions A, B and C consisted of diluted amounts of 2,4 dichlorobenzotrifluoride, 2-chloro-4-fluorotoluene, and $[C_2C_1im][NTf_2]$, respectively.

Table 5.8. Compositions of mixtures A, B, and C. The volume and molar concentration of solution C were not required for further calculations. The uncertainties for values in this table were not required for further calculations.

Soln	DMSO (g)	2,4 Dichloro-benzotrifluoride (g)	2-Chloro-4-fluorotoluene (g)	$[C_2C_1im][NTf_2]$ (g)	Fluorine molecules	Peak region (ppm)	Total Vol (ml)	Conc (mol/ml)
A	2.7017	0.6379	--	--	3	~-62	2.645	0.001122
B	2.7105	--	0.4579	--	1	~-115	2.706	0.001170
C	2.5395	--	--	1.5092	6	~-79	--	--

The compounds 2,4 dichloro-benzotrifluoride, 2-chloro-4-fluorotoluene, and $[C_2C_1im][NTf_2]$ were used because each of these compounds have distinct NMR fluorine peaks and allowed the researcher to view two signals when placing one of the solutions in the coaxial tube and another in the NMR sample tube. The absolute peak integrals are divided by the number

of fluorine atoms in their specific compound and then compared, as shown in Table 5.9. Using Eq. 5.15, if the concentrations of the liquids inside each tube are equal, and the integral ratios are known, then the volume ratios can be determined.

Solution A and solution B were not the same concentration, therefore, the solutions were each compared against solution C, as shown in Table 5.9 with Measurements 2.1 to 3.2. Comparison of I_{Coax}/I_{Tube} for Measurement 2.1 to 3.1 gave a ratio of A/B = 1.0660, and a comparison of Measurement 2.2 to 3.2 gave a ratio of A/B = 0.87823. Therefore, the average (0.97214) was used as a correction factor, $Z_{A/B}$.

Table 5.9. Combinations of coaxial and NMR sample content with their absolute and normalized peak integrals listed for both the coaxial tube and the sample NMR tube, as well as the normalized integral ratio

Meas.	Set	Coaxial Tube	NMR Sample Tube	Absolute Area of Coaxial Tube Species	Absolute Area of NMR Sample Tube Species	Normalized Area of Coaxial Tube Species	Normalized Area of NMR Sample Tube Species	I_{Coax}/I_{Tube}
1.1	I	A	B	213634	574436	71211.3	574436	0.123968
1.2	II	B	A	32448	747248	32448	249083	0.13027
2.1	I	A	C	47655	819671	15885	136612	0.11628
2.2	II	B	C	17719	956985	17719	159497	0.11109
3.1	I	B	C	15924	875938	15924	145990	0.10908
3.2	II	A	C	42420	869598	14140	144933	0.09756
4.1	I	B	A	32875	776891	32875	258964	0.12695
4.2	II	A	B	192944	597061	64314.7	597061	0.107718
5.1	I	B	A	35878	838312	35878	279437	0.12839
5.2	II	A	B	189405	598692	63135.1	598692	0.105460

The volume ratio of the coaxial tube volume to the sample tube volume was tested three times for each set, using the following equation.

$$\frac{V_R}{V_T} = \frac{V_{Coax}}{V_{Tube}} = \frac{I_{Coax}}{I_{Tube}} * Z_{Tube/Coax} \tag{5.16}$$

For example, Set I with Measurement 1.1, uses $Z_{B/A}$ (=1/$Z_{A/B}$) because Solution A is in the coaxial tube and solution B is in the sample tube:

$$\frac{V_R}{V_T} = \frac{V_{Coax}}{V_{Tube}} * \frac{1}{Z_{A/B}} = 0.12398 * 1/0.97214 = 0.12752 \tag{5.17}$$

And for Set I with Measurement 4.1, $Z_{A/B}$ is directly used:

$$\frac{V_R}{V_T} = \frac{V_{Coax}}{V_{Tube}} * Z_{A/B} = 0.12695 * 0.97214 = 0.12341 \tag{5.18}$$

The average for each set of tubes was determined, as shown in Table 5.10. It is important to note that between every measurement, each set of tubes was cleaned thoroughly with acetone and placed in a sonicating bath three times and dried at room temperature in a vacuum oven.

Table 5.10. Determination of coaxial tube to sample tube ratio

	V_R/V_T			
Set	Meas. 1	Meas. 4	Meas. 5	Average
I	0.12752	0.12341	0.12481	0.12525
II	0.12664	0.11081	0.10848	0.11531

The reference concentration was prepared with 0.9825 ± 0.0004 g of deuterated DMSO and 0.3730 ± 0.0004 g of 2,4-dichlobenzotrifluoride in a 5 mL vial where the liquid level was marked (standard deviation of the weight recording is 4.7 x 10^{-5} g). The liquid was transferred to

a different container, and the 5 mL vial was cleaned. The volume of the reference solution was determined four times by weighing the mass of HPLC grade water needed to reach the marked liquid level in the 5 mL vial at 294.08 K (as determined by the Fluke Standard Platinum Resistance Thermometer S/N 1113, product max deviation ±0.025 K). The density of water at 294.08 K (0.998013 g/mL)[74] was used to calculate the volume. The data are shown in Table 5.11.

Table 5.11. Determination of standard mix

Trial	Water (g)	Volume (mL)
1	1.1318 ± 0.0004	1.1340 ± 0.0004
2	1.1502 ± 0.0004	1.1525 ± 0.0004
3	1.0952 ± 0.0004	1.0974 ± 0.0004
4	1.1329 ± 0.0004	1.1352 ± 0.0004
Average	1.1275 ± 0.0002	1.1298 ± 0.0002

The value C_R for Eq. 5.15 was determined by dividing the moles of 2,4-dichlobenzotrifluoride by the volume average 1.1298 ± 0.0002 mL. Thus, C_R is equal to 0.0015 ± 0.0001 mol/ml. The reference mixture was loaded into coaxial tubes I and II. A sample of the top phase was loaded into the NMR sample tube I, and a sample of the bottom phase was loaded into the NMR sample tube II. Sets I and II were analyzed using ^{19}F NMR, and the NMR spectra (Figure 5.8 and Figure 5.9) were analyzed using Mestrenova v12. The peaks of interest were ~ -61 ppm for the fluorine content in 2,4-dichlobenzotrifluoride and ~ -80 ppm for the fluorine content in the $[C_2C_1im][NTf_2]$-containing mixture.

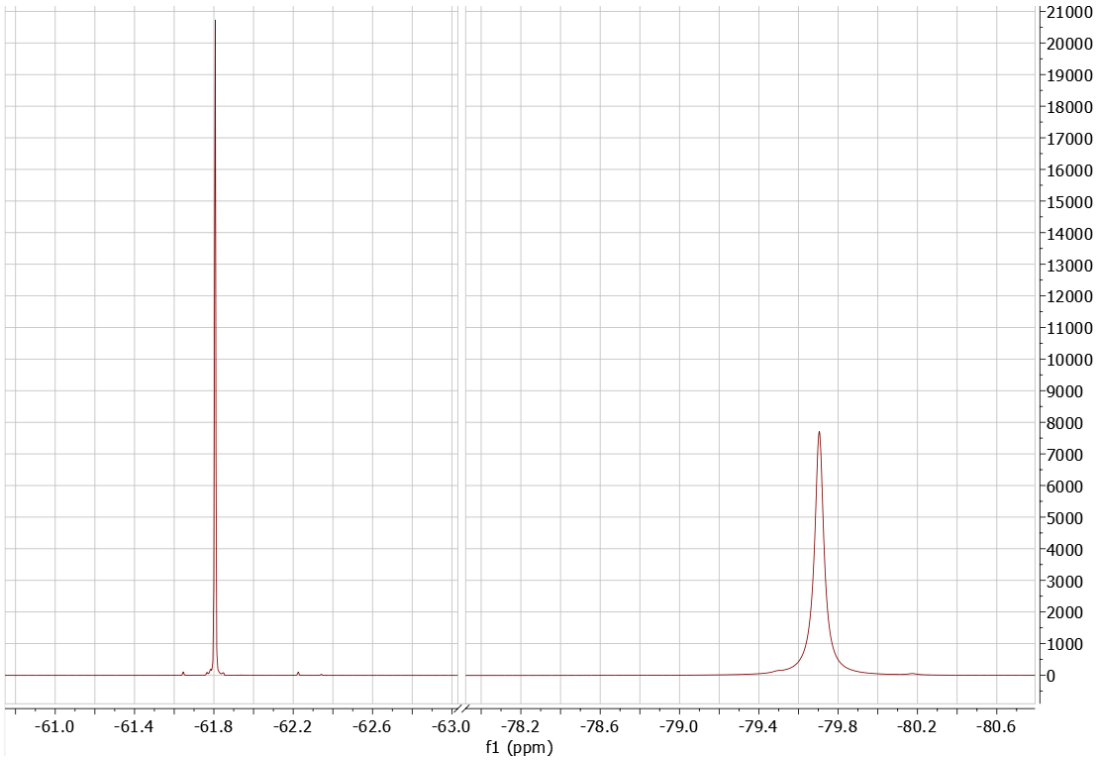

Figure 5.8. ^{19}F NMR spectra for top liquid phase of $[C_2C_1im][NTf_2]$:$[C_2C_1im][Cl]$:H_2O mixture[a]
[a] The overall composition was 29.72 mol% $[C_2C_1im][NTf_2]$, 29.85 mol% $[C_2C_1im][Cl]$, and 40.43 mol% H_2O

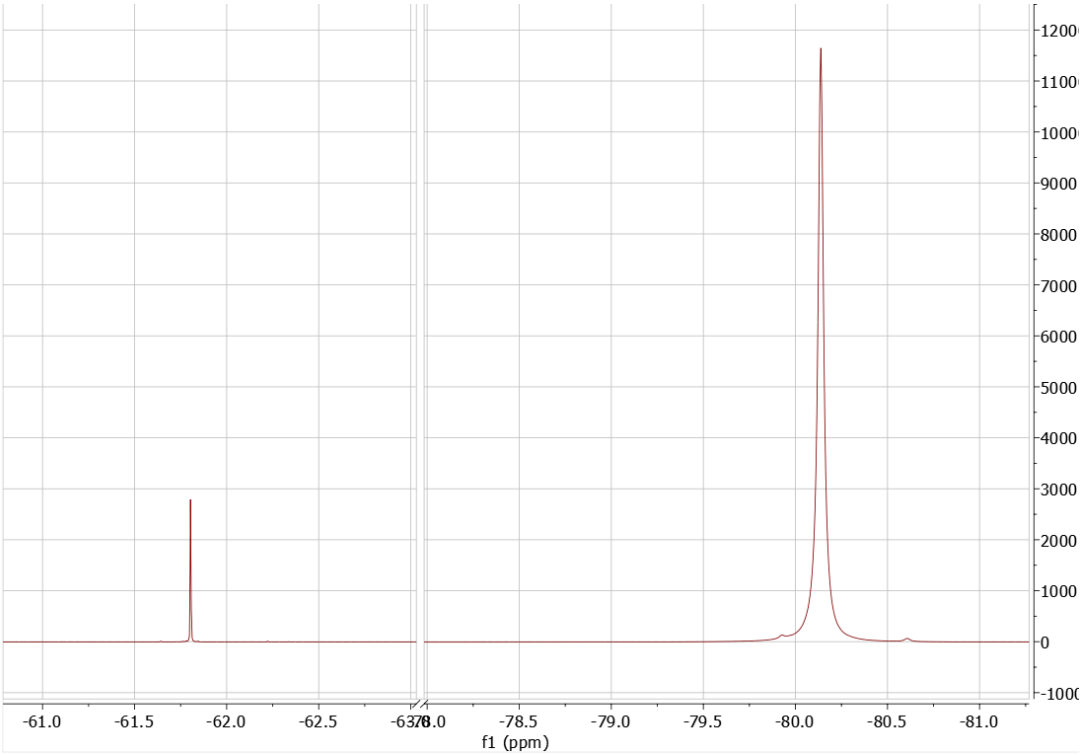

Figure 5.9. ^{19}F NMR spectra for bottom liquid phase of $[C_2C_1im][NTf_2]$:$[C_2C_1im][Cl]$:H_2O mixture [a]
[a] The overall composition was 29.72 mol% $[C_2C_1im][NTf_2]$, 29.85 mol% $[C_2C_1im][Cl]$, and 40.43 mol% H_2O

The spectra were first processed as recommended by MestreNova in a qNMR webinar[75] to perform an accurate quantitative determination of fluorine content. The "Linear Fitting" advanced feature with a Lorentzian-Gaussian shape type was applied to remove the effect of minor peaks. Three integration measurements were performed on the same sample with Mestrenova for each phase as listed in Table 5.12 and Table 5.13. The peak integral, or area, values were divided by the number of fluorine atoms related to the compound. The I_T/I_R was determined by dividing the area per molecule of the $[C_2C_1im][NTf_2]$ by that of the 2,4-dichlorobenzotrifluoride.

Table 5.12. ^{19}F NMR integral data for 2,4-dichlorobenzotrifluoride and $[C_2C_1im][NTf_2]$ for the top liquid phase of $[C_2C_1im][NTf_2]$:$[C_2C_1im][Cl]$:H_2O mixture [a] and determination of I_T/I_R

Species	Meas. 1	Meas. 2	Meas. 3	Avg. Area	Avg. Area/# F	I_T/I_R
$[C_2C_1im][NTf_2]$	657632	663527	663172	661444	110241 ± 450	1.64387 ± 0.02951
2,4-dichloro-benzotrifluoride	199901	208348	195305	201185	67061.5 ± 1801.5	

[a] The overall composition was 29.72 mol% $[C_2C_1im][NTf_2]$, 29.85 mol% $[C_2C_1im][Cl]$, and 40.43 mol% H_2O

Table 5.13. ^{19}F NMR integral data for 2,4-dichlorobenzotrifluoride and $[C_2C_1im][NTf_2]$ for the bottom liquid phase of the $[C_2C_1im][NTf_2]$:$[C_2C_1im][Cl]$:H_2O mixture [a] and determination of I_T/I_R

Species	Meas. 1	Meas. 2	Meas. 3	Avg. Area	Avg. Area/#F	I_T/I_R
$[C_2C_1im][NTf_2]$	662689	645553	670477	659573	109929 ± 1735	17.4354 ± 0.2485
2,4-dichloro-benzotrifluoride	18802	19421	18522	18914.8	6304.93 ± 125.24	

[a] The overall composition was 29.72 mol% $[C_2C_1im][NTf_2]$, 29.85 mol% $[C_2C_1im][Cl]$, and 40.43 mol% H_2O

The total mass of each phase was determined: 5.7030 ± 0.0284 g in the top phase and 32.4950 ± 0.0367 g in the bottom phase. Additionally, the volume of both phases were determined by marking the liquid level on the funnel and weighing the amount of water needed to fulfill the markings at 294.52 K three times (density: 0.997904 g/mL[74]). The results are shown in Table 5.14. Mass error for top phase and bottom phase measurements are 0.0007 g and 0.0116 g, respectively.

Table 5.14. Volume determination for top and bottom phase of the $[C_2C_1im][NTf_2]$:$[C_2C_1im][Cl]$:H_2O mixture[a] using three measurements

Phase	Meas. 1 (g)	Meas. 2 (g)	Meas. 3 (g)	Avg. Mass of Water (g)	Volume (ml)
Top	5.3040	5.6313	4.9925	5.3093 ± 0.0004	5.3204 ± 0.0004
Bottom	23.1653	22.4666	23.1252	22.9190 ± 0.0067	22.967 ± 0.0067

[a] The overall composition was 29.72 mol% $[C_2C_1im][NTf_2]$, 29.85 mol% $[C_2C_1im][Cl]$, and 40.43 mol% H_2O

Using Eq. 5.15 and all the data determined thus far, the concentration of $[C_2C_1im][NTf_2]$ in both phases were calculated and are shown in Table 5.15.

Table 5.15.Concentration and amounts of $[C_2C_1im][NTf_2]$ present in the top and bottom phase of the $[C_2C_1im][NTf_2]$:$[C_2C_1im][Cl]$:H_2O mixture[a]

Phase	Concentration (mol/mL)	Moles	Mass (g)
Top	$(3.1617 \pm 0.0961) \times 10^{-4}$	$(0.16822 \pm 0.0051) \times 10^{-2}$	0.65825 ± 0.0200
Bottom	$(3.0873 \pm 2.2984) \times 10^{-4}$	$(7.0905 \pm 0.52789) \times 10^{-2}$	27.746 ± 2.0657

[a] The overall composition was 29.72 mol% $[C_2C_1im][NTf_2]$, 29.85 mol% $[C_2C_1im][Cl]$, and 40.43 mol% H_2O

The water content was determined with Karl Fisher after concluding that ^1H NMR would not provide accurate results because the spectra was unclear and illustrated convoluted peaks. Both a volumetric and a coulometric titrator were used. First, the Mettler Toledo V20 volumetric titrator was used to determine the water content in both phases of the $[C_2C_1im][NTf_2]$:$[C_2C_1im][Cl]$:H_2O mixture, the results are shown in Table 5.16.

Table 5.16. Water concentration results for the $[C_2C_1im][NTf_2]$:$[C_2C_1im][Cl]$:H_2O mixture[a] determined with volumetric Karl Fischer titration

	Top Phase		Bottom Phase	
Measurement	Sample (g)	Water (wt.%)	Sample (g)	Water (wt.%)
1	0.0975	14.76	0.2467	2.05
2	0.0395	14.54	0.7843	2.03
3	0.1648	14.59	0.8652	2.03
4	0.0852	15.17	0.9371	2.03
5	0.0441	14.86	--	--
6	0.0754	13.96	--	--
Average	--	14.65 ± 0.37	--	2.04 ± 0.01

[a] The overall composition was 29.72 mol% $[C_2C_1im][NTf_2]$, 29.85 mol% $[C_2C_1im][Cl]$, and 40.43 mol% H_2O

After initial determination that the water concentration in the bottom phase was lower than 5 wt.%, the bottom phase was tested using a coulometric titrator for higher accuracy. The results are shown in Table 5.17.

Table 5.17. Water concentration results for bottom phase of $[C_2C_1im][NTf_2]$:$[C_2C_1im][Cl]$:H_2O mixture[a] determined with coulometric Karl Fischer titration

Measurement	Sample (g)	Water Content (mg)	Water (wt.%)
1	0.0204	0.4421	2.17%
2	0.0178	0.3853	2.17%
3	0.0361	0.7868	2.18%
4	0.0201	0.4299	2.14%
5	0.0196	0.4270	2.18%
6	0.0272	0.5860	2.15%
7	0.0194	0.4193	2.16%
8	0.0248	0.5583	2.25%
9	0.0202	0.4390	2.17%
Average	--	--	2.17 ± 0.03%

[a] The overall composition was 29.72 mol% $[C_2C_1im][NTf_2]$, 29.85 mol% $[C_2C_1im][Cl]$, and 40.43 mol% H_2O

Ion chromatography was applied to determine the concentration of $[C_2C_1im][Cl]$ using a mixed anion standard, as mentioned earlier in the Materials section. The standard contained 29.99 ± 0.065 ppm Cl^- and was diluted with Milli-Q® purified (MQ) water to solutions of 0.5, 1, 5, 10, 15, and 20 ppm (mg/kg) shown in Table 5.18. The standard solutions were used to obtain a calibration curve to determine the unknown concentration of the Cl anion in the mixture samples.

Table 5.18. Ion chromatography standard solutions used for the Cl anion calibration curve

Desired concentration (mg/kg)	30 ppm Standard Mass (g)	MQ Water Mass (g)	Actual (mg/Kg)
0.5	0.7198 ± 0.0004	42.4746 ± 0.0116	0.4998 ± 0.0011
1	1.0053 ± 0.0004	29.1547 ± 0.0116	0.9996 ± 0.0022
5	4.9944 ± 0.0007	24.9926 ± 0.0116	4.9949 ± 0.0110
10	10.0197 ± 0.0007	20.1236 ± 0.0116	9.9687 ± 0.0219
15	14.9062 ± 0.0007	14.9390 ± 0.0116	14.9785 ± 0.0330
20	30.3045 ± 0.0007	15.1598 ± 0.0116	19.9900 ± 0.0436

Based on the concentration results of $[C_2C_1im][NTf_2]$ (top = 0.65825 g, bottom = 27.746 g) and water (top = 14.65 wt.%, bottom = 2.17 wt.%), and the measured total mass (top = 5.7030 g, bottom = 32.495 g), using a mass balance, it was estimated that the top phase and the bottom phase each had about 4 g of $[C_2C_1im][Cl]$. Therefore, the mixture samples were diluted as tabulated in Table 5.19 and Table 5.20 to maintain a concentration of Cl^- lower than 20 ppm.

Table 5.19. Water and stock quantities used for dilutions of $[C_2C_1im][NTf_2]$:$[C_2C_1im][Cl]$:H_2O solution top phase

Sample Label	Mass of Stock Used (g)	Milli-Q water (g)	Stock Solution Used
1K	1.0169 ± 0.0004	126.0366 ± 0.0116	Original Phase (1O)
1L	1.1042 ± 0.0004	70.1613 ± 0.0116	1K
1M	2.8738± 0.0007	41.5547 ± 0.0116	1L
1N	1.2212± 0.0004	25.2374 ± 0.0116	1L

Table 5.20. Water and stock quantities used for dilutions of $[C_2C_1im][NTf_2]$:$[C_2C_1im][Cl]$:H_2O solution bottom phase

Sample Label	Mass of Stock Used (g)	MQ water (g)	Stock Solution Used
2K	0.5257 ± 0.0004	11.0301 ± 0.0116	Original Phase (2O)
2L	0.4199 ± 0.0004	22.0442 ± 0.0116	2K
2M	2.0404 ± 0.0007	31.0139 ± 0.0116	2L
2N	1.0221 ± 0.0004	20.1338 ± 0.0116	2L

The concentration of chloride in samples 1M, 1N, 2M and 2N was determined with ion chromatography; the results are listed in Table 5.21.

Table 5.21. IC results for Cl^- concentration in $[C_2C_1im][NTf_2]$:$[C_2C_1im][Cl]$:H_2O mixture[a]

Sample	Top Phase (1) (mg/L)	Bottom Phase (2) (mg/L)
M	1.4436 ± 0.0030	1.8930 ± 0.0104
N	1.0608 ± 0.0146	1.4889 ± 0.0002

[a] The overall composition was 29.72 mol% $[C_2C_1im][NTf_2]$, 29.85 mol% $[C_2C_1im][Cl]$, and 40.43 mol% H_2O

Equations 5.19-5.22 were applied to determine the unknown concentration of $[C_2C_1im][Cl]$ in each phase, where C_{iL} is the concentration in mg/kg of the chloride in the *ith* phase and *L* sample, W_{wiM} is the mass of MQ water used to create the M sample of phase *i* , W_{SiM} is the mass of stock solution used to create the *M* sample of phase *i*, and $C_{i[C2C1im][Cl]}$ is the concentration of

[C_2C_1im][Cl] in phase *i*. Note that C_{iM} and C_{iN} are values determined by the ion chromatography measurements.

$$C_{iL} = C_{iM}(W_{w_{iM}} + W_{S_{iM}})/W_{S_{iM}} \quad (5.19)$$

$$C_{iK} = C_{iL}(W_{w_{iL}} + W_{S_{iL}})/W_{S_{iL}} \quad (5.20)$$

$$C_{iO} = C_{iK}(W_{w_{iK}} + W_{S_{iK}})/W_{S_{iK}} \quad (5.21)$$

$$C_{i[C2C1im][Cl]}\left(\frac{g}{g}\right) = C_{iO}\frac{1\ g}{1000\ mg} * \frac{1\ kg}{1000\ g} * \frac{1\ mol\ Cl}{35.453\ g} * \frac{1\ mol\ [C2C1im][Cl]}{mol\ Cl} * \frac{146.62\ g}{mol\ [C2C1im][Cl]} \quad (5.22)$$

Note that the sample *N* can also be used in the calculations by using the values for sample *N* instead of *M* to calculated C_{iL}. Once the values for $C_{i[C2C1im][Cl]}$ were calculated for each *M* and *N* sample, the average was calculated for each phase. The results are shown in Table 5.22.

Table 5.22. IC stock concentrations and wt.% of [C_2C_1im][Cl] in for each phase in the [C_2C_1im][NTf_2]:[C_2C_1im][Cl]:H_2O mixture[a]

Sample #	C_{iL} (mg/kg)	C_{iK} (mg/kg)	C_{iO} (mg/kg)	$C_{i[C2C1im][Cl]}$ (%)	Average $C_{i[C2C1im][Cl]}$ (%)
1M	22.318 ± 0.047	1440.4 ± 3.1	(1.7997 ± 0.0039) x 10^5	74.427 ± 0.163	75.537 ± 0.530
1N	22.983 ± 0.317	1483.4 ± 20.4	(1.8533 ± 0.0256) x 10^5	76.647 ± 1.057	
2M	30.666 ± 0.169	1640.6 ± 9.2	(3.6063 ± 0.0208) x 10^4	14.914 ± 0.028	14.951 ± 0.045
2N	30.818 ± 0.021	1648.7 ± 2.2	(3.6241 ± 0.0067) x 10^4	14.988 ± 0.086	

[a] The overall composition was 29.72 mol% [C_2C_1im][NTf_2], 29.85 mol% [C_2C_1im][Cl], and 40.43 mol% H_2O

Finally, the total mass for the top (T_{Wtop}) and bottom (T_{Wbot}) phases were calculated with Eq. 5.23 using the mass of [C_2C_1im][NTf_2] (W_{iT}) from F NMR, the [C_2C_1im][Cl] mass fraction (w_{iC}) from Ion Chromatography, the water mass fraction (w_{iH}) from Karl Fischer, and the volume V_i (where *i* indicates the ith phase). W_{iT} is the mass of NTf_2 in phase *i*.

$$T_{Wi} = \frac{C_{iT}V_iMW_T}{1-w_{iC}-w_{iH}} = \frac{W_{iT}}{1-w_{iC}-w_{iH}} \quad (5.23)$$

The results were T_{Wtop} = 6.71 ± 0.50 g and T_{Wbot} = 33.48 ± 2.50 g, which are equivalent to 16.69 ± 1.47 wt.% of the total mass is in the top phase and 83.31 ± 1.47 wt.% is in the bottom phase. These values are significantly close to those measured: 5.703 ± 0.028 g top and 32.495 ± 0.037 g bottom, and 14.93 ± 0.06 wt.% in the top and 85.07 ± 0.06 wt.% in the bottom. Therefore, the methodology was validated.

The $[C_2C_1im][NTf_2]$ mass percent in each phase was calculated in Eq. 5.24, and the mass of $[C_2C_1im][Cl]$ and water in each phase were calculated using equations 5.25-5.26 (where *i* indicates the ith phase). The results are shown in Table 5.23.

$$w_{iT} = \frac{W_{iT}}{T_{Wi}} \tag{5.24}$$

$$W_{iC} = T_{Wi} w_{iC} \tag{5.25}$$

$$W_{iH} = T_{Wi} w_{iH} \tag{5.26}$$

Table 5.23. Mass concentration in the $[C_2C_1im][NTf_2]$:$[C_2C_1im][Cl]$:H_2O mixture[a]

Species	Top Phase	Bottom Phase	Top Phase	Bottom Phase
	mass (g)	mass (g)	mass (%)	mass (%)
$[C_2C_1im][NTf_2]$	0.66 ± 0.02	27.75 ± 2.07	9.81 ± 0.79	82.88 ± 8.73
$[C_2C_1im][Cl]$	5.07 ± 0.38	5.00 ± 0.37	75.54 ± 0.53	14.95 ± 0.05
H_2O	0.98 ± 0.08	0.73 ± 0.06	14.65 ± 0.40	2.17 ± 0.03
Total	6.71 ± 0.50	33.48 ± 2.49	100.00	100.00

[a] The overall composition was 29.72 mol% $[C_2C_1im][NTf_2]$, 29.85 mol% $[C_2C_1im][Cl]$, and 40.43 mol% H_2O

The moles for each species were calculated by dividing the mass of each species by their molecular weight, and the total moles for each phase were calculated by summing the moles of each species. Mole fractions were determined by dividing each mole species by the total moles of each phase, or by Eq. 5.27 (both methods conclude the same result), and the results are listed in Table 5.24.

$$x_{iJ} = \frac{\frac{w_{ij}}{MW_J}}{\frac{w_{iT}}{MW_T}+\frac{w_{iC}}{MW_C}+\frac{w_{iH}}{MW_H}} \quad (5.27)$$

Table 5.24. Mole concentration in the $[C_2C_1im][NTf_2]$:$[C_2C_1im][Cl]$:H_2O mixture[a]

Species	Top Phase	Bottom Phase	Top Phase	Bottom Phase
	(moles)	(moles)	(mole %)	(mole %)
$[C_2C_1im][NTf_2]$	(0.17 ±0.01) x 10^{-2}	(7.091 ± 0.528) x 10^{-2}	1.85 ± 0.15	48.75 ± 2.64
$[C_2C_1im][Cl]$	(3.45 ± 0.26) x 10^{-2}	(3.414 ± 0.254) x 10^{-2}	38.08 ± 0.66	23.47 ± 1.21
H_2O	(5.45 ± 0.43) x 10^{-2}	(4.040 ± 0.306) x 10^{-2}	60.07 ± 0.69	27.78 ± 1.46
Total	(9.07 ± 0.51) x 10^{-2}	(14.544 ± 0.661) x 10^{-2}	100.0	100.00

[a] The overall composition was 29.72 mol% $[C_2C_1im][NTf_2]$, 29.85 mol% $[C_2C_1im][Cl]$, and 40.43 mol% H_2O

Finally, the partition for each species was calculated with Eq. 5.28 and are shown in Table 5.25.

$$P_{iJ} = \frac{W_{iJ}}{W_{topJ}+W_{botJ}} \quad (5.28)$$

Table 5.25. Phase partition results (in wt.% or mol%) for the $[C_2C_1im][NTf_2]$:$[C_2C_1im][Cl]$:H_2O mixture[a]

Component	$[C_2C_1im][NTf_2]$	$[C_2C_1im][Cl]$	H_2O
Top Phase	2.32 ± 0.18 %	50.30 ± 2.64 %	57.43 ± 2.69 %
Bottom Phase	97.68 ± 0.18 %	49.70 ± 2.64 %	42.57 ± 2.69 %

[a] The overall composition was 29.72 mol% $[C_2C_1im][NTf_2]$, 29.85 mol% $[C_2C_1im][Cl]$, and 40.43 mol% H_2O

The mole percent and mass percent results shown in Tables 5.23 and 5.24, clearly show the top liquid phase was water-rich and the bottom phase was rich in $[C_2C_1im][NTf_2]$. Similar to the $[C_2C_1im][NTf_2]$:$[C_2C_1im][OAc]$: H_2O system, it was expected that the bottom phase would be rich in $[C_2C_1im][NTf_2]$ and the top phase would be rich in water with a higher concentration of the hydrophilic ionic liquid. The higher water affinity of the Cl anion in comparison to that of the NTf_2 anion dictates the phase separation. In addition, the ionic liquid $[C_2C_1im][NTf_2]$ is denser than water or $[C_2C_1im][Cl]$, and therefore the $[C_2C_1im][NTf_2]$-rich phase is positioned in the bottom.

Figure 5.10 summarizes the phase concentration of the $[C_2C_1im][NTf_2]$:$[C_2C_1im][Cl]$:H_2O mixture.

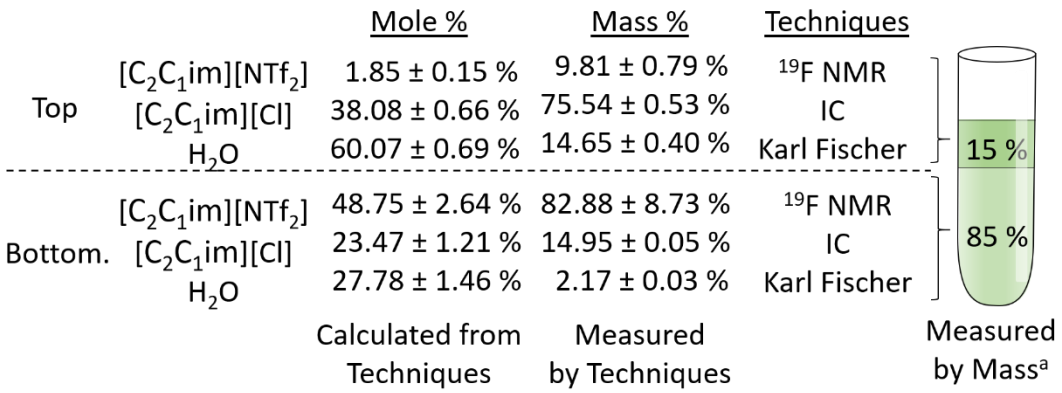

Figure 5.10. Phase concentration results for the $[C_2C_1im][NTf_2]$:$[C_2C_1im][Cl]$:H_2O mixture[b] which applied a variety of analytical techniques (NMR, IC, KF) to determine the species concentrations in each phase. This is a modified version of the original image published by Rocha et al.[67]

[a] Phase fractions are in mass percent

[b] The overall composition was 29.72 mol% $[C_2C_1im][NTf_2]$, 29.85 mol% $[C_2C_1im][Cl]$, and 40.43 mol% H_2O

5.3.3 $[C_2C_1im][OAc]$:$[C_2C_1im][Cl]$:H_2O System

The third system investigated was the 1:1 mole ratio mixture of $[C_2C_1im][Cl]$ and $[C_2C_1im][OAc]$ (Figure 5.11). The solution was initially a heterogeneous solid-liquid mixture with no water added, similar to the $[NTf_2]$:[Cl] system, as $[C_2C_1im][Cl]$ is a solid at room temperature. When the system reached 43 ± 1 mol% H_2O, the $[C_2C_1im][Cl]$ dissolved and the solution became light green in color. More water was added to the system, until the water concentration was 83.6 ± 0.1 mol%. Heat was released as the solution was mixed, and the color changed to an amber-like tint. No liquid-liquid separation was observed at room temperature. This phase behavior is consistent with the molecular dynamics simulations and is expected, as both anions are hydrophilic and have similar dimensions. Considering [OAc] and [Cl] have comparable van der Waals radii of 1.6 Å [58] and 1.75 Å,[59] respectively, it can be concluded the anions share similar charge densities and are equally miscible with water.

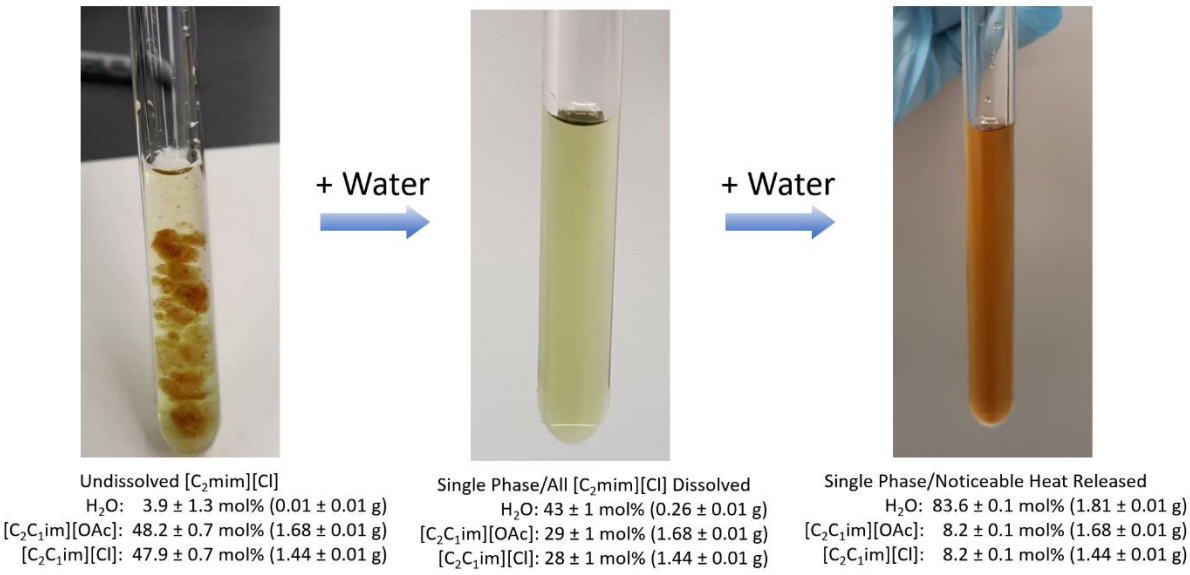

Figure 5.11. Mixtures of $[C_2C_1im][OAc]$:$[C_2C_1im][Cl]$:H_2O at 295 ± 1 K with increasing water content. This is a modified version of the original image published by Rocha et al.[67]

Previous literature has shown that a color change in imidazolium based ionic liquids with [Cl] anions is due to the thermal decomposition of the ionic liquid.[76,77] However, the present study indicates that the color change occurs at room temperature when the H_2O to $[C_2C_1im][Cl]$ ratio is increased from 1.5:1 to 10:1. The liquid structure in these mixtures was studied by Dr. Maginn's group at the University of Notre Dame using spatial distribution functions (SDFs) to possibly understand the solution color change. The SDFs showed that the location of [Cl] and [OAc] anions changed as the concentration of water increased. It is very likely that the color change observed in experiments is related to the solvation structure changes when the H_2O mol% was increased from 60 % to 83 %. The possibility of impurities reacting is also a potential cause for color change, however, most reactions are observed at higher temperatures than 298 K. A recommended future study is the evaporation of water from the 83.6 mol% water mixture to observe if the color change is reversible.

5.3.4 Effect of Temperature on Liquid-Liquid Equilibria

The mixtures were also observed at temperatures ranging from 298.15 K to 323.15 K in 5 K intervals until the liquid-liquid meniscus disappeared. The tubes were secured in a copper wire basket-like cage and submerged in a (Hart 7341 Calibration bath) silicone oil bath. The bath was calibrated with a Fluke® Standard Platinum Resistance Thermometer (S/N 1113, max deviation ± 0.025 K), and the uncertainty was determined to be 0.30 K. The samples were manually shaken at every temperature, and then allowed to stay upright within the heated bath for 2 hours before final observation. The presence of a liquid-liquid partition was monitored at every temperature. Figure 5.12 and Figure 5.13 show the temperature effects on the liquid-liquid phase equilibrium of $[C_2C_1im][NTf_2]$:$[C_2C_1im][OAc]$:H_2O (x_w = 0.54) and $[C_2C_1im][NTf_2]$:$[C_2C_1im][Cl]$:H_2O (x_w = 0.41) mixtures, respectively. It was observed that the $[C_2C_1im][NTf_2]$:$[C_2C_1im][OAc]$:H_2O system was no longer a two-phase liquid at 303.11 ± 0.30 K. Similarly, the $[C_2C_1im][NTf_2]$:$[C_2C_1im][Cl]$:H_2O system was also a single phase when increased to 323.11 ± 0.30 K.

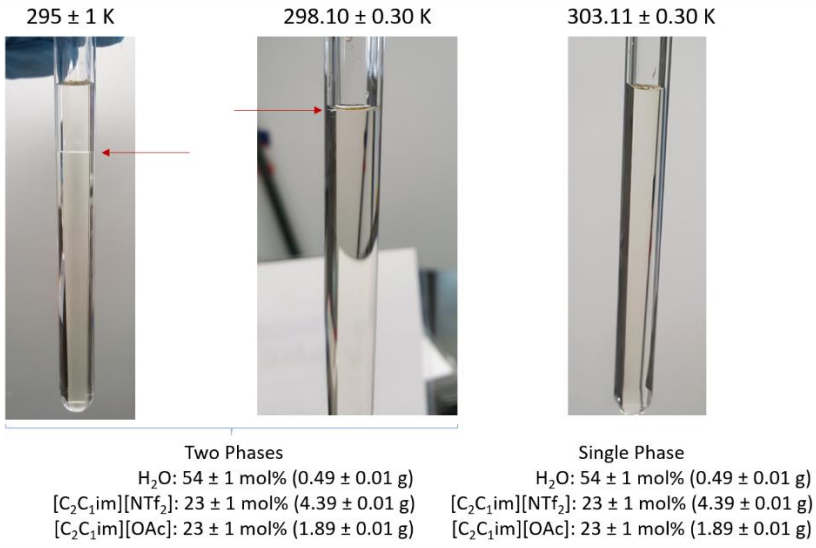

Figure 5.12. Temperature effects on the phase equilibria of $[C_2C_1im][NTf_2]$:$[C_2C_1im][OAc]$:H_2O mixture at 54 mol% H_2O

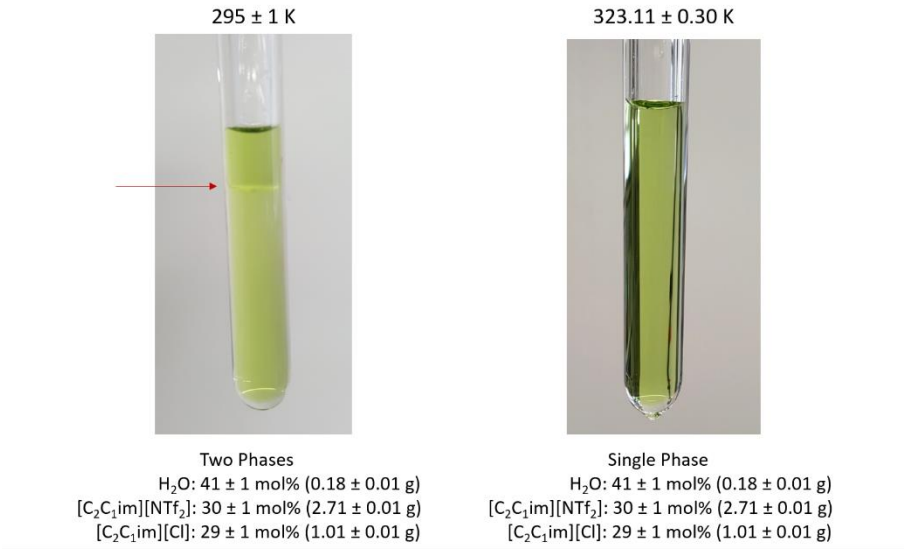

Figure 5.13. Temperature effects on the phase equilibria of $[C_2C_1im][NTf_2]$:$[C_2C_1im][Cl]$:H_2O mixture at 41 mol% H_2O

The equimolar mixtures $[C_2C_1im][NTf_2]$:$[C_2C_1im][OAc]$ and $[C_2C_1im][NTf_2]$:$[C_2C_1im][Cl]$ were created at 83 mol% H_2O, and a liquid-liquid phase separation meniscus was observed in each mixture at 295 ± 1 K. Each solution was heated, and the meniscus was still present when the temperature reached 355.13 ± 0.30 K, the results are shown in Figure 5.14 and Figure 5.15. An interesting effect occurred upon the increase of water content in the $[C_2C_1im][NTf_2]$:$[C_2C_1im][Cl]$ mixture. Figure 5.15 depicts the bottom phase became clear and the top phase turned to a yellow/amber tint. Upper critical solution temperatures (UCST) were not measured for either of these systems, as this would have required heating the solution beyond 356 K and the authors were concerned that it could cause HF by-product formation. Different masses for each species are shown in Figure 5.14 compared to Figure 5.12 because the mixture used in Figure 5.12 became contaminated and a new solution had to be made.

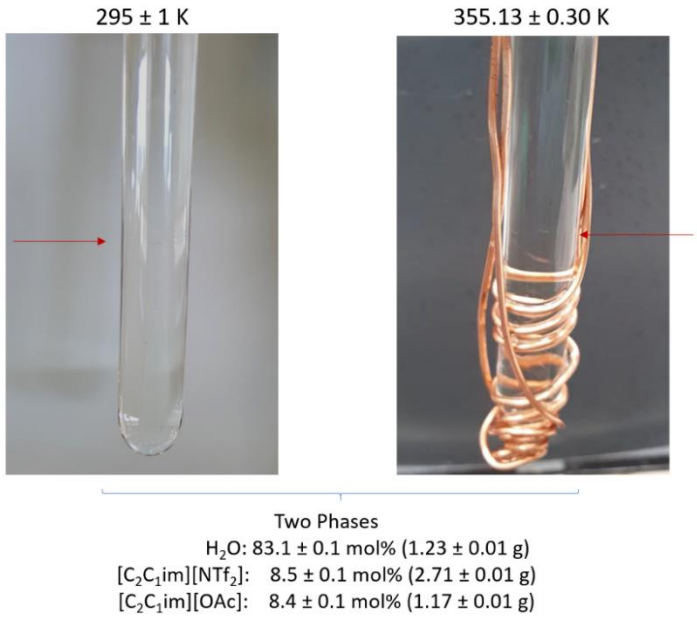

Figure 5.14. Phase equilibria of equimolar $[C_2C_1im][NTf_2]$:$[C_2C_1im][OAc]$ mixture and 83 mol% H_2O at room temperature (i.e., 295 ± 1 K) and 355 K. Red arrow indicates meniscus. Note the copper wire basket (right hand picture) was used to hold the tube with its cap in place in the oil bath.

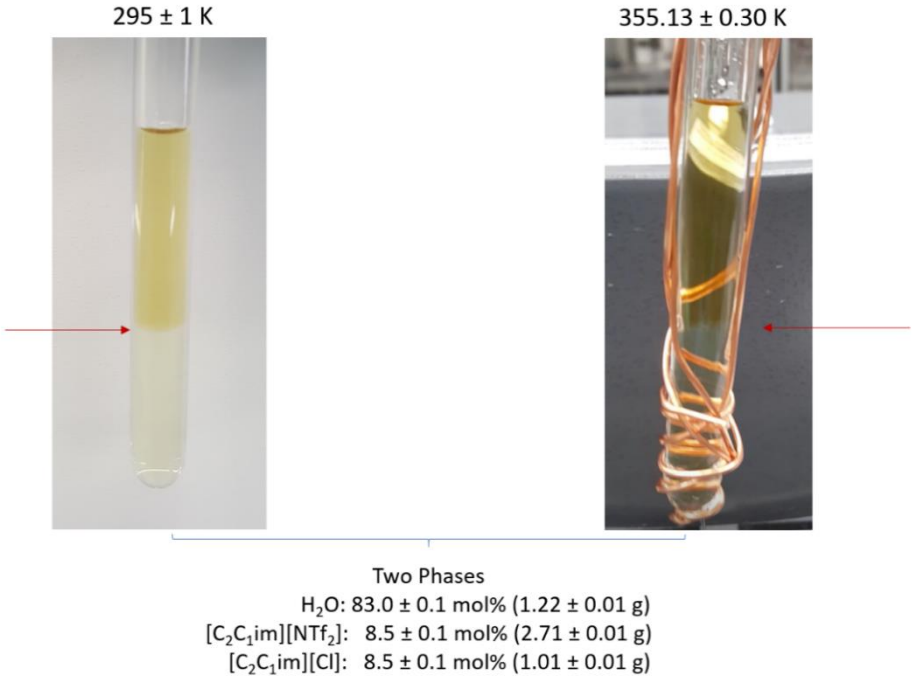

Figure 5.15. Phase equilibria of equimolar $[C_2C_1im][NTf_2]$:$[C_2C_1im][Cl]$ mixture and 83 mol% H_2O at room temperature (i.e., 295 ± 1 K) and at 355 K. Red arrow indicates meniscus. Note the copper wire basket (right hand picture) was used to hold the tube with its cap in place in the oil bath.

5.4 Conclusion

Water addition to equimolar imidazolium-based ionic liquids with anions of differing hydrophilicity can induce a liquid-liquid phase separation at room temperature. This study validated the simulation predictions performed by the Maginn group at the University of Notre Dame. Mixtures of $[C_2C_1im][NTf_2]$, $[C_2C_1im][OAc]$, and water were observed to phase separate at 54 ± 1 mol% H_2O and ^1H NMR analysis showed the top phase was rich in $[C_2C_1im][OAc]$ and water and the bottom phase was rich in $[C_2C_1im][NTf_2]$. The $[C_2C_1im][NTf_2]$:$[C_2C_1im][Cl]$:H_2O mixture was observed to reach liquid-liquid equilibrium at 39 ± 3 mol% H_2O, and using ^{19}F NMR, Karl Fischer, and ion chromatography, the top phase was determined to be rich in $[C_2C_1im][Cl]$ and water, and the bottom phase was determined to be rich in $[C_2C_1im][NTf_2]$. The third system investigated was an equimolar mixture of two hydrophilic ionic liquids ($[C_2C_1im][OAc]$ + $[C_2C_1im][Cl]$). The mixture remained single-phase at all water concentrations, as expected due to the affinity of both anions to water.

The temperature effect was also observed in the IL-IL-water mixtures. It was observed that the $[C_2C_1im][NTf_2]$:$[C_2C_1im][OAc]$:H_2O mixture at 54 ± 1 mol% H_2O was a single-phase liquid at 303.11 ± 0.30 K, but remained a two-phase liquid at 83.1 ± 0.1 mol% H_2O at 355.13 ± 0.30 K. The $[C_2C_1im][NTf_2]$:$[C_2C_1im][Cl]$:H_2O mixture was a single-phase liquid at 41 ± 1 mol% H_2O and 323.11± 0.30 K, and was two-phase at 83.0 ± 0.1 mol% H_2O at 355.13 ± 0.30 K.

Chapter 6: Conclusion and Recommendation

6.1 Background

This chapter summarizes conclusions from previous chapters and provides recommendations for future studies on the phase equilibria of water and ionic liquids.

6.2 Water Sorption Using the Gravimetric Technique

The use of gravimetric microbalances for the solubility measurement of gases and vapors in ionic liquids has been proven to be a reliable and accurate technique. A force balance and a correction for the buoyancy effects was successfully applied to improve the accuracy of the results. As mentioned in Chapter 2, the drag force effect on the microbalance results were also incorporated into the correction factor. However, the effect which drag force has on the system may be of interest to some researchers. Future studies could involve expanding the drag force term, F_D, in Eq. 2.5 to include aerodynamic or viscous drag as a function of Reynolds number.

6.3 Water Vapor Solubility Results

The water solubility measurements in $[C_2C_1im][BF_4]$ agreed with published data and provided confidence that the IGAsorp method was reliable for measuring water sorption in ionic liquids. The results also showed that for the measured conditions, the water solubility from highest to lowest was: $[C_2C_1im][OAc]$ > $[C_4C_1im][OAc]$ > $[C_4C_1im][Cl]$ > $[C_2C_1im][TFES]$ > $[C_2C_1im][BF_4]$.

It is recommended that the solubility of water in $[C_2C_1im][TFES]$ be measured at higher humidity values (> 25% RH) The current range (0 – 25 % RH) only reached a solubility of about 30 mol% water. Higher RH and x_w values would provide a better overall view of the isotherms and whether they become nonlinear. or remain similar to the isotherms for $[C_2C_1im][BF_4]$. In addition, it would also be of interest to measure higher humidity values for $[C_2C_1im][OAc]$, $[C_4C_1im][OAc]$,

and [C_4C_1im][Cl] to observe if the solubility (P vs. x_w) reaches a plateau as x_w approaches 1. Overall, it is recommended that all ILs be measured at humidity values close to 40 % RH (ambient humidity), as ILs are most likely to be exposed to this condition in practice.

6.4 Diffusion and Enthalpy of Water Vapor Sorption in Ionic Liquids

Water-IL binary diffusion coefficients were determined using a 1D diffusion equation on mass time-dependent data, which was measured using a spherical-shaped container. The diffusion results for [C_2C_1im][BF_4] were unexpected as the diffusion coefficient decreased as the % RH increased and as the mixture viscosity decreased. On the other hand, the results for [C_2C_1im][TFES], [C_2C_1im][OAc], [C_4C_1im][OAc], and [C_4C_1im][Cl] were as expected, where the diffusivity increased as % RH increased and mixture viscosity decreased.

The diffusing radii and enthalpy of absorption were calculated to explain the differences in diffusion behavior for the ionic liquids. The results for the diffusing radii suggested that the species diffusing in the [C_2C_1im][OAc], [C_4C_1im][OAc], and [C_4C_1im][Cl] systems were much smaller than the species diffusing in [C_2C_1im][BF_4]. In addition, results in literature have indicated that water aggregates form in imidazolium-based [BF_4] systems. Therefore, this leads to the hypothesis that while only a few water molecules may be hydrogen bonding with the [OAc] and [Cl] anions, larger water/BF_4^- networks are forming in the [C_2C_1im][BF_4] system, which continue to increase in size as water concentration increases.

The enthalpy of absorption analysis indicated that increasing water concentration caused the mixture interactions to approach values similar to ΔH_{vap} for water at 298 K, which represents water-water hydrogen bonding interactions. This makes sense as a higher concentration in water indicates a higher probability of water-water bonding. Interestingly, it was observed that at low x_w the system interactions in [C_2C_1im][BF_4] and [C_2C_1im][TFES], were weaker than the water-water

hydrogen bonding interactions (ΔH_{vap}), whereas the system interactions in $[C_2C_1im][OAc]$, $[C_4C_1im][OAc]$, and $[C_4C_1im][Cl]$ were larger than ΔH_{vap}. A comparison of the water-IL systems at similar viscosities, suggested that higher heats of absorption indicated a lower diffusion coefficient. Therefore, this indicates that, in addition to viscosity, molecular interactions such as hydrogen bonding play an important role in the diffusivity of water in ionic liquids.

There are several opportunities for future work regarding the diffusion and enthalpy analyses. A full derivation for the 2D diffusion coefficient (with spherical coordinates) is encouraged to remove any approximation limitations which may occur when using the 1D diffusion equation on data measured with the spherical container. It would be of interest to compare the results of this new fit to those calculated by the 1D approximation, the COMSOL Multiphysics® simulation, and to the results obtained using the 1D equation on the flat cylinder container. It also recommended that higher RH values be measured for all ILs, particularly values near 40 % RH, and to observe the kinetic behavior at these conditions. This would provide valuable information on the expected mass percent absorbed as a function of time.

Solubility measurements at higher % RH conditions are recommended for the $[C_2C_1im][TFES]$ system; which would show if the diffusion of water in $[C_2C_1im][TFES]$ continues to increase as RH increases at higher water concentrations. In addition, the mixture viscosity for water and $[C_2C_1im][TFES]$ should be measured so that the diffusing radius can be calculated and effect of heat of absorption on the diffusion coefficient can be analyzed.

As mentioned in Chapter 4, the heat of absorption of water in the IL systems was calculated using the Clausius-Clapeyron equation and using the pressure determined by the NRTL equation. A calorimetry study on absorption of water in ILs would make it possible to compare the measured and calculated ΔH_{abs} and to evaluate the accuracy of the approximation.

Finally, it is recommended that molecular simulations be performed for the measured water-IL systems as a function of increasing RH. This would provide insight into the structure of water in ionic liquids as a function of water concentration and explain how water forms clusters with various anion types.

6.5 Water-Induced Liquid-Liquid Separation of Imidazolium-based IL mixtures

Water addition to equimolar imidazolium-based ionic liquids with anions of differing hydrophilicity was shown to induce a liquid-liquid phase separation at room temperature. The results validated the simulation prediction performed by the Maginn group at the University of Notre Dame. The $[C_2C_1im][NTf_2]$:$[C_2C_1im][OAc]$ mixture was observed to phase separate with the addition of water, and the analytical techniques showed that the top phase was rich in water and the hydrophilic ionic liquid, $[C_2C_1im][OAc]$, while the bottom phase was rich in $[C_2C_1im][NTf_2]$, the hydrophobic IL. Similarly, the $[C_2C_1im][NTf_2]$:$[C_2C_1im][Cl]$ mixture phase separated with the addition of water, and it was determined that the top phase was rich in water and the hydrophilic IL, $[C_2C_1im][Cl]$, and that the bottom liquid phase was rich in $[C_2C_1im][NTf_2]$.

The third system, $[C_2C_1im][OAc]$:$[C_2C_1im][Cl]$ did not phase separate with the addition of water due to the affinity of water with both [OAc] and [Cl] anions. However, an interesting effect occurred when water was added; the mixture changed color from a green-tinted solution (due to the presence of $[C_2C_1im][Cl]$) to an amber color. It is hypothesized that the color change is due to a change in the solvation structure as the water concentration increases. A future study on this system could dry the mixture and observe if the color returns to green when the water concentration decreases. This would help understand if the color change is truly due to a physical effect. It would also be of interest to expand the phase equilibria studies on mixtures of IL-IL-water mixtures at

different IL concentrations. This could result in the creation of ternary phase diagrams to estimate the behavior of such functionalized mixtures.

References

(1) Lei, Z.; Chen, B.; Koo, Y.-M.; MacFarlane, D. R. Introduction: Ionic Liquids. *Chem. Rev.* **2017**, *117*, 6633–6635.

(2) Wong, D. S. H.; Chen, J. P.; Chang, J. M.; Chou, C. H. Phase Equilibria of Water and Ionic Liquids [Emim][PF_6] and [Bmim][PF_6]. *Fluid Phase Equilib.* **2002**, *194–197*, 1089–1095.

(3) Cao, Y.; Chen, Y.; Sun, X.; Zhang, Z.; Mu, T. Water Sorption in Ionic Liquids: Kinetics, Mechanisms and Hydrophilicity. *Phys. Chem. Chem. Phys.* **2012**, *14*, 12252–12262.

(4) Chen, Y.; Cao, Y.; Yan, C.; Zhang, Y.; Mu, T. The Dynamic Process of Atmospheric Water Sorption in [BMIM][Ac]: Quantifying Bulk versus Surface Sorption and Utilizing Atmospheric Water as a Structure Probe. *J. Phys. Chem. B* **2014**, *118*, 6896–6907.

(5) Zhao, H.; Xia, S.; Ma, P. Review Use of Ionic Liquids as “green” Solvents for Extractions. *J. Chem. Technol. Biotechnol. J Chem Technol Biotechnol* **2005**, *80*, 1089–1096.

(6) Welton, T. Room-Temperature Ionic Liquids. Solvents for Synthesis and Catalysis. *Chem. Rev.* **1999**, *99*, 2071–2084.

(7) MacFarlane, D. R.; Forsyth, M.; Howlett, P. C.; Pringle, J. M.; Sun, J.; Annat, G.; Neil, W.; Izgorodina, E. I. Ionic Liquids in Electrochemical Devices and Processes: Managing Interfacial Electrochemistry. *Acc. Chem. Res.* **2007**, *40*, 1165–1173.

(8) Zhao, W.; He, G.; Zhang, L.; Ju, J.; Dou, H.; Nie, F.; Li, C.; Liu, H. Effect of Water in Ionic Liquid on the Separation Performance of Supported Ionic Liquid Membrane for CO2/N2. *J. Memb. Sci.* **2010**, *350*, 279–285.

(9) Maiti, A.; Kumar, A.; Rogers, R. D. Water-Clustering in Hygroscopic Ionic Liquids - An

Implicit Solvent Analysis. *Phys. Chem. Chem. Phys.* **2012**, *14*, 5139–5146.

(10) Welton, T. Ionic Liquids in Catalysis. *Coord. Chem. Rev.* **2004**, *248*, 2459–2477.

(11) Holbrey, J. D.; Reichert, M. M.; Nieuwenhuyzen, M.; Sheppard, O.; Hardacre, C.; Rogers, R. D. Liquid Clathrate Formation in Ionic Liquid-Aromatic Mixtures. *Chem. Commun.* **2003**, *3*, 476–477.

(12) Takamuku, T.; Kyoshoin, Y.; Shimomura, T.; Kittaka, S.; Yamaguchi, T. Effect of Water on Structure of Hydrophilic Imidazolium-Based Ionic Liquid. *J. Phys. Chem. B* **2009**, *113*, 10817–10824.

(13) Cao, Y.; Chen, Y.; Lu, L.; Xue, Z.; Mu, T. Water Sorption in Functionalized Ionic Liquids: Kinetics and Intermolecular Interactions. *Ind. Eng. Chem. Res.* **2013**, *52*, 2073–2083.

(14) Tran, C. D.; De Paoli Lacerda, S. H.; Oliveira, D. Absorption of Water by Room-Temperature Ionic Liquids: Effect of Anions on Concentration and State of Water. *Appl. Spectrosc.* **2003**, *57*, 152–157.

(15) Broderick, A.; Khalifa, Y.; Shiflett, M. B.; Newberg, J. T. Water at the Ionic Liquid-Gas Interface Examined by Ambient Pressure X-Ray Photoelectron Spectroscopy. *J. Phys. Chem. C* **2017**, *121*, 7337–7343.

(16) Di Francesco, F.; Calisi, N.; Creatini, M.; Melai, B.; Salvo, P.; Chiappe, C. Water Sorption by Anhydrous Ionic Liquids. *Green Chem.* **2011**, *13*, 1712–1717.

(17) Penner, E. A.; Schmidt, S. J. Comparison between Moisture Sorption Isotherms Obtained Using the New Vapor Sorption Analyzer and Those Obtained Using the Standard Saturated Salt Slurry Method. *J. Food Meas. Charact.* **2013**, *7*, 185–193.

(18) Kohno, Y.; Ohno, H. Ionic Liquid/Water Mixtures: From Hostility to Conciliation. *Chem.*

Commun. **2012**, *48*, 7119–7130.

(19) Kohno, Y.; Ohno, H. Temperature-Responsive Ionic Liquid/Water Interfaces: Relation between Hydrophilicity of Ions and Dynamic Phase Change. *Phys. Chem. Chem. Phys.* **2012**, *14*, 5063–5070.

(20) Shimojo, K.; Nakashima, K.; Kamiya, N.; Goto, M. Crown Ether-Mediated Extraction and Functional Conversion of Cytochrome c in Ionic Liquids. *Biomacromolecules* **2006**, *7*, 2–5.

(21) Niedermeyer, H.; Hallett, J. P.; Villar-Garcia, I. J.; Hunt, P. A.; Welton, T. Mixtures of Ionic Liquids. *Chem. Soc. Rev.* **2012**, *41*, 7780–7802.

(22) Arce, A.; Earle, M. J.; Katdare, S. P.; Rodríguez, H.; Seddon, K. R. Mutually Immiscible Ionic Liquids. *Chem. Commun.* **2006**, *2*, 2548–2550.

(23) Anthony, J. L.; Maginn, E. J.; Brennecke, J. F. Solution Thermodynamics of Imidazolium-Based Ionic Liquids and Water. *J. Phys. Chem. B* **2001**, *105*, 10942–10949.

(24) Anthony, J. L.; Maginn, E. J.; Brennecke, J. F. Solubilities and Thermodynamic Properties of Gases in the Ionic Liquid 1-n-Butyl-3-Methylimidazolium Hexafluorophosphate. *J. Phys. Chem. B* **2002**, *106*, 7315–7320.

(25) Minnick, D. L.; Turnaoglu, T.; Rocha, M. A.; Shiflett, M. B. Review Article: Gas and Vapor Sorption Measurements Using Electronic Beam Balances. *J. Vac. Sci. Technol. A* **2018**, *36*, 050801-1–050801-14.

(26) Shiflett, M. B.; Yokozeki, A. Phase Behaviour of Gases in Ionic Liquids. In *Ionic Liquids Uncoiled: Critical Expert Overviews*; John Wiley & Sons, Inc.: Hoboken, NJ, USA, 2012; pp 349–386.

(27) Cadena, C.; Anthony, J. L.; Shah, J. K.; Morrow, T. I.; Brennecke, J. F.; Maginn, E. J.

Why Is CO2 so Soluble in Imidazolium-Based Ionic Liquids? *J. Am. Chem. Soc.* **2004**, *126*, 5300–5308.

(28) Lei, Z. G.; Dai, C. N.; Chen, B. H. Gas Solubility in Ionic Liquids. *Chem. Rev.* **2014**, *114*, 1289–1326.

(29) Wang, J.; Trinkle, D.; Derbin, G.; Martin, K.; Sharif, S.; Timmins, P.; Desai, D.; Desa, D. Moisture Adsorption and Desorption Properties of Colloidal Silicon Dioxide and Its Impact on Layer Adhesion of a Bilayer Tablet Formulation. *J. Excipients Food Chem.* **2014**, *5*, 21–31.

(30) Tugui, C.; Vlad, S.; Iacob, M.; Varganici, C. D.; Pricop, L.; Cazacu, M. Interpenetrating Poly(Urethane-Urea)– Polydimethylsiloxane Networks Designed as Active Elements in Electromechanical Transducers. *Polym. Chem* **2016**, *7*.

(31) Cazacu, M.; Ignat, M.; Racles, C.; Cristea, M.; Musteata, V.; Ovezea, D.; Lipcinski, D. Well-Defined Silicone–titania Composites with Good Performances in Actuation and Energy Harvesting. *J. Compos. Mater.* **2014**, *48*, 1533–1545.

(32) Bele, A.; Stiubianu, G.; Varganici, C. D.; Ignat, M.; Cazacu, M. Silicone Dielectric Elastomers Based on Radical Crosslinked High Molecular Weight Polydimethylsiloxane Co-Filled with Silica and Barium Titanate. *J. Mater. Sci.* **2015**, *50*, 6822–6832.

(33) Pásztory, Z.; Horváth, T.; Glass, S. V.; Zelinka, S. L. [Technical Note] Thermal Insulation System Made of Wood and Paper for Use in Residential Construction. *For. Prod. J.* **2015**, *65*, 352–357.

(34) Boardman, C.; Glass, S. V. Moisture Transfer through the Membrane of a Cross-Flow Energy Recovery Ventilator: Measurement and Simple Data-Driven Modeling. *J. Build. Phys.* **2015**, *38*, 389–418.

(35) Dahi, A.; Fatyeyeva, K.; Chappey, C.; Langevin, D.; Rogalsky, S. P.; Tarasyuk, O. P.; Marais, S. Water Sorption Properties of Room-Temperature Ionic Liquids over the Whole Range of Water Activity and Molecular States of Water in These Media. *RSC Adv.* **2015**, *5*, 76927–76938.

(36) Dahi, A.; Fatyeyeva, K.; Langevin, D.; Chappey, C.; Rogalsky, S. P.; Tarasyuk, O. P.; Benamor, A.; Marais, S. Supported Ionic Liquid Membranes for Water and Volatile Organic Compounds Separation: Sorption and Permeation Properties. *J. Memb. Sci.* **2014**, *458*, 164–178.

(37) Fatyeyeva, K.; Rogalsky, S.; Tarasyuk, O.; Chappey, C.; Marais, S. Vapour Sorption and Permeation Behaviour of Supported Ionic Liquid Membranes: Application for Organic Solvent/Water Separation. *React. Funct. Polym.* **2018**, *130*, 16–28.

(38) Lemmon, E. W.; Huber, M. L.; Mclinden, M. O. REFPROP 9.1. *NIST standard reference database*. 2013.

(39) Wagner, W.; Pruß, A. The IAPWS Formulation 1995 for the Thermodynamic Properties of Ordinary Water Substance for General and Scientific Use. *J. Phys. Chem. Ref. Data* **2002**, *31*, 387–535.

(40) Finotello, A.; Bara, J. E.; Camper, D.; Noble, R. D. Room-Temperature Ionic Liquids: Temperature Dependence of Gas Solubility Selectivity. *Ind. Eng. Chem. Res.* **2008**, *47*, 3453–3459.

(41) Anderson, J. L.; Dixon, J. K.; Brennecke, J. F. Solubility of CO2, CH4, C2H6, C2H4, O2, and N2 in 1-Hexyl-3-Methylpyridinium Bis(Trifluoromethylsulfonyl)Imide: Comparison to Other Ionic Liquids. *Acc. Chem. Res.* **2007**, *40*, 1208–1216.

(42) Shirota, H.; Mandai, T.; Fukazawa, H.; Kato, T. Comparison between Dicationic and

Monocationic Ionic Liquids: Liquid Density, Thermal Properties, Surface Tension, and Shear Viscosity. *J. Chem. Eng. Data* **2011**, *56*, 36.

(43) Larriba, M.; Navarro, P.; Beigbeder, J. B.; García, J.; Rodríguez, F. Mixing and Decomposition Behavior of {[4bmpy][Tf2N] + [Emim][EtSO4]} and {[4bmpy][Tf2N] + [Emim][TFES]} Ionic Liquid Mixtures. *J. Chem. Thermodyn.* **2015**, *82*, 58–75.

(44) Santos, E.; Albo, J.; Irabien, A. Acetate Based Supported Ionic Liquid Membranes (SILMs) for CO2 Separation: Influence of the Temperature. *J. Memb. Sci.* **2014**, *452*, 277–283.

(45) Awad, W. H.; Gilman, J. W.; Nyden, M.; Harris, R. H.; Sutto, T. E.; Callahan, J.; Trulove, P. C.; Delong, H. C.; Fox, D. M. Thermal Degradation Studies of Alkyl-Imidazolium Salts and Their Application in Nanocomposites. *Thermochim. Acta* **2004**, *409*, 3–11.

(46) Seddon, K. R.; Stark, A.; Torres, M.-J. Influence of Chloride, Water, and Organic Solvents on the Physical Properties of Ionic Liquids*. *Pure Appl. Chem* **2000**, *72*, 2275–2287.

(47) Zhao, J.; Jiang, X.-C.; Li, C.-X.; Wang, Z.-H. Vapor Pressure Measurement for Binary and Ternary Systems Containing a Phosphoric Ionic Liquid. *Fluid Phase Equilib.* **2006**, *247*, 190–198.

(48) Wang, J.-F.; Li, C.-X.; Wang, Z.-H.; Li, Z.-J.; Jiang, Y.-B. Vapor Pressure Measurement for Water, Methanol, Ethanol, and Their Binary Mixtures in the Presence of an Ionic Liquid 1-Ethyl-3-Methylimidazolium Dimethylphosphate. *Fluid Phase Equilib.* **2007**, *255*, 186–192.

(49) Shiflett, M. B.; Harmer, M. A.; Junk, C. P.; Yokozeki, A. Solubility and Diffusivity of Difluoromethane in Room-Temperature Ionic Liquids. *J. Chem. Eng. Data* **2006**, *51*, 483–

495.

(50) Shiflett, M. B.; Yokozeki, A. Solubility and Diffusivity of Hydrofluorocarbons in Room-Temperature Ionic Liquids. *AIChE J.* **2006**, *52*, 1205–1219.

(51) Belvèze, L. S. Modeling and Measurement of Thermodynamic Properties of Ionic Liquids, 2004.

(52) Yang, Q.; Yu, K.; Xing, H.; Su, B.; Bao, Z.; Yang, Y.; Ren, Q. The Effect of Molecular Solvents on the Viscosity, Conductivity and Ionicity of Mixtures Containing Chloride Anion-Based Ionic Liquid. *J. Ind. Eng. Chem.* **2013**, *19*, 1708–1714.

(53) Ries, L. A. S.; do Amaral, F. A.; Matos, K.; Martini, E. M. A.; de Souza, M. O.; de Souza, R. F. Evidence of Change in the Molecular Organization of 1-n-Butyl-3-Methylimidazolium Tetrafluoroborate Ionic Liquid Solutions with the Addition of Water. *Polyhedron* **2008**, *27*, 3287–3293.

(54) Zhang, S.; Li, X.; Chen, H.; Wang, J.; Zhang, J.; Zhang, M. Determination of Physical Properties for the Binary System of 1-Ethyl-3-Methylimidazolium Tetrafluoroborate + H_2O. *J. Chem. Eng. Data* **2004**, *49*, 760–764.

(55) Stevanovic, S.; Podgoršek, A.; Pádua, A. A. H.; Costa Gomes, M. F. Effect of Water on the Carbon Dioxide Absorption by 1-Alkyl-3-Methylimidazolium Acetate Ionic Liquids. *J. Phys. Chem. B* **2012**, *116*, 14416–14425.

(56) Yang, Q.; Yu, K.; Xing, H.; Su, B.; Bao, Z.; Yang, Y.; Ren, Q. The Effect of Molecular Solvents on the Viscosity, Conductivity and Ionicity of Mixtures Containing Chloride Anion-Based Ionic Liquid. *J. Ind. Eng. Chem.* **2013**, *19*, 1708–1714.

(57) D'Arrigo, J. S. Screening of Membrane Surface Charges by Divalent Cations: An Atomic Representation. *Am. J. Physiol.* **1978**, *235*, C109–C117.

(58) Lovell, C. S.; Walker, A.; Damion, R. A.; Radhi, A.; Tanner, S. F.; Budtova, T.; Ries, M. E. Influence of Cellulose on Ion Diffusivity in 1-Ethyl-3-Methyl-Imidazolium Acetate Cellulose Solutions. *Biomacromolecules* **2010**, *11*, 2927–2935.

(59) Bondi, A. Van Der Waals Volumes and Radii. *J. Phys. Chem.* **1964**, *68*, 441–451.

(60) Wasserscheid, P.; Welton, T. *Ionic Liquids in Synthesis: Second Edition*; Wiley-VCH, 2008; Vol. 1.

(61) Reid, J. E. S. J.; Walker, A. J.; Shimizu, S. Residual Water in Ionic Liquids: Clustered or Dissociated? *Phys. Chem. Chem. Phys.* **2015**, *17*, 14710–14718.

(62) Chen, Y.; Sun, X.; Yan, C.; Cao, Y.; Mu, T. The Dynamic Process of Atmospheric Water Sorption in [EMIM][Ac] and Mixtures of [EMIM][Ac] with Biopolymers and CO2capture in These Systems. *J. Phys. Chem. B* **2014**, *118*, 11523–11536.

(63) Hall, C. A.; Le, K. A.; Rudaz, C.; Radhi, A.; Lovell, C. S.; Damion, R. A.; Budtova, T.; Ries, M. E. Macroscopic and Microscopic Study of 1-Ethyl-3-Methyl-Imidazolium Acetate-Water Mixtures. *J. Phys. Chem. B* **2012**, *116*, 12810–12818.

(64) Haywood, R. *Thermodynamic Tables in SI (Metric) Units*; Cambridge University Press: London, 1972.

(65) Yasaka, Y.; Wakai, C.; Matubayasi, N.; Nakahara, M. Rotational Dynamics of Water and Benzene Controlled by Anion Field in Ionic Liquids: 1-Butyl-3-Methylimidazolium Chloride and Hexafluorophosphate. *J. Chem. Phys.* **2007**, *127*, 214509.

(66) Ueno, M.; Ueyama, S.; Hashimoto, S.; Tsuchihashi, N.; Ibuki, K. Pressure and Temperature Effects on the Molecular Rotation in Acetonitrile-Water Mixtures. *J. Solution Chem.* **2004**, *33*, 827–846.

(67) Rocha, M. A.; Zhang, Y.; Maginn, E. J.; Shiflett, M. B. Simulation and Measurement of

Water-Induced Liquid-Liquid Phase Separation of Imidazolium Ionic Liquid Mixtures. *J. Chem. Phys.* **2018**, *149*, 164503.

(68) Appetecchi, G. B.; Montanino, M.; Carewska, M.; Moreno, M.; Alessandrini, F.; Passerini, S. Chemical–physical Properties of Bis(Perfluoroalkylsulfonyl)Imide-Based Ionic Liquids. *Electrochim. Acta* **2011**, *56*, 1300–1307.

(69) Berthod, A.; Ruiz-Ángel, M. J.; Carda-Broch, S. Ionic Liquids in Separation Techniques. *J. Chromatogr. A* **2008**, *1184*, 6–18.

(70) Castro, M. C.; Arce, A.; Soto, A.; Rodríguez, H. Liquid-Liquid Equilibria of Mutually Immiscible Ionic Liquids with a Common Anion of Basic Character. *J. Chem. Thermodyn.* **2016**, *102*, 12–21.

(71) Le, K. A.; Sescousse, R.; Budtova, T. Influence of Water on Cellulose-EMIMAc Solution Properties: A Viscometric Study. *Cellulose* **2012**, *19*, 45–54.

(72) Troshenkova, S. V.; Sashina, E. S.; Novoselov, N. P.; Arndt, K.-F.; Jankowsky, S. Structure of Ionic Liquids on the Basis of Imidazole and Their Mixtures with Water. *Russ. J. Gen. Chem.*, **2010**, *80*, 1070–3632.

(73) Henderson, T. J. Quantitative NMR Spectroscopy Using Coaxial Inserts Containing a Reference Standard: Purity Determinations for Military Nerve Agents. *Anal. Chem.* **2002**, *74*, 191–198.

(74) Weast, R. *CRC Handbook of Chemistry and Physics*, 53rd ed.; Cleveland, Ohio: Chemical Rubber, 1972.

(75) Sanchez, E. *Processing and Analysis in Mnova 12. Focus on Requirements for QNMR*; 2018.

(76) Jiang, T.; Chollier Brym, M. J. J.; Dubé, G.; Lasia, A.; Brisard, G. M. M.

Electrodeposition of Aluminium from Ionic Liquids: Part I—electrodeposition and Surface Morphology of Aluminium from Aluminium Chloride (AlCl3)–1-Ethyl-3-Methylimidazolium Chloride ([EMIm]Cl) Ionic Liquids. *Surf. Coatings Technol.* **2006**, *201*, 1–9.

(77) Carda–Broch, S.; Berthod, A.; Armstrong, D. W.; Carda-Broch, S.; Berthod, A.; Armstrong, D. W. Solvent Properties of the 1-Butyl-3-Methylimidazolium Hexafluorophosphate Ionic Liquid. *Anal. Bioanal. Chem.* **2003**, *375*, 191–199.

(78) Shiflett, M. B.; Yokozeki, A. Liquid-Liquid Equilibria in Binary Mixtures of 1,3-Propanediol + Ionic Liquids [Bmim][PF 6], [Bmim][BF 4], and [Emim][BF 4]. *J. Chem. Eng. Data* **2007**, *52*, 1302–1306.

(79) Larriba, M.; García, S.; García, J.; Torrecilla, J. S.; Rodríguez, F. Thermophysical Properties of 1-Ethyl-3-Methylimidazolium 1,1,2,2-Tetrafluoroethanesulfonate and 1-Ethyl-3-Methylimidazolium Ethylsulfate Ionic Liquids as a Function of Temperature. *J. Chem. Eng. Data* **2011**, *56*, 3589–3597.

(80) Freire, M. G.; Rita, A.; Teles, R.; Rocha, M. A. A.; Schr€, B.; Neves, C. M. S. S.; Carvalho, P. J.; Evtuguin, D. V; Santos, L. M. N. B. F.; Ao, J.; et al. Thermophysical Characterization of Ionic Liquids Able To Dissolve Biomass. *J. Chem. Eng. Data* **2011**, *56*, 46.

(81) Safarov, J.; Geppert-Rybczy Nska, M.; Kul, I.; Hassel, E. Thermophysical Properties of 1-Butyl-3-Methylimidazolium Acetate over a Wide Range of Temperatures and Pressures. *Fluid Phase Equilib.* **2014**, *383*, 144–155.

(82) Li, H.; Zhao, G.; Liu, F.; Zhang, S. Physicochemical Characterization of MFm--Based Ammonium Ionic Liquids. *J. Chem. Eng. Data* **2013**, *58*, 1505–1515.

(83) Lu, Y.; Ma, W.; Hu, R.; Dai, X.; Pan, Y. Ionic Liquid-Based Microwave-Assisted Extraction of Phenolic Alkaloids from the Medicinal Plant Nelumbo Nucifera Gaertn. *J. Chromatogr. A* **2008**, *1208*, 42–46.

(84) Huddleston, J. G.; Visser, A. E.; Reichert, W. M.; Willauer, H. D.; Broker, G. A.; Rogers, R. D. Characterization and Comparison of Hydrophilic and Hydrophobic Room Temperature Ionic Liquids Incorporating the Imidazolium Cation. *Green Chem.* **2001**, *3*, 156–164.

(85) Kumar, B.; Singh, T.; Rao, K. S.; Pal, A.; Kumar, A. Thermodynamic and Spectroscopic Studies on Binary Mixtures of Imidazolium Ionic Liquids in Ethylene Glycol. *J. Chem. Thermodyn.* **2012**, *44*, 121–127.

(86) Kavitha, T.; Vasantha, T.; Venkatesu, P.; Rama Devi, R. S. S.; Hofman, T. Thermophysical Properties for the Mixed Solvents of N-Methyl-2-Pyrrolidone with Some of the Imidazolium-Based Ionic Liquids. *J. Mol. Liq.* **2014**, *198*, 11–20.

(87) He, R. H.; Long, B. W.; Lu, Y. Z.; Meng, H.; Li, C. X. Solubility of Hydrogen Chloride in Three 1-Alkyl-3-Methylimidazolium Chloride Ionic Liquids in the Pressure Range (0 to 100) KPa and Temperature Range (298.15 to 363.15) K. *J. Chem. Eng. Data* **2012**, *57*, 2936–2941.

Appendix

Appendix A: IGAsorp and Vapor Liquid Equilibrium Data for Water-IL systems

A.1 Experimental Methodology Details

The Pyrex® spherical-shaped containers used in this study were each cleaned twice with methanol using an ultrasound bath for a minimum of 10 minutes. They were then dried in a vacuum oven at 343 K for about 10 minutes. The radii of the containers used for each IL and the amount of IL used are shown in Table A1.

Table A1. Mass and radius of container used for each IL

Ionic Liquid	Mass of IL Used (mg)	Radius of Container Used (cm)
$[C_2C_1im][BF_4]$	~ 56.4	0.63
$[C_2C_1im][TFES]$	~ 52.7	0.59
$[C_2C_1im][OAc]$	~ 51.5	0.64
$[C_4C_1im][OAc]$	~ 56.7	0.63
$[C_4C_1im][Cl]$	~ 63.1	0.63

The empty clean containers were placed into the instrument and measured at the same conditions at which the ionic liquid were to be measured. This was done to calculate for the correction factor mentioned in Chapter 2. Once this was completed, the ionic liquid was loaded into the clean container outside of the IGAsorp, and then introduced into the instrument to undergo pretreatment and begin the isotherm sorption measurements.

A.2 Density values

The densities used in the buoyancy corrections for ionic liquids $[C_2C_1im][BF_4]$, $[C_2C_1im][TFES]$, $[C_2C_1im][OAc]$, $[C_4C_1im][OAc]$, and $[C_4C_1im][Cl]$ are shown in Table A2.

Table A2. Densities for buoyancy corrections

Ionic Liquid	Temperatures (K)	Density (g/cm^3)	Source
$[C_2C_1im][BF_4]$	298.15 303.15	1.28 1.30	[78]Equation d/g, cm^{-3} = 1.5134 - $7.8297x10^{-4}$ T/K
$[C_2C_1im][TFES]$	293.15 303.15 313.15	1.44 1.43 1.42	Data[79]
$[C_2C_1im][OAc]$	293.15 303.15 313.15	1.10 1.10 1.09	Data[80]
$[C_4C_1im][OAc]$	294.85 303.15 315.15	1.05 1.05 1.04	[81]Equation 2 and 3 in literature
$[C_4C_1im][Cl]$	283.15 295.15 303.15	1.09 1.08 1.08	Linear equation fit to data from literature[82–87]

A.3 Solubility Results

The instrumental (or systematic) errors for w_{H2O} and x_{H2O} were calculated using the standard deviation of the measured mass when the mass vs. time reached equilibrium and at a constant T and RH. For isotherm set points which did not reach equilibrium and were instead estimated with the LDF equation (Eq. 2.2), the standard deviation calculation was applied to a section of data where the mass vs. time data measured was approximately constant. The w_{H2O} and x_{H2O} errors were calculated by propagating the measured mass errors using the force balance equation (Eq. 2.6).

Table A3. Absorption and Desorption Solubility Data for $[C_2C_1im][BF_4]$ at 298.15 K

Sorption	Relative Humidity (%)	Partial Pressure of water (kPa)	w_{H2O} (mass %)	x_{H2O} (mole %)
Absorption	0.00	0.00	0.0	0.0
Absorption	10.67	0.34	0.8	8.5
Absorption	30.67	0.97	2.8	24.3
Absorption	50.67	1.61	5.8	40.4
Absorption	70.67	2.24	11.8	59.4
Desorption	70.67	2.25	11.9	59.6
Desorption	50.67	1.61	5.8	40.4
Desorption	30.67	0.97	2.8	24.2
Desorption	10.67	0.34	0.8	8.5
Desorption	0.00	0.00	0.0	0.5

The instrumental uncertainties are: T = ± 0.01 K; % RH = ± 1 %; P_{H2O} < 1.01 kPa; w_{H2O} < 0.1 mass %, and x_{H2O} < ± 0.1 mol%.

Table A4. Absorption and Desorption Solubility Data for $[C_2C_1im][BF_4]$ at 303.15 K

Sorption	Relative Humidity (%)	Partial Pressure of water kPa	w_{H2O} (mass %)	x_{H2O} (mole %)
Absorption	0.00	0.00	0.0	0.0
Absorption	10.67	0.45	0.9	9.2
Absorption	30.67	1.30	3.0	25.6
Absorption	50.67	2.15	6.2	41.8
Absorption	60.67	2.58	8.5	50.5
Absorption	70.67	3.00	12.3	60.6
Desorption	70.67	3.01	12.1	60.3
Desorption	50.67	2.15	6.1	41.7
Desorption	0.00	0	0.0	0.0

The instrumental uncertainties are: T = ± 0.01 K; % RH = ± 1 %; P_{H2O} < 1.01 kPa; w_{H2O} < 0.1 mass %, and x_{H2O} < ± 0.1 mol%.

Table A5. Absorption and Desorption Solubility Data for $[C_2C_1im][TFES]$ at 293.15 K

Sorption	Relative Humidity (%)	Partial Pressure of water (kPa)	w_{H2O} (mass %)	x_{H2O} (mole %)
Absorption	0	0.00	0.00	0.0
Absorption	1	0.02	0.1	1.4
Absorption	5	0.12	0.4	6.1
Absorption	10	0.23	0.8	11.2
Absorption	15	0.35	1.2	16.2
Absorption	20	0.47	1.6	21.0
Absorption	25	0.58	2.1	25.7
Desorption	15	0.35	1.2	16.2
Desorption	5	0.12	0.4	6.0
Desorption	1	0.02	0.1	1.3
Desorption	0	0.00	0.0	-0.2

The instrumental uncertainties are: T = ± 0.01 K; % RH = ± 1 %; P_{H2O} < 1.01 kPa; w_{H2O} < 0.1 mass %, and x_{H2O} < ± 0.1 mol%.

Table A6. Absorption and Desorption Solubility Data for $[C_2C_1im][TFES]$ at 303.15 K

Sorption	Relative Humidity (%)	Partial Pressure of water (kPa)	w_{H2O} (mass %)	x_{H2O} (mole %)
Absorption	0	0.00	0.0	0.0
Absorption	1	0.04	0.1	1.6
Absorption	5	0.21	0.4	6.4
Absorption	10	0.42	0.8	11.8
Absorption	15	0.64	1.2	16.8
Absorption	20	0.85	1.7	21.7
Absorption	25	1.06	2.2	26.5
Desorption	15	0.64	1.2	16.8
Desorption	5	0.21	0.4	6.3
Desorption	0	0.00	-0.0	-0.2

The instrumental uncertainties are: T = ± 0.01 K; % RH = ± 1 %; P_{H2O} < 1.01 kPa; w_{H2O} < 0.1 mass %, and x_{H2O} < ± 0.1 mol%.

Table A7. Absorption and Desorption Solubility Data for $[C_2C_1im][TFES]$ at 313.15 K

Sorption	Relative Humidity (%)	Partial Pressure of water (kPa)	w_{H2O} (mass %)	x_{H2O} (mole %)
Absorption	0	0.00	0.0	0.0
Absorption	1	0.07	0.1	1.6
Absorption	5	0.37	0.4	6.6
Absorption	10	0.74	0.8	12.1
Absorption	15	1.11	1.3	17.2
Absorption	20	1.48	1.7	22.2
Absorption	25	1.85	2.2	26.9
Desorption	15	1.11	1.3	17.2
Desorption	5	0.37	0.4	6.4
Desorption	0	0.00	0.0	-0.2

The instrumental uncertainties are: T = ± 0.01 K; % RH = ± 1 %; P_{H2O} < 1.01 kPa; w_{H2O} < 0.1 mass %, and x_{H2O} < ± 0.1 mol%.

Table A8. Absorption and Desorption Solubility Data for $[C_2C_1im][OAc]$ at 293.15 K

Sorption	Relative Humidity (%)	Partial Pressure of water (kPa)	w_{H2O} (mass %)	x_{H2O} (mole %)
Absorption	0	0.00	0.0	0.0
Absorption	5	0.12	14.5	61.5
Absorption	10	0.23	18.9	68.8
Absorption	15	0.35	22.5	73.3
Absorption	20	0.47	25.6	76.5
Absorption	25	0.58	28.5%	79.0
Desorption	15	0.35	22.5	73.3
Desorption	5	0.12	14.3	61.2

The instrumental uncertainties are: T = ± 0.01 K; % RH = ± 1 %; P_{H2O} < 1.01 kPa; w_{H2O} < 0.1 mass %, and x_{H2O} < ± 0.1 mol%.

Table A9. Absorption and Desorption Solubility Data for $[C_2C_1im][OAc]$ at 303.15 K

Sorption	Relative Humidity (%)	Partial Pressure of water (kPa)	w_{H2O} (mass %)	x_{H2O} (mole %)
Absorption	0	0.00	0.0%	0.0
Absorption	2.5	0.11	10.7	53.1
Absorption	5	0.21	13.8	60.2
Absorption	10	0.42	18.3	67.9
Absorption	15	0.64	21.8	72.5
Absorption	20	0.85	24.9	75.8
Absorption	25	1.06	27.7	78.4
Desorption	15	0.64	21.5	72.1
Desorption	5	0.21	13.4	59.3

The instrumental uncertainties are: T = ± 0.01 K; % RH = ± 1 %; P_{H2O} < 1.01 kPa; w_{H2O} < 0.1 mass %, and x_{H2O} < ± 0.1 mol%.

Table A10. Absorption and Desorption Solubility Data for $[C_2C_1im][OAc]$ at 313.15 K

Sorption	Relative Humidity (%)	Partial Pressure of water (kPa)	w_{H2O} (mass %)	x_{H2O}[a] (mole %)
Absorption	0	0.00	0.0	0.0
Absorption	2.5	0.18	9.9	51.0
Absorption	5	0.37	13.2	59.0
Absorption	10	0.74	17.7	67.0
Absorption	15	1.11	21.1	71.7
Absorption	20	1.48	24.2	75.1
Absorption	25	1.85	26.9	77.7
Desorption	15	1.11	21.0	71.6
Desorption	5	0.37	13.0	58.6

The instrumental uncertainties are: T = ± 0.01 K; % RH = ± 1 %; P_{H2O} < 1.01 kPa; w_{H2O} < 0.1 mass %, and x_{H2O} < ± 0.1 mol%.

Table A11. Absorption and Desorption Solubility Data for $[C_4C_1im][OAc]$ at 294.85 K

Sorption	Relative Humidity (%)	Partial Pressure of water (kPa)	w_{H2O} (mass %)	x_{H2O} (mole %)
Absorption	0	0.00	0.0	0.0
Absorption	1.67	0.04	7.2	46.2
Absorption	5.67	0.15	11.8	59.4
Absorption	10.67	0.28	15.5	66.9
Absorption	15.67	0.41	18.6	71.6
Absorption	20.67	0.54	21.4	75.0
Absorption	25.67	0.67	24.2	77.8
Desorption	25.67	0.67	24.2	77.8
Desorption	20.67	0.54	21.5	75.0
Desorption	15.67	0.41	18.6	71.6
Desorption	10.67	0.28	15.5	66.9

The instrumental uncertainties are: T = ± 0.01 K; % RH = ± 1 %; P_{H2O} < 1.01 kPa; w_{H2O} < 0.1 mass %, and x_{H2O} < ± 0.1 mol%.

Table A12. Absorption and Desorption Solubility Data for $[C_4C_1im][OAc]$ at 303.15 K

Sorption	Relative Humidity (%)	Partial Pressure of water (kPa)	w_{H2O} (mass %)	x_{H2O} (mole %)
Absorption	0	0.00	0.0	0.0
Absorption	1.47	0.06	5.6	39.5
Absorption	1.67	0.07	6.4	42.9
Absorption	5.67	0.24	12.4	60.9
Absorption	10.67	0.45	15.7	67.1
Absorption	15.67	0.67	18.8	71.8
Absorption	20.67	0.88	21.8	75.4
Absorption	25.67	1.09	24.5	78.1
Desorption	25.67	1.09	24.4	78.0
Desorption	20.67	0.88	21.8	75.4
Desorption	15.67	0.67	19.0	72.1
Desorption	10.67	0.45	15.9	67.5
Desorption	5.67	0.24	12.2	60.4

The instrumental uncertainties are: $T = \pm 0.01$ K; % RH = ± 1 %; $P_{H2O} < 1.01$ kPa; $w_{H2O} < 0.1$ mass %, and $x_{H2O} < \pm$ 0.1 mol%.

Table A13. Absorption and Desorption Solubility Data for $[C_4C_1im][OAc]$ at 315.15 K

Sorption	Relative Humidity (%)	Partial Pressure of water (kPa)	w_{H2O} (mass %)	x_{H2O} (mole %)
Absorption	0	0.00	0.0	0.0
Absorption	1.47	0.12	5.1	37.3
Absorption	1.67	0.14	5.9	40.8
Absorption	5.67	0.47	11.7	59.2
Absorption	10.67	0.88	15.3	66.5
Absorption	15.67	1.29	18.3	71.2
Absorption	20.67	1.70	21.1	74.6
Absorption	25.67	2.11	23.7	77.4
Desorption	25.67	2.11	23.7	77.4
Desorption	20.67	1.70	21.1	74.6
Desorption	15.67	1.29	18.4	71.2
Desorption	10.67	0.88	15.3	66.6
Desorption	5.67	0.47	11.6	59.2
Desorption	1.67	0.14	6.0	41.3
Desorption	1.47	0.12	5.1	37.2
Desorption	0	0.00	0.4	4.2

The instrumental uncertainties are: $T = \pm 0.01$ K; % RH = ± 1 %; $P_{H2O} < 1.01$ kPa; $w_{H2O} < 0.1$ mass %, and $x_{H2O} < \pm$ 0.1 mol%.

Table A14. Absorption and Desorption Solubility Data for $[C_4C_1im][Cl]$ at 283.15 K

Sorption	Relative Humidity (%)	Partial Pressure of water (kPa)	w_{H2O} (mass %)	x_{H2O} (mole %)
Absorption	0	0.00	0.0	0.0
Absorption	1.66	0.02	6.3	39.6
Absorption	5.66	0.07	9.5	50.6
Absorption	10.66	0.14	12.4	57.9
Absorption	15.66	0.20	14.9	62.9
Absorption	20.66	0.26	17.2	66.8
Absorption	25.66	0.33	19.5	70.1
Desorption	15.66	0.20	14.9	62.9
Desorption	5.66	0.07	9.6	50.8
Desorption	1.66	0.02	6.3	39.6
Desorption	0	0.00	1.2	10.5

The instrumental uncertainties are: $T = \pm 0.01$ K; % RH = ± 1 %; $P_{H2O} < 1.01$ kPa; $w_{H2O} < 0.1$ mass %, and $x_{H2O} < \pm$ 0.1 mol%.

Table A15. Absorption and Desorption Solubility Data for $[C_4C_1im][Cl]$ at 295.15 K

Sorption	Relative Humidity (%)	Partial Pressure of water (kPa)	w_{H2O} (mass %)	x_{H2O} (mole %)
Absorption	0	0.00	0.0	0.0
Absorption	1.67	0.04	5.8	37.5
Absorption	5.67	0.15	9.2	49.6
Absorption	10.67	0.28	12.0	56.9
Absorption	15.67	0.41	14.4	61.9
Absorption	20.67	0.55	16.6	65.9
Absorption	25.67	0.68	18.9	69.3
Desorption	15.67	0.41	14.4	61.9
Desorption	5.67	0.15	9.2	49.4
Desorption	1.67	0.04	5.8	37.6
Desorption	0	0.00	0.5	4.6

The instrumental uncertainties are: $T = \pm 0.01$ K; % RH = ± 1 %; $P_{H2O} < 1.01$ kPa; $w_{H2O} < 0.1$ mass %, and $x_{H2O} < \pm$ 0.1 mol%.

Table A16. Absorption and Desorption Solubility Data for $[C_4C_1im][Cl]$ at 303.15 K

Sorption	Relative Humidity (%)	Partial Pressure of water (kPa)	w_{H2O} (mass %)	x_{H2O} (mole %)
Absorption	0	0.00	0.00	0.0
Absorption	1.66	0.07	5.6	36.7
Absorption	5.66	0.24	9.0	49.1
Absorption	10.66	0.45	11.8	56.5
Absorption	15.66	0.67	14.3	61.7
Absorption	20.66	0.88	16.5	65.7
Absorption	25.66	1.09	18.7	69.0
Desorption	15.66	0.67	14.2	61.6
Desorption	5.66	0.24	9.0	48.9
Desorption	1.66	0.07	5.7	36.8
Desorption	0	0.00	1.6	13.3

The instrumental uncertainties are: $T = \pm 0.01$ K; % RH = ± 1 %; $P_{H2O} < 1.01$ kPa; $w_{H2O} < 0.1$ mass %, and $x_{H2O} < \pm$ 0.1 mol%.

A.4 Liquid Fugacity Correction

The liquid fugacity correction $(f/P)sat_{,i}$ values were calculated for all measured temperatures using Eqs. A1 to A5 and REFPROP v9.2 to obtain the enthalpy and entropy values. It was assumed that because N_2 had insignificant solubility in the ionic liquid, the only liquid fugacity correction needed was that of water. The calculation begins with the fugacity equilibrium equation for water (Eq. A1):

$$f^L = f^V \tag{A1}$$

The next step is to calculate f^v with Eq. A2:

$$f^V(T,P) = Pexp\left[\frac{\underline{G}(T,P)-\underline{G}^{IG}(T,P)}{RT}\right] \tag{A2}$$

where $\underline{G}$ is the molar Gibbs energy of water at *T* and *P*, $\underline{G}^{IG}$ is the molar Gibbs energy of an ideal gas at *T* and *P*, and P is the total pressure. The molar Gibbs energy for an ideal gas is determined using Eq. A3, where $\underline{V}^{IG}$ is the molar volume for an ideal gas, and P_1 is a pressure low enough to consider water vapor an ideal gas (for example 0.1013 kPa).

$$\underline{G}(T,P_2) = \underline{G}(T,P_1) + \int_{P_1}^{P_2} \underline{V}\, dP = \underline{G}(T,P_1) + \ln\left(\frac{P_2}{P_1}\right) \tag{A3}$$

The Gibbs energies are calculated using the relationship in A4, where $\hat{H}$ and $\hat{S}$ are the specific enthalpy and specific entropy values for water at a certain *T*.

$$\hat{G} = \hat{H} - T\hat{S} \tag{A4}$$

The liquid fugacity f_L is equal to P^{sat} $(f/P)_{sat}$, replacing this in equation A1 and replacing F^v with equation A2, results in Eq. A5. To calculate the liquid fugacity correction, Eq A5 is solved for $(f/P)_{sat}$, where P^{sat} is the saturated vapor pressure of water at *T*.

$$P^{sat}(T)\left(\frac{f}{P}\right)_{sat} = Pexp\left[\frac{\underline{G}(T,P)-\underline{G}^{IG}(T,P)}{RT}\right] \tag{A5}$$

An example is shown below for T = 313.15 K and P_2 = 101.325 kPa and P_1 = 0.101325 kPa.

$$\hat{G}(T, P_1) = -631.1\ \text{J/g} = 2575.9\ \text{J/g} - 313.15\ \text{K} \times 10.241\ \text{J/(g K)} \quad \text{(A6)}$$

$$\underline{G}^{IG}(T, P_1) = \underline{G}(T, P_1) = -11{,}370\ \text{J/mol} = -631.1\ \text{J/g} \times 18.02\ \text{g/mol} \quad \text{(A7)}$$

$$\underline{G}^{IG}(T, P_2) = 6613\ \text{J/mol} = \text{-}11{,}370\ \text{J/mol} + 8.314\text{J/(mol K)} \times \ln(1000) \quad \text{(A8)}$$

$$\hat{G}(T, P_2) = -11.62\ \text{J/g} = 167.62\ \text{J/g} - 313.15\ \text{K} \times 0.57237\ \text{J/(g K)} \quad \text{(A9)}$$

$$\underline{G}(T, P_2) = -209.35\ \text{J/mol} = -11.62\ \text{J/g} \times 18.02\ \text{g/mol} \quad \text{(A10)}$$

The total pressure P is equal to P_2 (101.325 kPa), and P^{sat} is 7.385 kPa at 313.15 K. Using these values in Eq. A5 leads to Eq. A11.

$$\left(\frac{f}{P}\right)_{sat} = 0.9986 = \frac{101.325\ \text{kPa}}{7.385\ \text{kPa}} exp\left[\frac{-209.35\ \text{J/mol} - 6613\ \text{J/mol}}{8.314\text{J/(mol K)} \times 313.15\ \text{K}}\right] \quad \text{(A11)}$$

The results for all temperatures measured are shown in Table A17.

Table A17. Liquid fugacity coefficient correction values for all measured temperatures

Temperature (K)	$(f/P)_{sat,H2O}$
283.15	1.001
293.15	1.000
294.85	1.000
295.15	1.001
298.15	1.001
303.15	1.000
313.15	0.9986
315.15	0.9982

A.5 Time-Dependent Data

Below are some qualitative examples of the time dependent data measured by the IGAsorp.

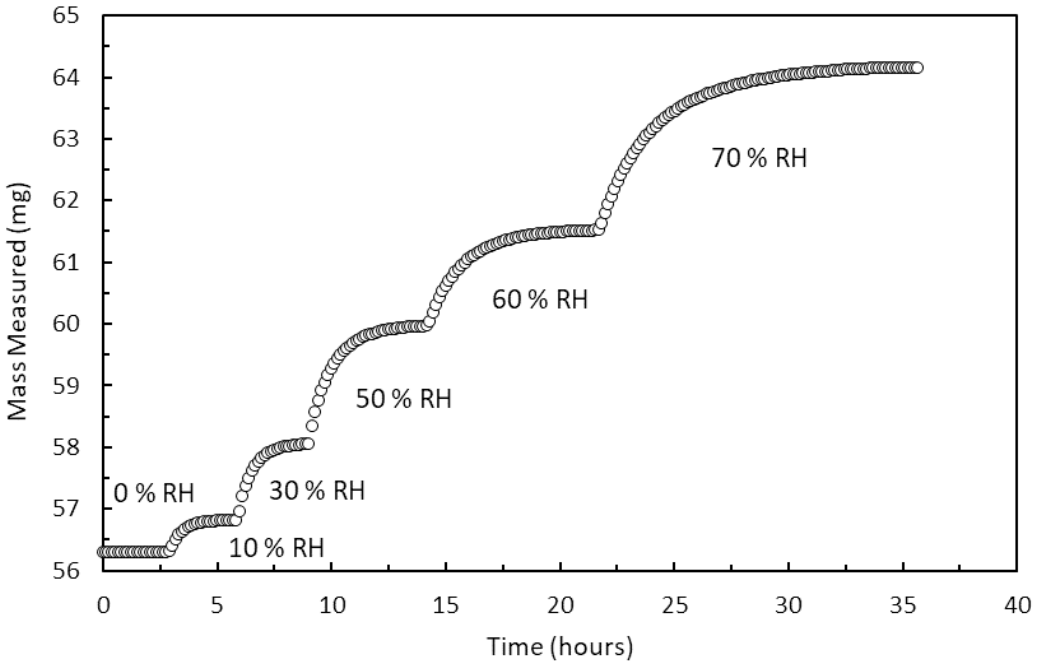

Figure A1. Raw time-dependent data for $[C_2C_1im][BF_4]$ at 303.15 K and multiple RH set points.

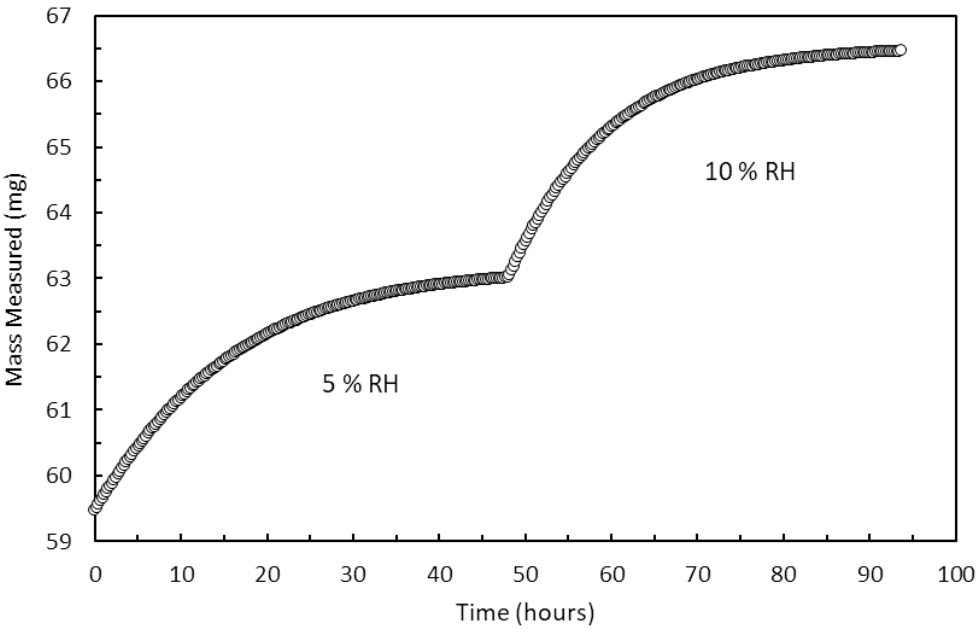

Figure A2. Raw time-dependent mass data for $[C_2C_1im][OAc]$ at 293.15 K and 5 % and 10 % RH.

A.6 Enthalpy Results

The heat of absorption errors were determining using the standard error of the slope for the linear regression Eq. 4.14.

Table A18. Enthalpy of Absorption Data for $[C_2C_1im][BF_4]$

x_{H2O} (mole fraction)	ΔH_{abs} (kJ/mol)	ΔH_{abs} Error (kJ/mol)
0.05	38.9	0.3
0.10	39.2	0.3
0.15	39.6	0.3
0.20	39.9	0.3
0.25	40.2	0.3
0.30	40.5	0.3
0.35	40.9	0.3
0.40	41.2	0.3
0.45	41.5	0.3
0.50	41.9	0.3
0.55	42.2	0.3
0.60	42.6	0.3
0.65	43.0	0.4
0.70	43.4	0.4
0.75	43.8	0.4
0.80	44.2	0.4

Table A19. Enthalpy of Absorption Data for $[C_2C_1im][TFES]$

x_{H2O} (mole fraction)	ΔH_{abs} (kJ/mol)	ΔH_{abs} Error (kJ/mol)
0.05	40.5	0.1
0.10	40.9	0.1
0.15	41.2	0.1
0.20	41.6	0.1
0.25	41.9	0.1
0.30	42.2	0.1

Table A20. Enthalpy of Absorption Data for $[C_2C_1im][OAc]$

x_{H2O} (mole fraction)	ΔH_{abs} (kJ/mol)	ΔH_{abs} Error (kJ/mol)
0.50	54.3	0.4
0.55	53.4	0.4
0.60	52.3	0.3
0.65	51.2	0.3
0.70	50.1	0.3
0.75	48.9	0.2
0.80	47.7	0.2

Table A21. Enthalpy of Absorption Data for $[C_4C_1im][OAc]$

x_{H2O} (mole fraction)	ΔH_{abs} (kJ/mol)	ΔH_{abs} Error (kJ/mol)
0.35	47.0	0.1
0.40	46.9	0.1
0.45	46.9	0.1
0.50	46.8	0.1
0.55	46.6	0.1
0.60	46.4	0.1
0.65	46.2	0.1
0.70	46.0	0.1
0.75	45.6	0.1
0.80	45.3	0.1

Table A22. Enthalpy of Absorption Data for $[C_4C_1im][Cl]$

x_{H2O} (mole fraction)	ΔH_{abs} (kJ/mol)	ΔH_{abs} Error (kJ/mol)
0.35	54.6	0.2
0.40	51.6	0.1
0.45	49.5	0.1
0.50	48.1	0.1
0.55	47.1	0.1
0.60	46.4	0.1
0.65	45.8	0.1
0.70	45.5	0.1

Error for the enthalpy of absorption was calculated using Eq. A12 at each mole fraction shown in Tables A18-22, where *C* is the constant arising from the derivative. Then the excel LINEST function was used to obtain the slope error, which was multiplied by *R* and converted to ΔH.

$$\ln(P) = \frac{1}{T} * \frac{\Delta H}{R} + C \tag{A12}$$

Appendix B: Liquid-Liquid Equilibria

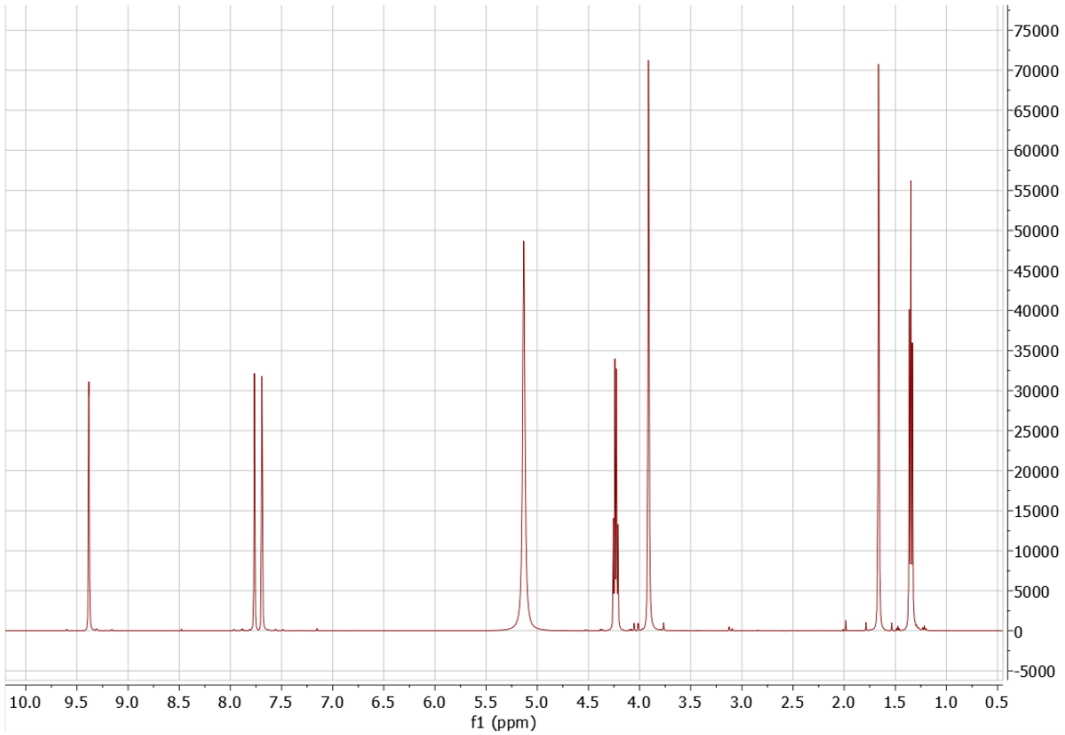

Figure B1. ^{1}H NMR Spectra for top liquid phase of $[C_2C_1im][NTf_2]$:$[C_2C_1im][OAc]$:H_2O mixture

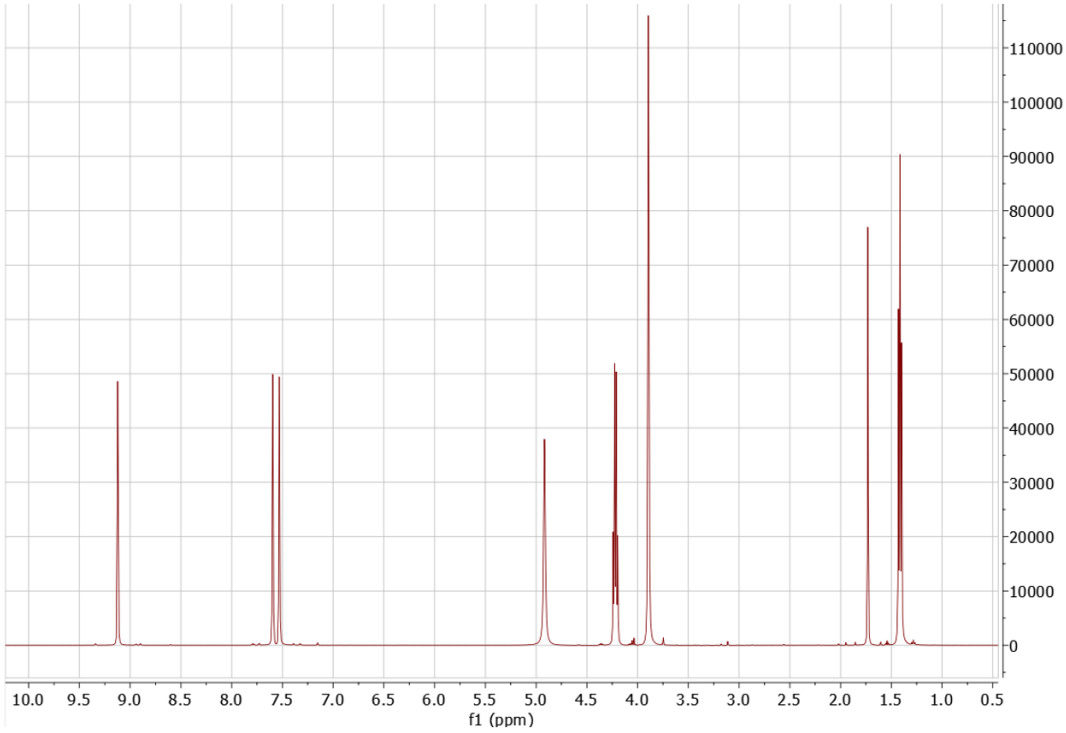

Figure B2. ^{1}H NMR Spectra for bottom liquid phase of $[C_2C_1im][NTf_2]$:$[C_2C_1im][OAc]$:H_2O mixture

B.1 Uncertainties

B.1.1 [C₂C₁im][NTf₂]:[C₂C₁im][OAc]:H₂O

Uncertainty for this system was determined calculating the absolute difference between the peak integrals of two $[C_2C_1im][NTf_2]$:$[C_2C_1im][OAc]$:H_2O mixtures tested by NMR (sample 1-36 vs. sample 1-37) as shown in Eq. B.1, and the maximum of the absolute errors was used as the integral peak errors σ_{a_k} (= 149,203). The errors were propagated across the mole fraction calculations.

$$\sigma_{x_k}^2 = \left(\frac{\delta_{x_k}}{\delta_{\frac{a_T}{n_T}}}\right)^2 {\sigma_{\frac{a_T}{n_T}}}^2 + \left(\frac{\delta_{x_k}}{\delta_{a_O}}\right)^2 {\sigma_{a_O}}^2 + \left(\frac{\delta_{x_k}}{\delta_{a_H}}\right)^2 {\sigma_{a_H}}^2 \Bigg|_{k=\begin{cases} T \\ O \\ H \end{cases}} \tag{B.1}$$

$$\frac{\delta_{x_T}}{\delta_{\frac{a_T}{n_T}}} = \frac{1}{\frac{a_T}{n_T}+\frac{a_O}{n_o}+\frac{a_H}{n_H}} - \frac{\frac{a_T}{n_T}}{\left(\frac{a_T}{n_T}+\frac{a_O}{n_O}+\frac{a_H}{n_H}\right)^2} = \frac{\frac{a_O}{n_O}+\frac{a_H}{n_H}}{\left(\frac{a_T}{n_T}+\frac{a_O}{n_O}+\frac{a_H}{n_H}\right)^2} \tag{B.2}$$

$$\frac{\delta_{x_T}}{\delta_{a_{(O\ or\ H)}}} = \frac{\frac{a_T}{n_T}\left(-\frac{1}{n_{(O\ or\ H)}}\right)}{\left(\frac{a_T}{n_T}+\frac{a_O}{n_O}+\frac{a_H}{n_H}\right)^2} \tag{B.3}$$

$$\frac{\delta_{x_O}}{\delta_{a_O}} = \frac{1}{n_O(\frac{a_T}{n_T}+\frac{a_O}{n_o}+\frac{a_H}{n_H})} - \frac{\frac{a_O}{n_O}}{n_O\left(\frac{a_T}{n_T}+\frac{a_O}{n_O}+\frac{a_H}{n_H}\right)^2} = \frac{\frac{a_T}{n_T}+\frac{a_H}{n_H}}{n_O\left(\frac{a_T}{n_T}+\frac{a_O}{n_O}+\frac{a_H}{n_H}\right)^2} \tag{B.4}$$

$$\frac{\delta_{x_O}}{\delta_{a_H}} = \frac{\frac{a_O}{n_O}\left(-\frac{1}{n_H}\right)}{\left(\frac{a_T}{n_T}+\frac{a_O}{n_O}+\frac{a_H}{n_H}\right)^2} \tag{B.5}$$

$$\frac{\delta_{x_O}}{\delta_{a_T/n_T}} = \frac{\frac{a_O}{n_O}}{\left(\frac{a_T}{n_T}+\frac{a_O}{n_O}+\frac{a_H}{n_H}\right)^2} \tag{B.6}$$

$$\frac{\delta_{x_H}}{\delta_{a_H}} = \frac{1}{n_H(\frac{a_T}{n_T}+\frac{a_O}{n_o}+\frac{a_H}{n_H})} - \frac{\frac{a_H}{n_H}}{n_H\left(\frac{a_T}{n_T}+\frac{a_O}{n_O}+\frac{a_H}{n_H}\right)^2} = \frac{\frac{a_T}{n_T}+\frac{a_O}{n_O}}{n_H\left(\frac{a_T}{n_T}+\frac{a_O}{n_O}+\frac{a_H}{n_H}\right)^2} \tag{B.7}$$

$$\frac{\delta_{x_H}}{\delta_{a_O}} = \frac{\frac{a_H}{n_H}\left(-\frac{1}{n_O}\right)}{\left(\frac{a_T}{n_T}+\frac{a_O}{n_O}+\frac{a_H}{n_H}\right)^2} \tag{B.8}$$

$$\sigma_{\frac{a_T}{n_T}} = \sum_{k=1}^{8} \left(\frac{\delta_{\frac{a_T}{n_T}}}{\delta_{a_k}} \right)^2 {\sigma_{a_k}}^2 \; for \; k \neq 4 \tag{B.9}$$

$$\frac{\delta_{\frac{a_T}{n_T}}}{\delta_{a_k}} = \frac{1}{n \times 6} \; \text{for} \; k = 1, 2, 3, 5, 6 \tag{B.10}$$

$$\frac{\boldsymbol{\delta_{\frac{a_T}{n_T}}}}{\boldsymbol{\delta_{a_o}}} = -\frac{\mathbf{1}}{\boldsymbol{n_O}} \tag{B.11}$$

$$\sigma_{a_k} = absolute \; error = \max\left(\left| a_{k_{1-36}} - a_{k_{1-37}} \right|_{for \; k=1 \; to \; 8} \right) \tag{B.12}$$

It was also assumed that the error from the acetate and water peaks were equal to σ_{ak}.

$$\sigma a_O = \sigma a_H = \sigma a_k \tag{B.13}$$

Once the errors for the mole fractions were determined, the errors for the mass % could be calculated. First, Eq B.14 was used to convert from mole fractions to mass fractions, where *i* is again the *ith* phase and *J* is the species.

$$w_{iJ} = \frac{x_{iJ} MW_J}{x_{iT} MW_T + x_{iO} MW_O + x_{iH} MW_H} \tag{B.14}$$

Next, the error for each mole fraction is propagated for each mass%, an example is shown for w_{iT} in Eqs. B.15-B.17.

$$\sigma^2_{w_{iT}} = \left(\frac{\delta_{w_{iT}}}{\delta_{x_{iT}}} \right)^2 {\sigma_{x_{iT}}}^2 + \left(\frac{\delta_{w_{iT}}}{\delta_{x_{iO}}} \right)^2 {\sigma_{x_{iO}}}^2 + \left(\frac{\delta_{w_{iT}}}{\delta_{x_{iH}}} \right)^2 {\sigma_{x_{iH}}}^2 \tag{B.15}$$

$$\frac{\delta_{w_{iT}}}{\delta_{x_{iT}}} = \frac{(x_{iO} MW_O + x_{iH} MW_H) MW_T}{(x_{iT} MW_T + x_{iO} MW_O + x_{iH} MW_H)^2} \tag{B.16}$$

$$\frac{\delta_{w_{iT}}}{\delta_{x_{ik}}} = \frac{-(x_{iT} MW_T) MW_k}{(x_{iT} MW_T + x_{iO} MW_O + x_{iH} MW_H)^2} \; where \; k = O \; or \; H \tag{B.17}$$

As mentioned in Chapter 5, Eqs. 5.5-5.10 were solved simultaneously using Excel solver to guess a total mass for the top phase and for the bottom phase. Equations 5.8-5.10 can be re-written as

shown in B.18-B.20, where T_{Wtop} is the total mass of the top phase and T_{Wbo} is the total mass of the bottom phase:

$$T_{WT} = w_{topT}T_{Wtop} + w_{botT}T_{Wbot} \quad \text{(B.18)}$$

$$T_{WO} = w_{topO}T_{Wtop} + w_{botO}T_{Wbot} \quad \text{(B.19)}$$

$$T_{WH} = w_{topH}T_{Wtop} + w_{botH}T_{Wbot} \quad \text{(B.20)}$$

In order to estimate an uncertainty for the estimated mass of the top phase and of the bottom phase, pairs of equations were solved simultaneously for a common variable. For example, Eqs. B.18 and Eq B.19 were solved together for T_{Wtop}, same as Eqs. B.18 and B.20, and equations B.19 and B.20. Equation B.21 shows Eq B.19 solved for T_{Wbot} and replaced in Eq. B.18. The equation is rearranged for T_{Wtop} as shown in Eq. B.22, and the errors for w_{iJ} are propagated throughout.

$$T_{WT} = w_{topT}T_{Wtop} + w_{botT} * \frac{(T_{WO} - w_{topO}T_{Wtop})}{w_{botO}} \quad \text{(B.21)}$$

$$T_{Wtop} = \frac{T_{WT} - \frac{T_{WO}w_{botT}}{w_{botO}}}{w_{topT} - \frac{w_{botT}w_{topO}}{w_{botO}}} \quad \text{(B.22)}$$

$$\sigma^2_{T_{Wtop}} = \left(\frac{\delta_{T_{Wtop}}}{\delta_{T_{WT}}}\right)^2 {\sigma_{T_{WT}}}^2 + \left(\frac{\delta_{T_{Wtop}}}{\delta_{T_{WO}}}\right)^2 {\sigma_{T_{WO}}}^2 + \left(\frac{\delta_{T_{Wtop}}}{\delta_{w_{botT}}}\right)^2 {\sigma_{w_{botT}}}^2 + \left(\frac{\delta_{T_{Wtop}}}{\delta_{w_{botO}}}\right)^2 {\sigma_{w_{botO}}}^2 +$$

$$\left(\frac{\delta_{T_{Wtop}}}{\delta_{w_{topT}}}\right)^2 {\sigma_{w_{topT}}}^2 + \left(\frac{\delta_{T_{Wtop}}}{\delta_{w_{topO}}}\right)^2 {\sigma_{w_{topO}}}^2 \quad \text{(B.23)}$$

$$\frac{\delta_{T_{Wtop}}}{\delta_{T_{WT}}} = \frac{1}{w_{topT} - \frac{w_{botT}w_{topO}}{w_{botO}}} \quad \text{(B.24)}$$

$$\frac{\delta_{T_{Wtop}}}{\delta_{T_{WO}}} = \frac{-\frac{w_{botT}}{w_{botO}}}{w_{topT} - \frac{w_{botT}w_{topO}}{w_{botO}}} \quad \text{(B.25)}$$

$$\frac{\delta_{T_{Wtop}}}{\delta_{w_{botT}}} = \frac{w_{botO}w_{topO}T_{WT} - w_{topT}w_{botO}T_{WO}}{(w_{topT}w_{botO} - w_{botT}w_{topO})^2} \quad \text{(B.26)}$$

$$\frac{\delta_{T_{Wtop}}}{\delta_{w_{botO}}} = \frac{w_{botT}(w_{topT}T_{WO} - w_{topO}T_{WT})}{(w_{topT}w_{botO} - w_{botT}w_{topO})^2} \quad \text{(B.27)}$$

$$\frac{\delta_{T_{Wtop}}}{\delta_{w_{topT}}} = \frac{w_{botO}(w_{botT}T_{WO} - w_{botO}T_{WT})}{(w_{topT}w_{botO} - w_{botT}w_{topO})^2} \quad \text{(B.28)}$$

$$\frac{\delta_{T_{Wtop}}}{\delta_{w_{topO}}} = \frac{w_{botT}(w_{botO}T_{WT} - w_{botT}T_{WO})}{(w_{topT}w_{botO} - w_{botT}w_{topO})^2} \quad \text{(B.29)}$$

Using these forms of equations, we obtained σT_{Wtop} three times (pairing Eq. B.18 with Eq. B.19, Eq. B.18 with Eq. B.20, and Eq. B.19 with Eq. B.20). From these results, the largest error was used as the error for the total mass in the top phase. The same method was applied to obtain the uncertainty for T_{Wbot}.

The error for species in the top phase mass partition can therefore be calculated using the estimated values for σT_{Wtop} and σT_{Wbot} and propagated using Eqs. B.30-B.32,

$$\sigma_{P_{topJ}}^2 = \left(\frac{\delta_{P_{topJ}}}{\delta_{w_{topJ}}}\right)^2 {\sigma_{w_{topJ}}}^2 + \left(\frac{\delta_{P_{topJ}}}{\delta_{w_{botJ}}}\right)^2 {\sigma_{w_{botJ}}}^2 + \left(\frac{\delta_{P_{topJ}}}{\delta_{T_{Wtop}}}\right)^2 {\sigma_{T_{Wtop}}}^2 + \left(\frac{\delta_{P_{topJ}}}{\delta_{T_{Wbot}}}\right)^2 {\sigma_{T_{Wbot}}}^2 \quad \text{(B.30)}$$

$$\frac{\delta_{P_{topJ}}}{\delta_{w_{topJ}}} = \frac{w_{botJ}\,T_{Wbot}T_{Wtop}}{(w_{topJ}\,T_{Wtop} + w_{botJ}\,T_{Wbot})^2} \quad \text{(B.31)}$$

$$\frac{\delta_{P_{topJ}}}{\delta_{w_{botJ}}} = \frac{-w_{topJ}T_{Wtop}T_{Wbot}}{(w_{topJ}\,T_{Wtop} + w_{botJ}\,T_{Wbot})^2} \quad \text{(B.32)}$$

$$\frac{\delta_{P_{topJ}}}{\delta_{T_{Wtop}}} = \frac{w_{botJ}\,T_{Wbot}w_{topJ}}{(w_{topJ}\,T_{Wtop} + w_{botJ}\,T_{Wbot})^2} \quad \text{(B.33)}$$

$$\frac{\delta_{P_{topJ}}}{\delta_{T_{Wbot}}} = \frac{-w_{topJ}T_{Wtop}w_{botJ}}{(w_{topJ}\,T_{Wtop} + w_{botJ}\,T_{Wbot})^2} \quad \text{(B.34)}$$

Similar equations can be derived for the bottom phase for all species.

The overall top phase mass partition error was calculated as shown in Eqs. B.35 and B.36:

$$\sigma_{P_{T_{Wtop}}}^2 = \left(\frac{\delta_{P_{T_{Wtop}}}}{\delta_{T_{Wtop}}}\right)^2 {\sigma_{T_{Wtop}}}^2 + \left(\frac{\delta_{P_{T_{Wtop}}}}{\delta_{T_{Wbot}}}\right)^2 {\sigma_{T_{Wbot}}}^2 \quad \text{(B.35)}$$

$$\sigma^2_{P_{T_{Wtop}}} = \left(\frac{T_{Wbot}}{\left(T_{Wtop}+T_{Wbot}\right)^2}\right)^2 {\sigma_{T_{Wtop}}}^2 + \left(\frac{-T_{Wtop}}{\left(T_{Wtop}+T_{Wbot}\right)^2}\right)^2 {\sigma_{T_{Wbot}}}^2 \quad \text{(B.36)}$$

A similar equation can be derived for the bottom phase overall mass partition, which will result in the same answer. The same equations were applied to calculate the error of the overall mass partition of the measured masses for the top and bottom. The only difference is that the σT_{Wtop} and σT_{Wbot} terms were determined from the balance error to be 0.0284 g and 0.0367 g, respectively.

The uncertainty for the mass of each species was calculated using Eqs B.37 and B.38, and the uncertainty for the moles of each species was easily calculated using Eq B.39, where W_{iJ} is the mass of species *J* in phase *i*.

$$W_{iJ} = w_{iJ} T_{Wi} \quad \text{(B.37)}$$

$$\sigma^2_{W_{iJ}} = \left(\frac{\delta_{W_{iJ}}}{\delta_{w_{iJ}}}\right)^2 {\sigma_{w_{iJ}}}^2 + \left(\frac{\delta_{W_{iJ}}}{\delta_{T_{Wi}}}\right)^2 {\sigma_{T_{Wi}}}^2 = T^2_{Wi} * {\sigma_{w_{iJ}}}^2 + w^2_{iJ} * {\sigma_{T_{Wi}}}^2 \quad \text{(B.38)}$$

$$\sigma n_{iJ} = \frac{\sigma W_{iJ}}{MW_J} \quad \text{(B.39)}$$

Finally, the error for the total moles of each phase was calculated using the determined σ_{niJ} values, where *i* is the ith phase:

$$\sigma Ni^2 = \sigma n^2_{iT} + \sigma n^2_{iO} + \sigma n^2_{iH} \quad \text{(B.40)}$$

B.1.2 [C_2C_1im][NTf_2]:[C_2C_1im][Cl]:H_2O

The uncertainty for the mass of [C_2C_1im][NTf_2] was determined by propagating the error of C_T and vol_i in Eq. B.41, where vol_i is the volume of the specific phase of interest.

$$W_T = C_T vol_i MW_T \tag{B.41}$$

$$\sigma_{W_T}^2 = \left(\frac{\delta_{W_T}}{\delta_{C_T}}\right)^2 \sigma_{C_T}^2 + \left(\frac{\delta_{W_T}}{\delta_{vol_i}}\right)^2 \sigma_{vol_i}^2 \tag{B.42}$$

$$\frac{\delta_{W_T}}{\delta_{C_T}} = vol_i MW_T \tag{B.43}$$

$$\frac{\delta_{W_T}}{\delta_{vol_i}} = C_T MW_T \tag{B.44}$$

The volume of each phase (i.e., layer) vol_i was determined using the water weight and density as mentioned earlier. Three measurements were performed, and the error was calculated with equations B.45-B.47 where i is the *ith* phase. The water mass errors were σW_{Hltop} = 0.0007 g and σW_{Hlbot} = 0.0116 g.

$$vol_i = \frac{\sum_{l=1}^{3} w_{Hl}}{3\rho_{w@294.52\ K}} \tag{B.45}$$

$$\sigma_{vol_i}^2 = \sum_{l=1}^{3} \left(\frac{\delta vol_i}{\delta W_{Hli}}\right)^2 \sigma W_{Hli}^2 \tag{B.46}$$

$$\frac{\delta vol_i}{\delta W_{Hli}} = \frac{1}{3\rho_{w@294.52\ \mathrm{K}}} \tag{B.47}$$

The concentration of [C_2C_1im][NTf_2] C_{Ti} in phase i can be written as shown in Eq. B.48, where W_{std} is the total mass of the fluorine standard used to make the standard solution and vol_{std} is the volume of the standard solution. The error σW_{std} = 0.0004 g was determined from the balance error, σI_{Ttop} = 450, σI_{Rtop} =1800.5, σI_{Tbot} = 1735, σI_{Rtop} =125.24 were determined from standard deviations of values shown earlier in Tables 5.12 and 5.13.

$$C_{Ti} = \frac{W_{std}}{vol_{std} MW_{std}} \frac{I_{Ti}}{I_{Ri}} \frac{V_R}{V_T} \tag{B.48}$$

$$\sigma^2_{C_{Ti}} = \left(\frac{\delta_{C_{Ti}}}{\delta_{w_{std}}}\right)^2 \sigma^2_{w_{std}} + \left(\frac{\delta_{C_{Ti}}}{\delta_{vol_{std}}}\right)^2 \sigma^2_{vol_{std}} + \left(\frac{\delta_{C_{Ti}}}{\delta_{I_{Ti}}}\right)^2 \sigma^2_{I_{Ti}} + \left(\frac{\delta_{C_{Ti}}}{\delta_{I_{Ri}}}\right)^2 \sigma^2_{I_{Ri}} + \left(\frac{\delta_{C_{Ti}}}{\delta_{\frac{V_R}{V_T}}}\right)^2 \sigma^2_{\frac{V_R}{V_T}} \tag{B.49}$$

$$\frac{\delta_{C_{Ti}}}{\delta_{W_{std}}} = \frac{1}{vol_{std} MW_{std}} \frac{I_{Ti}}{I_{Ri}} \frac{V_R}{V_T} \tag{B.50}$$

$$\frac{\delta_{C_{Ti}}}{\delta_{vol_{std}}} = -\frac{W_{std}}{MW_{std}} \frac{I_{Ti}}{I_{Ri}} \frac{V_R}{V_T} \frac{1}{vol^2_{std}} \tag{B.51}$$

$$\frac{\delta_{C_{Ti}}}{\delta_{I_{Ti}}} = \frac{W_{std}}{vol_{std} MW_{std}} \frac{1}{I_{Ri}} \frac{V_R}{V_T} \tag{B.52}$$

$$\frac{\delta_{C_{Ti}}}{\delta_{I_{Ri}}} = \frac{W_{std}}{vol_{std} MW_{std}} \frac{I_{Ti}}{I^2_{Ri}} \frac{V_R}{V_T} \tag{B.53}$$

$$\frac{\delta_{C_{Ti}}}{\delta_{\frac{V_R}{V_T}}} = \frac{W_{std}}{vol_{std} MW_{std}} \frac{I_{Ti}}{I_{Ri}} \tag{B.54}$$

The volume of the standard solution was determined using the water weight and density as mentioned earlier. Four measurements were performed, and the water weighing error was w_{Hr} = 0.0004 g.

$$\sigma^2_{vol_{std}} = \sum_{r=1}^{4} \left(\frac{\delta vol_{std}}{\delta w_{Hr}}\right)^2 \sigma w^2_{Hr} \tag{B.55}$$

$$vol_i = \frac{\sum_{r=1}^{4} w_{Hr}}{4\rho_{w@294.08\,K}} \tag{B.56}$$

$$\frac{\delta vol_{std}}{\delta w_{Hr}} = \frac{1}{4\rho_{w@294.08\,K}} \tag{B.57}$$

As mentioned earlier, the concentration of $[C_2C_1im][Cl]$ for each phase was determined by taking the average of $C_{i[C2C1im][Cl]}$ for both M and N samples, as shown in Eq. B.58. The error for the concentration of $[C_2C_1im][Cl]$ was determined by error propagation as shown below, and the errors for σC_{iM}, σC_{iN}, σW_W, σW_S are listed in Table B1.

$$\text{Final } C_{i[C_2C_1m][Cl]} = \left(C_{i[C_2C_1im][Cl]}\Big|_{from\ M\ dilution} + C_{i[C_2C_1im][Cl]}\Big|_{from\ N\ dilution}\right) \div 2 \tag{B.58}$$

$$\sigma^2_{C_{i[C2C_1m][Cl]}} = \left(\frac{\delta_{C_{i[C2mim][Cl]}}}{\delta_{C_{i[C2mim][Cl]\,M}}}\right)^2 \sigma^2_{C_{i[C2C1im][Cl]\,M}} + \left(\frac{\delta_{C_{i[C2C1im][Cl]}}}{\delta_{C_{i[C2C1im][Cl]\,N}}}\right)^2 \sigma^2_{C_{i[C2C1im][Cl]\,N}} \quad \text{(B.59)}$$

$$\frac{\delta_{C_{i[C2C1im][Cl]}}}{\delta_{C_{i[C2C1im][Cl]M}}} = \frac{1}{2} \quad \text{(B.60)}$$

$$\frac{\delta_{C_{i[C2C1im][Cl]}}}{\delta_{C_{i[C2C1im][Cl]N}}} = \frac{1}{2} \quad \text{(B.61)}$$

$$\sigma^2_{C_{i[C2mim][Cl]U}} = \left(\frac{\delta_{C_{i[C2mim][Cl]U}}}{\delta_{C_{iO}}}\right)^2 \sigma^2_{C_{iO}} \Bigg| \; where\ U = M\ or\ N \quad \text{(B.62)}$$

$$\left(\frac{\delta_{C_{i[C2C1im][Cl]U}}}{\delta_{C_{iO}}}\right) = \frac{1\ g}{1000\ mg} * \frac{1\ kg}{1000\ g} * \frac{1\ mol\ Cl}{35.453\ g} * \frac{1\ mol\ [C_2C_1im][Cl]}{mol\ Cl} * \frac{146.62\ g}{mol\ [C_2C_1im][Cl]} \Bigg| \; where\ U = M\ or\ N \quad \text{(B.63)}$$

$$\sigma^2_{C_{iO}} = \left(\frac{\delta_{C_{iO}}}{\delta_{C_{iK}}}\right)^2 \sigma^2_{C_{iK}} + \left(\frac{\delta_{C_{iO}}}{\delta_{W_{W_{iK}}}}\right)^2 \sigma^2_{W_{W_{iK}}} + \left(\frac{\delta_{C_{iO}}}{\delta_{W_{S_{iK}}}}\right)^2 \sigma^2_{W_{S_{iK}}} \quad \text{(B.64)}$$

$$\frac{\delta_{C_{iO}}}{\delta_{C_{iK}}} = \frac{W_{w_{iK}} + W_{S_{iK}}}{W_{S_{iK}}} \quad \text{(B.65)}$$

$$\frac{\delta_{C_{iO}}}{\delta_{W_{W_{iK}}}} = \frac{C_{iK}}{W_{S_{iK}}} \quad \text{(B.66)}$$

$$\frac{\delta_{C_{iO}}}{\delta_{W_{W_{iK}}}} = -\frac{C_{PK} W_{w_{iK}}}{W^2_{S_{iK}}} \quad \text{(B.67)}$$

$$\sigma^2_{C_{iK}} = \left(\frac{\delta_{C_{iK}}}{\delta_{C_{iL}}}\right)^2 \sigma^2_{C_{iL}} + \left(\frac{\delta_{C_{iK}}}{\delta_{W_{W_{iL}}}}\right)^2 \sigma^2_{W_{W_{iL}}} + \left(\frac{\delta_{C_{iK}}}{\delta_{W_{S_{iL}}}}\right)^2 \sigma^2_{W_{S_{iL}}} \quad \text{(B.68)}$$

$$\frac{\delta_{C_{iK}}}{\delta_{C_{iL}}} = \frac{W_{w_{iL}} + W_{S_{iL}}}{W_{S_{iL}}} \quad \text{(B.69)}$$

$$\frac{\delta_{C_{iK}}}{\delta_{W_{w_{iL}}}} = \frac{C_{iL}}{W_{S_{iL}}} \quad \text{(B.70)}$$

$$\frac{\delta_{C_{iK}}}{\delta_{W_{S_{iL}}}} = -\frac{C_{iL} W_{w_{iL}}}{W^2_{S_{iL}}} \quad \text{(B.71)}$$

$$\sigma^2_{C_{iL}} = \left(\frac{\delta_{C_{iL}}}{\delta_{C_{iU}}}\right)^2 \sigma^2_{C_{iU}} + \left(\frac{\delta_{C_{iL}}}{\delta_{W_{w_{iU}}}}\right)^2 \sigma^2_{W_{w_{iU}}} + \left(\frac{\delta_{C_{iL}}}{\delta_{W_{S_{iU}}}}\right)^2 \sigma^2_{W_{S_{iU}}} \Bigg|_{U = M\ or\ N} \quad \text{(B.72)}$$

$$\frac{\delta_{C_{iL}}}{\delta_{C_{iU}}} = \frac{W_{w_{iU}} + W_{s_{iU}}}{W_{s_{iU}}} \Bigg| U = M \text{ or } N \tag{B.73}$$

$$\frac{\delta_{C_{iL}}}{\delta_{W_{w_{iU}}}} = \frac{C_{iU}}{W_{s_{iU}}} \Bigg| U = M \text{ or } N \tag{B.74}$$

$$\frac{\delta_{C_{iL}}}{\delta_{W_{s_{iU}}}} = -\frac{C_{iU} W_{w_{iU}}}{W_{s_{iU}}^2} \Bigg| U = M \text{ or } N \tag{B.75}$$

Table B1. List of uncertainty terms for the [C_2C_1im][Cl] concentration error calculation

Term	Top Phase Value (g)	Bottom Phase Value (g)
σC_{iM}	0.0030	0.0104
σC_{iN}	0.0146	0.0002
σW_{SiM}	0.0007	0.0007
σW_{WiM}	0.0116	0.0116
σW_{SiN}	0.0004	0.0004
σW_{WiN}	0.0116	0.0116
σW_{SiL}	0.0004	0.0004
σW_{WiL}	0.0116	0.0116
σW_{SiK}	0.0004	0.0004
σW_{WiK}	0.0116	0.0116

The error for the estimated masses at the top and bottom were calculated using Eqs. B.76-B.77 to propagate the error of W_{iT}, w_{iC}, *ad* w_{iH} within Eq 5.22.

$$\sigma_{T_{Wi}}^2 = \left(\frac{\delta T_{Wi}}{\delta W_{iT}}\right)^2 \sigma W_{iT}^2 + \left(\frac{\delta T_{Wi}}{\delta w_{iC}}\right)^2 \sigma w_{iC}^2 + \left(\frac{\delta T_{Wi}}{\delta w_{iH}}\right)^2 \sigma w_{iH}^2 \tag{B.76}$$

$$\frac{\delta T_{Wi}}{\delta W_{iT}} = \frac{1}{1 - w_{iC} - w_{iH}} \tag{B.77}$$

$$\frac{\delta T_{Wi}}{\delta w_{iC}} = \frac{-W_{iT}}{(1 - w_{iC} - w_{iH})^2} \tag{B.78}$$

$$\frac{\delta T_{Wi}}{\delta w_{iH}} = \frac{-W_{iT}}{(1-w_{iC}-w_{iH})^2} \tag{B.79}$$

The σT_{wi} error, along with the already measured error for W_{iT}, was used to calculate the error of the mass fraction of $[C_2C_1im][NTf_2]$ in both phases, as shown in Eq B.80 to B.82.

$$\sigma_{w_{iT}}^2 = \left(\frac{\delta w_{iT}}{\delta W_{iT}}\right)^2 \sigma_{W_{iT}}^2 + \left(\frac{\delta w_{iT}}{\delta T_{Wi}}\right)^2 \sigma_{T_{Wi}}^2 \tag{B.80}$$

$$\frac{\delta w_{iT}}{\delta W_{iT}} = \frac{1}{T_{Wi}} \tag{B.81}$$

$$\frac{\delta w_{iT}}{\delta T_{Wi}} = \frac{-W_{iT}}{T_{Wi}^2} \tag{B.82}$$

The errors for the estimated mass of $[C_2C_1im][Cl]$ and water were calculated with Eq B.83, where the mass percent errors (σw_{iC} and σw_{iH}) had been previously calculated.

$$\sigma_{W_{ik}}^2 = \left(\frac{\delta W_{ik}}{\delta w_{ik}}\right)^2 \sigma_{w_{ik}}^2 + \left(\frac{\delta W_{ik}}{\delta T_{Wi}}\right)^2 \sigma_{T_{Wi}}^2 \Big|_{k=H\ or\ C} = T_{Wi}^2 * {\sigma_{w_{ik}}}^2 + w_{ik}^2 * {\sigma_{T_{Wi}}}^2 \Big|_{k=H\ or\ C} \tag{B.83}$$

Errors for moles of each species were calculated using Eq B.39, and total moles were calculated with Eq B.40. Since mass percent errors were calculated, the errors for mole fractions could also be calculated. First, Eq B.84 was used to convert from mass percent to mole fractions, where *i* is the *ith* phase and *J* is the species.

$$x_{iJ} = \frac{w_{iJ}/MW_J}{w_{iT}/MW_T + w_{iC}/MW_C + w_{iH}/MW_H} \tag{B.84}$$

Next, the error for each mass percent was propagated for each mole percent, an example is shown for x_{iT} in Eqs. B.85-B.87.

$${\sigma x_{iT}}^2 = \left(\frac{\delta x_{iT}}{\delta w_{iT}}\right)^2 {\sigma w_{iT}}^2 + \left(\frac{\delta x_{iT}}{\delta w_{iC}}\right)^2 {\sigma w_{iC}}^2 + \left(\frac{\delta x_{iT}}{\delta w_{iH}}\right)^2 {\sigma w_{iH}}^2 \tag{B.85}$$

$$\frac{\delta x_{iT}}{\delta w_{iT}} = \frac{(w_{iC}/MW_C + w_{iH}/MW_H)/MW_T}{(w_{iT}/MW_T + w_{iC}/MW_C + w_{iH}/MW_H)^2} \tag{B.86}$$

$$\frac{\delta x_{iT}}{\delta w_{ik}} = \frac{-(w_{iT}/MW_T)/MW_k}{(w_{iT}/MW_T + w_{iC}/MW_C + w_{iH}/MW_H)^2}\ where\ k = O\ or\ H \tag{B.87}$$

The top species partition error was determined with Eqs. B.89-B.91 for species J. Similar equations can be used to calculate the bottom species partition error.

$$\sigma_{P_{topJ}}^2 = \left(\frac{\delta P_{topJ}}{\delta W_{topJ}}\right)^2 \sigma_{W_{topJ}}{}^2 + \left(\frac{\delta P_{topJ}}{\delta W_{botJ}}\right)^2 \sigma_{W_{botJ}}{}^2 \quad \text{(B.89)}$$

$$\frac{\delta P_{topJ}}{\delta W_{topJ}} = \frac{W_{botJ}}{\left(W_{topJ}+W_{botJ}\right)^2} \quad \text{(B.90)}$$

$$\frac{\delta P_{topJ}}{\delta W_{topJ}} = \frac{-W_{topJ}}{\left(W_{topJ}+W_{botJ}\right)^2} \quad \text{(B.91)}$$

The error for the overall mass partition of the estimated and measured masses for the top and bottom phases were calculated the same way as done for the $[C_2C_1im][NTf_2]$:$[C_2C_1im][OAc]$:H_2O system, with Eqs. B.35 and B.36. The σT_{Wtop} and σT_{Wbot} terms for the measured phase masses of this system were 0.0284 g and 0.0367 g, respectively.